FABRICATION OF FEPT FERROMAGNETIC NANOPARTICLES

by

KEVIN EUGENE ELKINS

Presented to the Faculty of the Graduate School of

The University of Texas at Arlington in Partial Fulfillment

of the Requirements

for the Degree of

DOCTOR OF PHILOSOPHY

THE UNIVERSITY OF TEXAS AT ARLINGTON

May 2008

ACKNOWLEDGEMENTS

I would like to express my deep appreciation and gratitude to my advisor Professor J. Ping Liu for his kind support, encouragement and mentoring. This research opportunity you graciously granted to me to study and explore magnetic nanoparticles brought to fruition many long years of study in materials science.

I would like to thank Professors Pranesh Aswath, Yaowu Hao, Choong-un Kim and Qiming Zhang for serving on my committee and providing critical feedback and direction on my written work.

I would like to thank Dr. Chuanbing Rong, Dr. Zhiqiang Jin, Dr. Baki Altuncevahir, Dr. Girija Chaubey, Vikas Nandwana, Narayan Poudyal, Tejaswi Vendantum, Vamsi Chakka and Daren Li for their important suggestions, assistance, encouragement on my studies and research and wonderful friendship during our time together.

I would like to thank our collaborators, Dr. Z.L. Wang at the Georgia Institute of Technology for his assistance in providing HRTEM analysis, and Dr. Hao Zeng at IBM for providing needed XRD and TEM analysis.

My hope one day is to take all I have learned and experienced from this endeavor to lift my children to see beyond what I could comprehend and carry a new family tradition into the uncharted waters of new days that lay ahead.

March 5, 2008

ABSTRACT

FABRICATION OF FEPT FERROMAGNETIC

NANOPARTICLES

KEVIN EUGENE ELKINS, Ph.D.

The University of Texas at Arlington, 2008

Supervising Professor: J. Ping Liu

Fabrication of chemically disordered FePt particles ranging from 2 - 9 nm with a precision of 1 nm has been achieved through modification of key process variables including surfactant concentration, heating rates and the type of iron precursor. In addition, the shape evolution of the FePt nanoparticles during particle growth can be manipulated to give cubic or rod geometries through changes to the surfactant injection sequence and solvent system. The primary method for synthesis of the disordered FePt

nanoparticles is the polyol reduction reported by Fievet et al., which has been modified and used extensively for synthesis of diff ering nanoparticle systems. Our procedures use platinum acetylacetonate, iron pentacarbonyl or ferric acetylacetonate as precursors for the FePt alloy, oleic acid and oleyl amine for the surfactants, 1,2-hexadecanediol to assist with the reduction of the precursors and either dioctyl ether or phenyl ether for the solvent system. For iron pentacarbonyl based reactions, adjustment of heating rates to reflux temperatures from 1 - 15 ^{o}C per minute allows control of FePt particle diameters from 3 - 8 nm. Substitution of iron pentacarbonyl with ferric acetylacetonate as the iron source results in 2 nm particles. A high platinum to surfactant ratio of 10 to 1 will yield 9 nm FePt particles when iron pentacarbonyl is used as the precursor. For use of these particles in advanced applications, the synthesized particles must be transformed to the $L1_o$ phase through annealing at temperatures above 500^{o}C. Inhibition of particle sintering can be avoided through dispersion in a NaCl matrix at a weight ratio of 400 to 1 salt to fcc FePt particles. Production of $L1_o$ FePt nanoparticles with high magnetic anisotropy with this process has been successful, allowing the original size and size distribution of the particles.

TABLE OF CONTENTS

LIST OF ILLUSTRATIONS

LIST OF TABLES

CHAPTER 1

MAGNETISM AND MAGNETIC MATERIALS

1.1 Introduction

Magnetic phenomena was readily visible to ancient people for those fortunate to live in latitudes offering a glimpse of the luminous lights of the Aurora Borealis. One can only imagine the wonder or perhaps fear that enveloped the observer while leaving questions unanswered as to the origins of the phenomena. Similarly, but to a more tangible extent, the discovery of loadstone, surely fired the imagination of those privileged to witness the unusual characteristics associated with this material.

Loadstone or magnetite as it is better known, is named in Greek from the Asia minor region of Magnesia from which it was obtained [2]. The ability to attract to iron or other pieces of magnetite was a unique attribute that eventually found utility in what appears to be the earliest of a compass in China [3]. As the investigation of magnetic materials and phenomenon were brought into the scientific process of discovery, early insight into the mechanisms responsible for magnetism was revealed allowing continued advancement of understanding and development of new technologies.

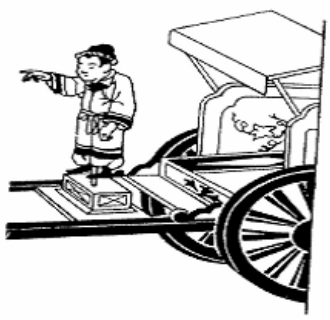

Figure 1.1 Schematic of a South Pointer used in Ancient China.

1.2 Quantities and Units in Magnetism

When discussing magnetic quantities, either CGS or SI units can be used; however, to highlight the origins of the quantities, SI units will be used here. A table with conversion factors will be provided to show the conversion in the units. From a macroscopic perspective, three magnetic vectors need to be defined:

B: Magnetic induction or magnetic flux density (T)

H: Magnetic field (A/m)

M: Magnetization (A/m)

The magnetic field (H) generated by a current (i) carrying loop of radius (r) is defined as follows:

$$H = \frac{i}{2\pi r} \tag{1.1}$$

The magnetization (M) or intensity of magnetization within a material is defined as the total magnetic moment per unit volume:

$$M = \frac{\sum m}{Volume} \tag{1.2}$$

When a material is placed in the external magnetic field, the magnetic induction (B) is a sum of the internal contribution to the magnetic field (magnetization) and external magnetic field (H) [4]:

$$B = \mu_o(H + M) \tag{1.3}$$

μ_o represents the permittivity of free space, which is given as 4π x 10^{-7} Henry/Meter. If using CGS units, μ_o is set to unity and the magnetic induction is expressed as:

$$B = H + 4\pi M \tag{1.4}$$

The measure of the induced magnetic dipole within a material in response to an external magnetic field is characterized by a quantity known as susceptibility. This quantity can be defined as a volume or mass property by the following equations:

$$\chi = \frac{M}{H} \qquad \text{Volume susceptibility (dimensionless)} \tag{1.5}$$

$$\chi_g = \frac{\chi}{\rho} \qquad \text{Mass susceptibility } (m^3/kg) \tag{1.6}$$

If equation (1.6) is divided by the external magnetic field, the equation can be rearranged to the following expression:

$$\frac{B}{H} = \frac{\mu_o(H + M)}{H} \tag{1.7}$$

$$\frac{B}{H} = \mu_o(1 + \frac{M}{H}) \tag{1.8}$$

$$\mu = \mu_o(1 + \chi) \text{ where } \mu \text{ is defined as B/H} \tag{1.9}$$

$$\mu_r = \frac{\mu}{\mu_o} \tag{1.10}$$

$$\mu_r = 1 + \chi \tag{1.11}$$

Equation (1.11) can be inserted into equation (1.8), resulting in the following relation:

$$B = \mu_o \mu_r H \tag{1.12}$$

Appendix B lists the conversion factors for the magnetic terms listed above between CGS and SI units.

1.3 Classification of Magnetism in Materials

The response of a material to an external magnetic field can be summarized by figure 1.2. If a material expels an external magnetic field, the magnetic flux density is zero within the material. This material would be classified as diamagnetic. If the material has a slight attraction to the e xternal magnetic field, thereby slightly increasing the magnetic flux density in the material, it would be classified as a paramagnet. Materials that strongly attract an external magnetic field are classified as ferromagnets.

If the susceptibility of these materials is plotted as a function of the external field, a graph similar to figure 1.3 will develop. As the graph shows, the magnitude in the change of the susceptibility of a paramagnetic material is substantially less than that of a ferromagnetic material. A negative slope of low magnitude occurs for a diamagnetic material.

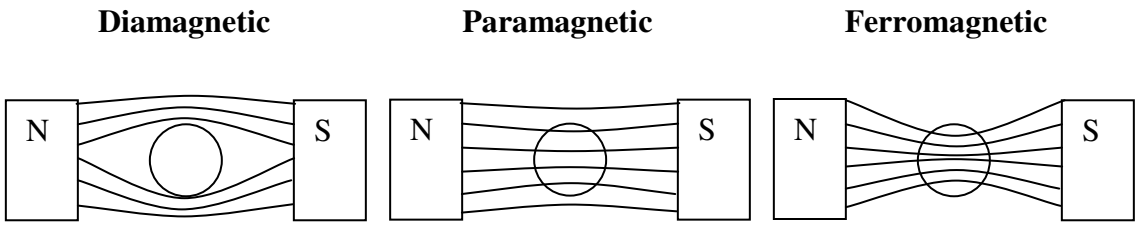

Figure 1.2 Materials with different magnetic response to a magnetic field.

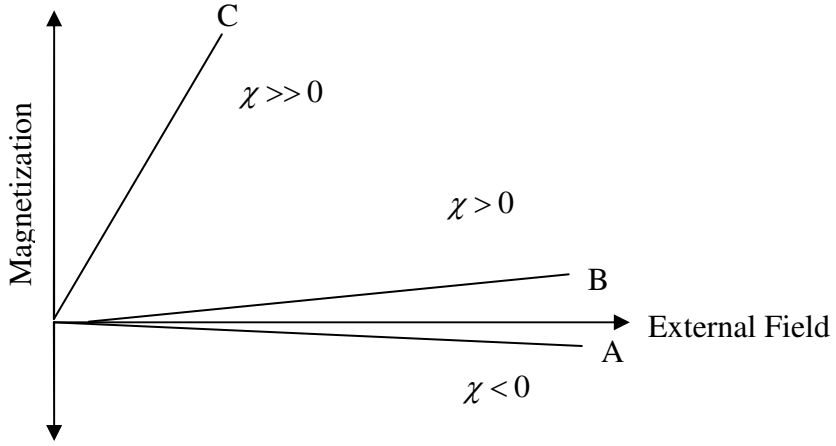

Figure 1.3 Magnetization response as a function of external field for A) diamagnet, B) paramagnet and C) ferromagnet.

1.3.1 Diamagnetism

All elements possess a degree of diamagnetism [4]. This phenomenon arises when non-interacting atomic moments align anti-parallel to an applied external magnetic field. The reason for this anti-parallel alignment is a consequence of Lenz law where a current in a circuit loop will generate a magnetic field that induces an opposite current in a separate circuit. For this reason, a diamagnetic material does not possess a magnetic

moment unless placed into an external field. If the susceptibility is plotted as a function of temperature, the susceptibility will remain constant.

1.3.2 Paramagnetism

Paramagnetic materials possess atomic moments that align parallel with an applied magnetic field; however, since the moments do not interact, when the external field is removed, the material will not retain a magnetic moment. Although a diamagnetic response is also induced in these materials, the magnitude of the paramagnetic moment is large enough to result in a positive susceptibility. If the inverse of susceptibility is plotted as function of temperature, it will result in a linear graph with the intercept occurring at zero Kelvin. This inverse response is known as Curie's law, which takes the form:

$$\chi = \frac{M}{H} = \frac{C}{T} \tag{1.13}$$

Where C is a constant. Many salts of transition metals and elements such as aluminum are paramagnetic. In addition, ferromagnetic and antiferromagnetic materials can show paramagnetic behavior after exceeding temperatures sufficient to disrupt the magnetic ordering.

1.3.3 Ferromagnetism

A unique property of ferromagnetic materials lies in that once an external field is applied then removed, a magnetic moment can be retained within the material. The parallel alignment of atomic moments occurs at very low external fields, and is a consequence of exchange interactions among the adjacent atomic moments. In 1907,

Weiss [4] described the phenomena of ferromagnetism by his molecular field theory. According to this theory, interacting atomic moments give rise to an internal magnetic field that is proportional to the magnetization.

$$H_E = \alpha M \tag{1.14}$$

The total magnetic field comprising the external field is:

$$H_{tot} = H + H_E = H + \alpha M \tag{1.15}$$

Substituting equation (1.15) in equation (1.13):

$$M = \frac{C}{T}(H + \alpha M) \tag{1.16}$$

Solving equation (1.16) for M and using the definition of susceptibility, $\chi = \frac{M}{H}$:

$$\chi = \frac{C}{(T - \alpha C)} = \frac{C}{(T - T_c)} \tag{1.17}$$

Equation (1.17) is called the Curie-Weiss law where $T_c = \alpha C$ is the Curie temperature. When $T = T_c$, the susceptibility diverges, which means a non-zero M exists even if the applied magnetic field is zero. This non-zero magnetization is referred to as spontaneous magnetization. When $T > T_c$, thermal energy is sufficient to disrupt the magnetic moment alignment leading to zero magnetization. If the inverse of the susceptibility is plotted as a function of temperature, the ferromagnetic material will behave analogous to that of a paramagnet above the Curie temperature.

1.3.4 Antiferromagnetism

If a material crystal lattice consist of two sub-lattices of atoms that have moments aligned anti-parallel to each other and the magnetic moments are of equal magnitude, a

net magnetization of zero will result. This material would be classified as an antiferromagnet. The susceptibility of this type of material is small and positive and at a temperature above a critical point referred to as the Neèl temperature (T_N), it follows the behavior of a paramagnetic material. Antiferromagnetism can be found in FeO, Fe_3Mn and $FePt_3$.

1.3.5 Ferrimagnetism

Similar to antiferromagnetism, the magnetic moments in a ferrimagnet are aligned antiparallel. However, the two sub-lattice magnetic moments are not equal in intensity, which results in a net moment in the absence of an external field. Compounds with the composition of $MO{\cdot}Fe_2O_3$ where M is a divalent cation such as Co^{2+}, Ni^{2+}, Fe^{2+}, Mg^{2+}, Mn^{2+}, etc. are an important class of magnetic materials that possess soft or hard magnetic characteristics and high resistivity. Magnetite $FeO(Fe_2O_3)$ is an example of a ferrimagnetic material.

1.4 Characteristics of Ferromagnetic Materials

Although the strong internal field within a ferromagnetic material will align the atomic moments, it is observed that the magnetization is absent unless an external field is applied. It was discovered that within the material, these atomic moments were aligned within volume elements, and the orientation of these volume elements cancelled out any expression of macroscopic magnetization.

1.4.1 Domain Structure

For ferromagnetic materials, there exists a balance between the alignment of atomic moments within volume elements (domains) and the energy required to form the

boundaries between the domains. The minimization of the system energy results in a material reaching a particular density of domains in the absence of any external influences. For example, mechanical processing of the material could impart energy needed to increase domains (domain wall energy), or if exposed to an external field, then domains aligned with the field can expand though domain wall motion.

1.4.2 Hysteresis

The word hysteresis is used in reference to any phenomenon where the effect lags the cause. If a ferromagnetic material is magnetized in one direction, the domains aligned with the external magnetic field will grow at the expense of other domains that are not aligned with the field through domain wall motion. As the external field is slowly reversed, the domains parallel to the reversed field then grow and maximize in size.

As the external magnetic field is increased, the material will reach a maximum in magnetization, which is referred to as saturation magnetization (M_s). When the external field is reversed and reduced to zero, the material will possess a certain value of magnetization known as remanent magnetization (M_r). In order to reduce the sample to zero magnetization, the reversed external magnetic field must reach a certain value known as intrinsic coercivity (H_{ci}) as seen in figure 1.4.

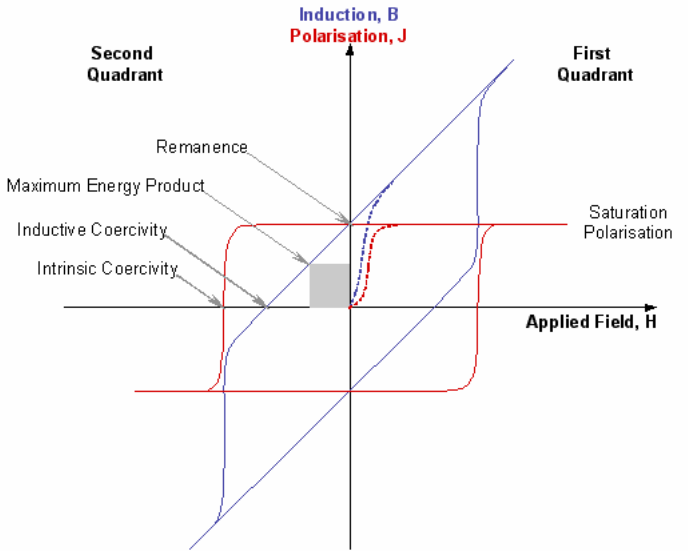

Figure 1.4 Hypothetical hysteresis showing key terms used in determining magnetic performance.

The size of the hysteresis loop is dependent on factors such as magnetocrystalline anisotropy, material impurities, defects and particle shape. The maximum product of the magnetic flux density and external field is referred to as the energy product $(BH)_{max}$, which is a measure of the maximum work the magnet can perform. For materials with sufficiently high H_c values ($H_c > 2\pi M_s$), the theoretical limit of the energy product is:

$$(BH)_{\max} \leq (2\pi M_s)^2 \tag{1.18}$$

1.4.3 Soft Magnets

If the ferromagnetic material is magnetized and demagnetized by very low external fields, the material is referred to as a soft magnet. Typical characteristics of a soft magnetic include low coercivity, high saturation magnetization and a low $(BH)_{max}$.

The magnetic domains within the material are easily rotated when the field is reversed through the process of domain wall motion. Materials such as iron, silicon iron, aluminum iron, etc., are common soft magnetic materials. They are widely used in the magnetic cores of transformers, motors, inductors and generators.

1.4.4 Hard Magnets

A "hard" ferromagnetic material requires a large external magnetic field typically greater than 1000 Oe to demagnetize the sample. As shown in figure 1.4, a considerable remnant magnetization exists in the absence of an external field, and because of this stored magnetization and large coercivity, these materials are commonly referred to as permanent magnets. The most well known hard magnetic materials are cobalt-rare earth alloys ($SmCo_5$ and Sm_2Co_{17}), neodymium-iron-boron ($Nd_2Fe_{14}B$), iron-platinum (FePt), cobalt-platinum (CoPt), hard ferrites ($SrO\text{-}Fe_2O_3$ or $BaO\text{-}6Fe_2O_3$) and Alnicos.

A measure of performance for hard magnets is the $(BH)_{max}$. Figure 1.5 shows the advancement of this measure up to the year 2000. Significant advances were marked by the development of rare earth compounds that supported high anisotropy. However, these compounds could not achieve the magnetization realized from traditional materials such as Co, Fe or $Fe_{65}Co_{35}$. It was realized that this pace of advancement in $(BH)_{max}$ could not continue singularly with hard phased magnets.

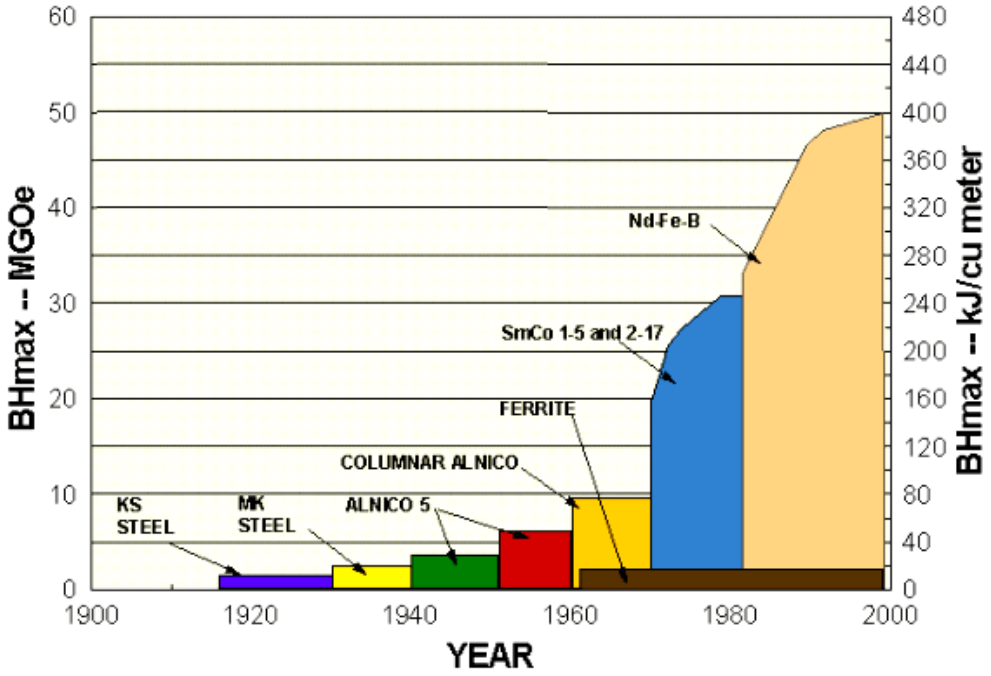

Figure 1.5 Magnetic material advancement up to year 2000 as a function of maximum energy product.

1.4.5 Soft/Hard Exchange-Coupled Magnets

An alternative approach to enhance the energy product was proposed in 1991 by Kneller and Hawig [5] through the careful control of the individual soft and hard materials in a composite magnet. Under the proper dimensional ratios, the nanocomposite would exchange-coupled the hard and soft magnetic phases. The hard phase provides the high magnetic anisotropy and stabilizes the exchange-coupled soft phase against demagnetization and the soft phase provides the high magnetization to enlarge the maximal energy product $(BH)_{max}$, as shown in Figure 1.6.

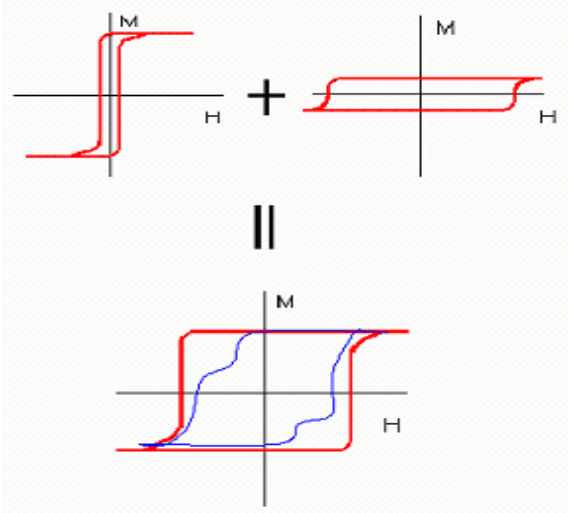

Figure 1.6 Hypothetic effects of exchange-coupling on the $(BH)_{max}$ between hard and soft magnetic materials.

The first-time observation of an exchange-coupled nanocomposite was made by Coehoorn and colleagues in a melt-spun $Nd_{4.5}Fe_{77}B_{18.5}$ sample that was annealed with the presence of the α-Fe phase [6]. Skomski and Coey performed a systemic theoretical study of exchange coupled films and predicted that energy product as high as 137 MGOe might be reached by the exchange coupling in oriented nanostructured magnetic materials [7].

1.5 Magnetic Anisotropy

The directional dependence of the magnetic properties within a crystal lattice gives rise to magnetic anisotropy. Properties such as magnetization and hysteresis are dependent on the type and magnitude of the anisotropy. For chemically produced FePt nanoparticles, processing occurs up to 300°C, which is sufficient to reduce or eliminate lattice strains; therefore, only magnetocrystalline and shape anisotropy will be mentioned.

1.5.1 Magnetocrystalline Anisotropy

If a single crystal of a magnetic material is measured along different crystallographic directions, it will be found that certain directions require a smaller external magnetic field to reach saturation magnetization than other directions. This identifies the easy axis (small field) and hard axis (large field) of magnetization see figure 1.7). The magnetocrystalline energy is then defined as the energy required to move the magnetization vector from the easy axis and align it parallel to the hard axis. For cubic systems, the equation for magnetocrystalline anisotropy is defined as [8]:

$$E = K_o + K_1(\alpha_1^2\alpha_2^2 + \alpha_2^2\alpha_3^2 + \alpha_3^2\alpha_1^2) + K_2(\alpha_1^2\alpha_2^2\alpha_3^2) + ... \quad (1.19)$$

Where $\alpha_1 = \cos(\theta)$, $\alpha_2 = \cos(\theta)\cos(\Phi)$ and $\alpha_3 = \sin(\theta)\cos(\Phi)$ [9]. When $K_2 = 0$, the easy direction is determined by the sign of K_1. If K_1 is positive, the energy associated with each direction is in the order:

$$E_{100} < E_{110} < E_{111}$$

For negative values of K_1 the energy associated with the crystallographic directions is:

$$E_{111} < E_{110} < E_{100}$$

For hexagonal crystals, the magnetocrystalline energy is dependent only on one angle, resulting in the following equation [8]:

$$E = K_o + K_1\sin^2\theta + K_2\sin^4\theta + ... \quad (1.20)$$

Magnetocrystalline anisotropy is intrinsic to the material, which is characterized based on a materials crystallographic orientation.

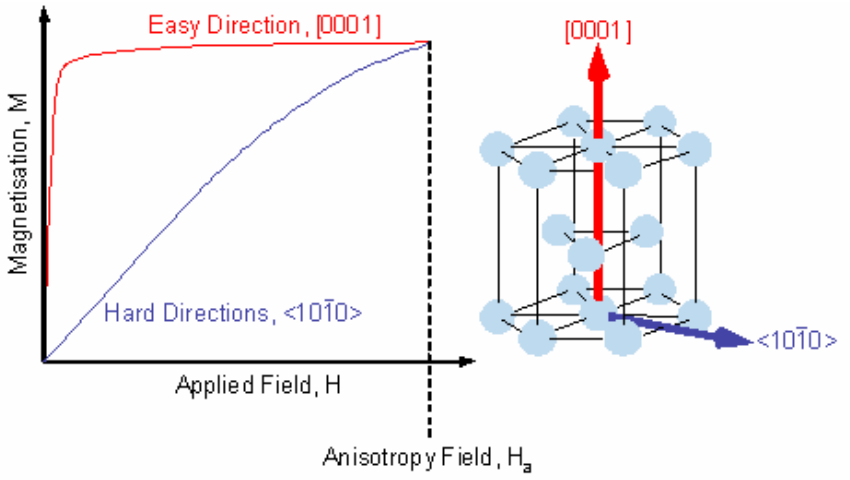

Figure 1.7 Directional dependence of saturation magnetization in Cobalt metal.

1.5.2 Shape Anisotropy

As deduced from the description, shape anisotropy arises in non-spherical materials where differences in surface poles and pole distance gives rise to a demagnetizing field. As seen in figure 1.8, the magnetization and external field point in opposite directions, giving rise to an internal magnetic field less than the external field. The demagnetizing field is proportional to the magnetization:

$$H_d = N_d M \tag{1.21}$$

Where N_d is the demagnetization factor. For an ellipsoid, the sum of the axial components of the demagnetizing factor equal [8]:

$$N_a + N_b + N_c = 4\pi \tag{1.22}$$

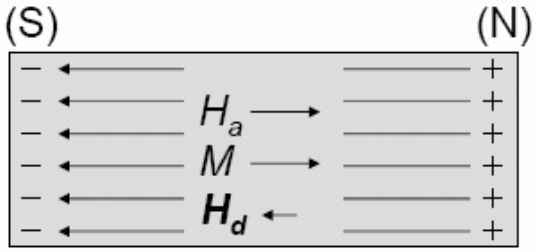

Figure 1.8 Illustration of the internal demagnetizing field within a ferromagnetic material. H_a is the applied field, M is the magnetization and H_d the demagnetizing field.

Formulas for demagnetization factors have been determined for prolate and oblate spheroids allowing the calculation of shape anisotropy constants in a form similar to that given for magnetocrystalline anisotropy. For example, the energy expression for a prolate spheroid is [8]:

$$E_{ms} = \frac{1}{2} N_d M^2 \tag{1.23}$$

Substitution of the demagnetizing components for the major and minor axis leads to:

$$E_{ms} = \frac{1}{2} M^2 N_c + \frac{1}{2}(N_a - N_c) M^2 \sin^2 \theta \tag{1.24}$$

The shape-anisotropy constant is defined as:

$$K_s = \frac{1}{2}(N_a - N_c) M^2 \tag{1.25}$$

Based on equation (1.25), depending on the material shape and magnetization, shape anisotropy can become a significant determinant on the material coercivity. For a prolate Co particle with a c/a axial ratio of 3.5, K_s is 45 x 10^5 ergs/cm^3 which equals the value of the K_1 magnetocrystalline anisotropy constant for cobalt [8].

1.6 Magnetism of Fine Particles

1.6.1 Size Dependent Magnetism

For ferromagnetic materials, as the particle size is decreased, critical length scales emerge which affects the coercivity, saturation magnetization and the shape of the hysteresis curve. The overall energy of a magnetic system is defined by the equation:

$$E = E_{ms} + E_{ex} + E_{an} + E_z \tag{1.30}$$

E_{ms} is the magnetostatic energy, E_{ex} is the exchange energy, E_{an} anisotropy energy and E_z is the Zeeman energy. The interaction between the exchange energy and magnetostatic energy leads to the exchange length [9]:

$$L_{ex} = \sqrt{\frac{A}{\mu_o M_S^2}} \qquad \text{where} \quad A = \frac{J \bullet S^2 \nu_{at}}{a} \tag{1.31}$$

μ_o is the permittivity of free space, M_s is the saturation magnetization, J is the exchange integral, S the spin vector, ν_{at} the atoms per unit cell and a, the lattice parameter. Below this critical length exchange interactions dominate. The balance between the exchange energy and magnetostatic energy defines the domain wall length [9].

$$\delta_D = \pi\left(\frac{A}{K_1}\right)^{\frac{1}{2}} \tag{1.32}$$

Where A is defined in 1.31, and K_1 is the magnetocrystalline anisotropy constant.

For bulk ferromagnetic materials, magnetic moments will divide into multiple domains that result in the material showing no net magnetization in the absence of an external field. These domains will reach a particular size that balances the anisotropy energy required to form the domain walls against the reduction in magnetostatic energy.

It is observed that the coercivity increases as the particle size is decreased as graphically shown in figure 1.9.

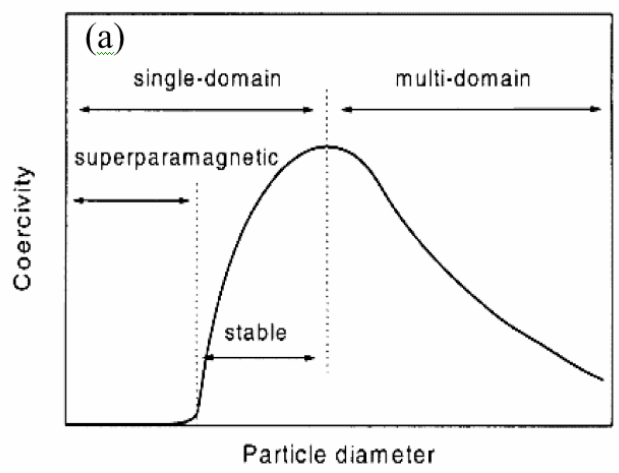

Figure 1.9 Coercivity as a function of particle diameter.

1.6.2 Single-Domain Particles

If the particle size has decreased to the equilibrium domain size, the particle transitions from a multi-domain to single domain state, which for a spherical particle is defined by the equation [9]:

$$D_c = 36\frac{(AK_1)^{1/2}}{(\mu_o M_s)^2} \tag{1.33}$$

μ_o is the permittivity of free space, M_s is the saturation magnetization, A is defined in 1.31, and K_1 is the magnetocrystalline anisotropy constant.

The magnetization vector lies in the same direction as the easy axis in the absence of an external magnetic field. Reversal of the magnetization vector requires it to pass through

the hard axis, which requires more energy than if magnetization is reversed through domain wall movement. However, as the particle size decreases, thermal agitation of the atoms tend to decrease alignment of the magnetic moments resulting in the particles reaching a maximum coercivity then rapidly dropping to zero as shown in figure 1.9.

1.6.3 Superparamagnetism

As magnetic particle sizes are decreased, a point is reached where the ambient thermal energy is sufficient to reverse the particle magnetization. Therefore, the system of particles will not exhibit any magnetization in the absence of an external magnetic field. The behavior of the ferromagnetic particles is similar to that of a paramagnetic material, which is referred to as superparamagnetism. When placed in an external field, the particles quickly saturates with no coercivity when the field is reversed.

CHAPTER 2

CHEMICAL SYNTHESIS OF METALLIC NANOPARTICLES

2.1 Introduction

A review of existing methods for producing metallic nanoparticles is beneficial for understanding the chemical tools available to the researcher in pursuing bottom up approaches for forming fine tuned magnetic composite structures. It should be noted that this review does not include purely oxide particle formation since applications that may use the magnetic nanoparticles can be significantly enhanced from the properties provided from magnetic metals and alloys. Moreover, challenges still remain with the formation of single element or alloy particles, surface protection from oxygen, composition control, size-control and dispersion stability.

2.2 Chemistry of Particle Formation

2.2.1 Particle Nucleation

Conventional nucleation and growth theory (CNT) provides a foundation thermodynamically for exploring conditions that lead to secondary phase formation, which in this case involves solid formation from a liquid state. The equation is constructed by stating the overall change in Gibbs free energy is a sum of the change in Gibbs free energy when a solute in solution is added to a crystal, ΔG_B, and the change in Gibbs free energy due to surface formation, ΔG_S:

$$\Delta G = \Delta G_B + \Delta G_s \tag{2.1}$$

The free energy change from new phase formation decreases and can be expressed by the difference in the chemical potential from the solute in solution and in the crystal phase while the free energy associated with generation of new surface area is the product of the specific surface energy and area [10]:

$$\Delta G = -N\Delta\mu + A\gamma_{SL} \tag{2.2}$$

Where $\Delta\mu = \mu_{solute} - \mu_{crystal}$ is the change in chemical potential in energy per mole, N is the moles of monomers transferred, A is the surface area generated and γ_{SL} the specific surface free energy. By inserting the geometric shape of the growing volume and surface area into equation (2.2), the typical form of the CNT equation is derived. For example, the number of moles transferred to a growing particle, N can be expressed as the total particle volume divided by the monomer molar volume Ω:

$$N = \frac{V}{\Omega} \tag{2.3}$$

Assuming a spherical particle, equation (2.2) becomes[10]:

$$\Delta G = -\frac{4}{3}\pi r^3 \frac{\Delta\mu}{\Omega} + 4\pi r^2 \gamma_{SL} \tag{2.4}$$

Under equilibrium conditions ($\frac{d\Delta G}{dr} = 0$), the equation can be solved to show the critical radius in which the formed particles are stable:

$$r_c = \frac{2\Omega\gamma_{SL}}{\Delta\mu} \tag{2.5}$$

Particle sizes below this critical radius are unstable and dissolve. Above the critical radius, the particles are thermodynamically stable enabling continued growth.

Figure 2.1 then shows the energy balance between surface area and particle volume. At r_c, the free energy requirement reaches a maximum with additional increases in radius leading to a decrease in the free energy.

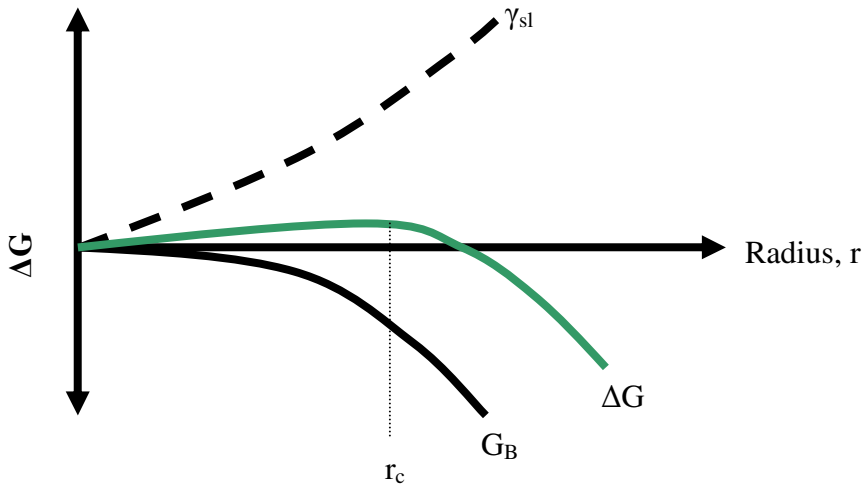

Figure 2.1 Gibbs free energy balance between surface area and particle volume leading to a critical radius for particle nucleation.

By defining the geometric expression for volume in equation (2.3) and surface area in equation (2.2), thermodynamic expressions for differing particle shapes can be derived.

2.2.2 Control of Critical Radius

The derivation of the critical radius shows the particle size is proportional to the interfacial energy and inversely proportional to the change in chemical potential, $\Delta\mu$. The chemical potential can be thought of in general terms as the difference in energy of the initial solution phase and the energy of the crystal phase plus the final solution phase. The magnitude of the change in chemical potential is the driving force for the

crystallization process. When considering the precipitation of a material from a liquid, the following chemical equation can be expressed:

$$aA + bB \rightarrow AB_{bulk} \tag{2.6}$$

The solvation of the bulk material is an equilibrium process between atoms leaving the bulk into the solution phase and solvated atoms leaving the solution and entering the crystal phase. The constant, K_{sp}, can then be defined:

$$K_{sp} = \frac{[A]_e^a [B]_e^b}{[AB]} \tag{2.7}$$

The quantities in equation (2.7) are activities and are usually approximated by concentrations; moreover, for crystalline materials, the activity of [AB] equals 1 reducing equation (2.7) to:

$$K_{sp} = [A]_e^a [B]_e^b \tag{2.8}$$

K_{sp} represents the system under equilibrium conditions, and to determine the change in $\Delta\mu$, the difference in the final and initial states is calculated by:

$$\Delta\mu = RT \ln(A^a B^b) - RT \ln K_{sp} \tag{2.9}$$

Where R equals 8.31 J $K^{-1}mol^{-1}$. Equation (2.9) rearranges to:

$$\Delta\mu = RT \ln \frac{(A^a B^b)}{K_{sp}} \tag{2.10}$$

The quantity (A^aB^b) for the supersaturated monomers can be referred to as the activity product (AP). The supersaturation is then defined by the quantity [11]:

$$\sigma = \ln\left(\frac{AP}{K_{sp}}\right) \tag{2.11}$$

Inserting equation (2.10) into (2.9) results in the change in chemical potential as a function of supersaturation:

$$\Delta\mu = RT\sigma \tag{2.12}$$

From equation (2.5), those changes in conditions that increase Δμ such as temperature or supersaturation will, in effect, lower the critical radius needed to grow a particle allowing the production of particles through a range of sizes. It should be noted that an increase in σ can occur through a decrease of K_{sp}, which can be modified by solution chemistry including factors such as solution composition, ionic strength, pH and impurity levels[11]. In practical terms, careful control of synthetic conditions, which include ligand type, concentration or blends, solvent type or co-solvent use, precursor concentrations and temperature result in differing particle sizes. Generally, the diameter of ceramic type nanoparticles varies as the inverse of the surfactant concentration [12]; however, for metallic nanoparticles such as FePt, the increase in concentration of surfactants can increase particle sizes [12].

2.2.3 Particle Growth

The general principles to chemically synthesizing monodisperse nanoparticles are usually stated in terms of achieving separation of the nucleation and growth steps. Underlying this statement is the chemical pathway that requires a rapid supersaturation of monomers above a critical threshold needed to initiate nucleation. Subsequently, the formed nuclei then rapidly deplete the monomer concentration below the nucleation

threshold allowing only particle growth to occur. Assuming a supply of monomers at a rate less than the rate of incorporation into the particles and uniform particle growth, the assembly of particles can achieve a targeted size with a monodisperse distribution. The prevalent mechanisms for explaining the growth of monodisperse particles are burst nucleation and growth [13], and slow nucleation with fast autocatalytic growth [14].

In burst nucleation (figure 2.2), a rapid generation of atomic species quickly reaches supersaturation, which provides the driving force for rapid nucleus formation. Nucleation rates (J_N) can be derived by substituting equation (2.5) for the critical radius into equation (2.4). The resulting equation then provides the energy barrier for nucleation, which controls the kinetics of particle formation [11]:

$$\Delta G_N = \frac{16}{3}\pi\gamma_{SL}^3\left(\frac{\Omega}{RT\sigma}\right)^2 \quad \text{at the critical radius} \tag{2.13}$$

$$\Delta G_N \propto \frac{\gamma_{SL}^3}{\sigma^2} \tag{2.14}$$

The nucleation rate equation is [11] :

$$J_N = A\exp\left(\frac{-\Delta G_N}{RT}\right) \tag{2.15}$$

$$J_N = A\exp\left(\frac{-B\lambda_{SL}^3}{\sigma^2}\right) \tag{2.16}$$

The A is a pre-exponential constant and B is a constant that contains summarized terms from 2.13. In equation (2.16), the quotient inside the exponential leads to a nucleation

rate that is very sensitive to changes in chemical conditions, which can lead to burst nucleation under the proper conditions, which is graphically presented in figure 2.2.

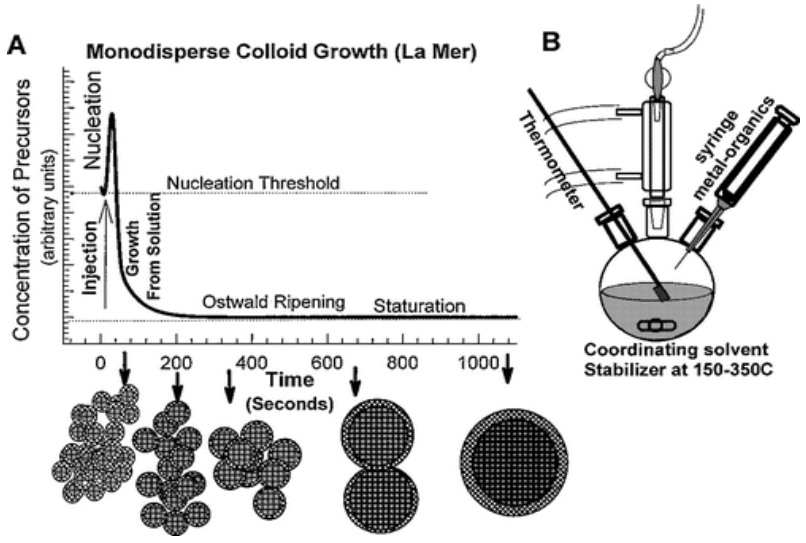

Figure 2.2 Graphic depicting the burst nucleation and growth mechanism.

Because of the large number of formed nuclei, the precursors that generate the monomers are quickly consumed resulting in a narrow distribution of particle sizes. Typically, rapid supersaturation of the metal monomer is achieved through decomposition of a precursor. Additional reductants drive the continued addition of metal to the formed particle. Temperature ranges for decomposition generally range from 100 – 200^{o}C, depending on the type of the precursor used.

For systems that generate a broad range of particle sizes under the proper conditions, the smaller particles can grow at a faster rate than the larger particles leading to uniform particle sizes if sufficient precursors are available. The variation in growth

rate as a function of particle size can be derived from equation (2.2), which is the Gibbs-Thomspon effect and is expressed in the following equation [15]:

$$C_e = C_\infty \exp\left(\frac{2\gamma_{SL}\Omega}{rRT}\right) \tag{2.17}$$

C_e is the solubility of the particle as a function of particle size, C_∞ is the solubility of the solid with infinite dimensions, Ω is the molar volume of the monomer and γ_{SL} the specific surface free energy. The chemical potential varies as a function of the particle radius, which indicates the driving force for particle growth is larger for smaller particles relative to larger particles within the same system.

2.2.4 Shape Control

A crucial aspect to engineering magnetic nanoparticles for various applications is the control of the particle shape. The equilibrium shape of the particle is one that minimizes the total surface free energy, which is sum of the energy of each individual facet. High-energy facets will grow the fastest leaving the low energy facets to dominate the particle structure. However, it is a combination of growth under kinetic conditions [16] and the nature of the growth source that lead to the particle shape, which include the number of step edges at dislocation sources. Since chemical and structural factors that lead to low energy facets are present at the step edges, the facet tends to mimic the shape of the growth hillock [11].

Equation (2.4) would be modified based on the approximation that an isotropic 2-D disc with an edge surface energy γ^{edge} develops on the crystal surface (figure 2.3).

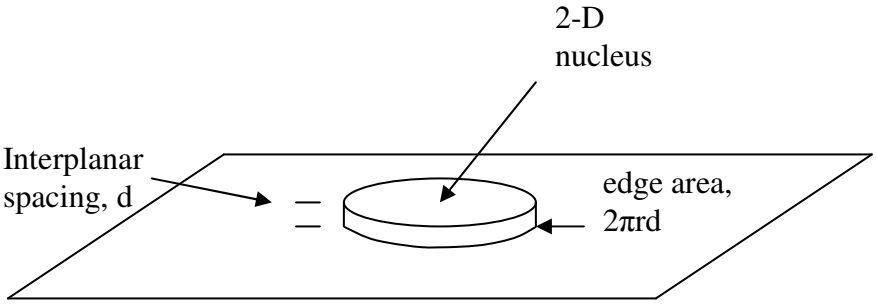

Figure 2.3 Circular nucleus on crystal face.

The thermodynamic equation then becomes:

$$\Delta G = -\pi r^2 d\frac{\Delta\mu}{\Omega} + 2\pi r d\gamma^{edge} \tag{2.18}$$

The resulting critical nucleus radius is:

$$r_c = \frac{\Omega\gamma^{edge}}{\Delta\mu} \tag{2.19}$$

Insertion of equation (2.19) into (2.18) gives the change in Gibbs free energy for the creation of one nucleus.

$$\Delta G_N = \pi(\gamma^{edge})^2\frac{\Omega}{\Delta\mu}d \tag{2.20}$$

The shape of the crystal can be modified through the introduction of components that interact with the step edges. These components can include organic molecules such as surfactants or inorganic ions. There are four mechanisms that can alter the growth hillocks, which are: 1) step pinning, 2) incorporation, 3) kink blocking, and 4) step edge adsorption [11].

In step pinning, impurities that adsorb on the step edges can inhibit the growth of the edge if the impurity spacing decreases below a critical distance. Above this distance, growth can occur unimpeded. The radius of curvature defined by the impurity spacing decreases the supersaturation of the edge atoms (Gibbs-Thompson effect), which in turn leads to the suppression of step edge growth.

Incorporation occurs when an impurity is added to the growing step edge. The distortion of the lattice with the impurity atoms raises the internal energy of the growth facet, which increases the solubility. Since supersaturation is inversely proportional to K_{sp}, the supersaturation is decreased which decreases the driving force for adding atoms to the growing step edge.

When impurity atoms temporarily adsorbs to kink sites, the kink site density is effectively reduced. Step advancement at these sites is inhibited resulting in a reduction in the growth of the facet. Since solubility is not affected, it is a reduction in the kinetic coefficient of step growth causing the reduced growth.

In step edge adsorption, the impurity lowers the step edge energy just as the surface energy of the facet is lowered when in contact with a surfactant. The angular dependence of the step edge energy is altered when considering a Wulff construction, which transitions to a new lower energy shape.

Through changes to the growth mechanism, particles shapes such as cubic, triangular, tetrapods, rods and wires have been synthesized in addition to the spherical geometry of many nanoparticle systems [16-21].

2.2.5 Particle Composition

Compositional changes over short dimensional ranges within a particle, to particle composition distributions have contributed to the inability of the nanoparticle assemblies from reaching the maximum possible magnetic properties. These compositional control difficulties occur as a result of differing reduction activation energy, reduction rates or heterogeneous material distribution from equipment limitations.

From a materials processing perspective, the variances in particle composition requires the use of thermal processing to distribute the elements comprising the system. However, annealing can lead to particle growth and sintering, which must be accounted for when planning the synthesis of the nanoparticles or use in applications.

2.3 Review on Chemical Methods for Nanoparticle Synthesis

2.3.1 Alkali Reduction

This reduction method involves the use of a strong alkali metal such as sodium, potassium or lithium to reduce the solvated precursor metal ion to the zero valence form. K. Tsai and J. Dye [22] reported how 2-15 nm metallic particles and their intermetallic compounds could be formed using an aprotic solvent and an appropriate cation complexing agent such as a crown ether or cryptand. Although this method indicated immediate reduction of the solvated metal salts, partial or complete oxidation of some metals such as Fe and Ni (surface oxidation) or Ti (complete oxidation) demonstrated the difficulties of synthesis, recovery and analysis for certain nanoparticle metals. D. Leslie-Pelecky and co-workers [23] using the Reike method synthesized Ni and Ni_3C composites with particle diameters in the range of 3 – 50 nm. Additional studies by D. Leslie-

Pelecky on Co [24] used a high temperature method with lithium metal in undecane, dodecane and pentadecane at temperatures of 200°C to reduce cobalt salts to metallic nanoparticles with an as-synthesized hexagonal close pack crystalline structure and particle sizes ranging from 5 – 50 nm based on Scherrer's analysis of the recovered samples.

Recent research by H. Nguyen used Collman's reagent to reduce the Fe and Pt ions simultaneously in equimolar ratios at temperatures between 297-389°C to generate nanoparticles of partial $L1_0$ tetragonal crystal structure without additional annealing [25].

2.3.2 Decomposition

A common method for generation of nanoparticles, which satisfy conditions needed for monodispersity of particle size and fine control over particle composition involves the use of chemical species that decompose under mild thermal conditions. Commonly, the carbonyl derivatives of many metals are used due to the instability of these species at elevated temperatures. Shouheng Sun applied this methodology to generate atomic iron at temperatures around 100°C from iron pentacarbonyl in the presence of platinum acetylacetonate and the diol 1,2-hexadecanediol. Once heated to temperatures around 280-300°C, chemically disordered face-centered cubic nanoparticles of FePt were formed [26, 27].

Many researchers have used this decomposition method to form nanoparticles of Co [16], Fe [28] FePt [28 29 30 31], FeCoPt [32]and CoPt[12]. The synthesis will generally involve the injection of a carbonyl complex ($Fe(CO)_5$ or Co_2CO_8), which will decompose at temperatures around 100°C, in the presence of the solvated Pt complex, diol and

surfactant. Although surfactants many vary, generally, a combination of oleic acid and oleyl amine are used or triphenyl phosphine oxide. This method many times is referred to also as the modified polyol process since Pt acetylacetonate is used in combination with 1,2-hexadecanediol; however, it is also know that $Pt(acac)_2$ will decompose within the temperature ranges used to form the binary alloys without the use of a mild reducing agent. Work performed by S.K. Suslick [33] formed Fe nanoparticles ultrasonic decomposition of $Fe(CO)_5$. Hexadecane solutions of $Fe(CO)_5$ containing oleic acid as a surfactant after sonication for 1 h at 30°C yielded nanoparticles with an average diameter of 8 nanometers.

In a recent method reported by Zafiropoulo [34] FePt and FePtAu nanoparticles were formed using $Fe(acac)_3$, $Pt(acac)_2$ and $AuCl_3$ salts in liquid paraffin in inert and reducing atmospheres at temperatures in the range of 390 – 400°C. XRD analysis on the particles confirmed the high anisotropic $L1_0$ tetragonal phase with coercivities of the FePtAu and FePt particles at 5.8 and 1.4 KOe respectively.

2.3.3 Hydrogen Reduction

At elevated temperatures generally above 500°C, hydrogen gas can be used to convert metal ions such as Co or Fe to the reduced state. In research performed by Y.C. Sui, $FeCl_3 \cdot 6H_20$ and $H_2PtCl_6 \cdot 6H_20$ solutions were loaded into alumina templates wetted by alcohol [35]. Subsequent annealing in hydrogen gas at 560°C for 1.5 hrs resulted in tetragonal $L1_0$ FePt nanotubes with lengths in order of 50 microns and diameter of 150 – 220 nm.

2.3.4 Hydride Reduction

The use of superhydrides such as lithium triethyl borohydride ($LiBEt_3H$) or sodium borohydride ($NaBH_3$) is a common technique in organic chemistry with several researchers successfully applying these reducing agents in both aqueous and non-aqueous systems to form nanoparticles such as Pt [36], Co [37], CoPt [38 - 40], FePt [41] and FePtRh [42].

The hydride reductive strength allows the simultaneous reduction of the metal ions in solution at sufficient quantities to form the nanoparticle alloys with monodisperse size distribution. The general method will use metal salts or complexes dissolved in an ethereal solvent such as phenyl ether/dioctyl ether and oleic acid/oleic amine surfactants. After addition of the hydride, at an elevated temperature (200^{o}C), the reactor will be heated to flux temperatures where further atomic diffusion can occur.

Research conducted H.M. Song [43] used a bimetallic precursor formed by reacting $[(CO)_4Fe(dppm)]$ (dppm = Ph 2PCH2PPh2) with $Pt(COD)Cl_2$ (COD = 1,5-cyclooctadiene) in toluene at room temperature, which when reduced with $LiBEt_3H$ formed fcc FePt nanoparticles with a typical size of 3.2 nanometers under what was described by the author as mild conditions.

2.3.5 Polyol Reduction

The method for homogeneous reduction of a metal salt in the presence of a mild reducing agent such as ethylene glycol or diethylene glycol under reflux conditions was report by F. Fievet, and coworkers in 1989 [44]. Successful production of micron-sized particles was achieved on Co, Ni and Cu complexes with a marked narrow size distribution rationalized by Fievet using the LaMer burst nucleation and growth

mechanism [13]. Subsequent studies by Fievet demonstrated the synthesis of CoNi and FeNi bimetallic particles of homogeneous composition and narrow size distribution using similar reaction conditions and materials, although Fe reduction occurred through disproportionation of the $Fe(OH)_2$ not reduction by the glycol. Furthermore, to ensure simultaneous reduction of the metal ions, NaOH was added to prevent the precipitation of the ion intermediates, which acts as a source needed for nucleation and growth [45, 46].

Many researchers have modified the method for the synthesis of particles of CoPt [30, 47-50], FePt [51-54], FePtAg [55] and NiPt [56] compositions. Most methods reflect the general modification of the solvent to an ethereal component such as dioctyl ether or benzyl ether with the replacement of the glycol with a diol of more hydrophobic characteristic such as 1,2-hexadecanediol. Moreover, these methods now use $Fe(CO)_5$ in combination with additional metal acetylacetonate complexes since the diol is unable to reduce the iron to a zero valence form. Temperatures generally range from 250 – 300^{o}C depending on the solvent boiling point which assists atomic diffusion and crystallization within the bimetallic particles. Inclusion of surfactants helps to suppress particle agglomeration, which contributes to the monodispersity of the particle size distribution.

2.3.6 Transmetallation

J. Park and J. Cheon reported a method by which a transmetallation reaction could be used to form monodisperse CoPt nanoparticles [57]. Transmetallation in a chemical reaction involves a redox process whereby the more active metal is oxidized when in contact with a less active metal ion. The cell potential will determine if the process is feasible through the relation $\Delta G = -nf\Delta E$, where a positive cell potential leads to a

negative change in the Gibbs free energy. With this method, CoPt alloys and Co core Pt shell nanoparticle structures where obtained with sizes of 1.8 and 6.27 nm respectively. Co seeds where generated via Co_2CO_8 decomposition in hot toluene containing the Pt complex. The formed Co then in turn reduced the Pt ions resulting in the formation of the CoPt nanoparticle alloy along with the oxidized Co complex. For core shell structures, the Co seeds where grown to sizes around 6 nm before being exposed to the Pt complex.

2.3.7 Oxide Coating on Metal Core

A common method to employ is to coat the monometallic core with its' oxide to form the M-MO core shell structure through controlled oxidation of the particles. An example of this application is demonstrated by C. Baker [58] where iron nanoparticles are formed through condensation of iron vapors then subsequent oxidation of the particles. Research conducted by L. Kuhn [59] formed αFe-FeO core shell structures with diameters of 15-21 nm and an oxide shell of approximately 3 nm using a hollow cathode sputtering system.

Methods that combine mono or bimetallic cores with differing oxide layers would include S. Kang [60] where fcc FePt nanoparticles were coated with MnO which prevents agglomeration and sintering of the particles during annealing to the high anisotropic phase due to the very high melting point of the MnO shell. A common technique to use is the coating of the metallic core with SiO_2. For example, M. Aslam [61] coated fcc FePt nanoparticles by reacting a solution of ethanol containing triethyloxysilane (TEOS) and

dispersed FePt nanoparticles with NH_4OH. Core shell particles with diameters of 10-12 nm and 5 nm FePt cores were obtained.

2.3.8 Metal Coating on Metal Core

N.Sobal [30] coated Pt nanoparticles with Co using a polyol process to form the Pt then decomposition of Co_2CO_8 to form the Co shell. An average diameter of 7.6 nm was obtained for this Pt-Co core shell structure. Park [57] used decomposition of Co_2CO_8 then transmetallation of the Pt ions to form Co core Pt shell nanoparticles with an average diameter of 6.27 nm.

CHAPTER 3

SAMPLE PREPARATION AND CHARACTERIZATION

3.1 Airless Solution Synthesis of fcc FePt Nanoparticles

3.1.1 Nanoparticle Synthesis

In section 4.2, a mixture of 0.5 mmol of $Pt(acac)_2$, 0.5 mmol to 2 mmol of $Fe(acac)_3$ and corresponding amount of 1,2-hexadecanediol was added to a 125 mL European flask containing a PTFE coated magnetic stir bar. 30 mL of dioctyl ether was then transferred into the flask and the contents stirred while purging with Ar for 20 minutes at room temperature. The flask was then heated to 100°C and held at 100°C for 20 minutes. During this hold, 0.5 mmol (0.17 mL) of oleyl amine and 0.5 mmol (0.16 mL) of oleic acid were injected into the flask while continuing the Ar purge. After the 20 minute hold, the mixture was maintained under an Ar blanket and heated to 295°C at a rate of approximately 7°C per minute. The flask was maintained at the refluxing temperature of 295°C for 30 minutes before cooling down to room temperature under the Ar blanket. Afterwards, all handling was performed open to the atmosphere.

In section 4.3, $Pt(acac)_2$ and $Fe(acac)_3$ in the molar ratio 1:1 were added to a 125 mL European flask containing a PTFE coated magnetic stir bar at room temperature. 1,2-hexadecanediol (5 times mole amount of $Pt(acac)_2$ and $Fe(acac)_3$) was added to the flask. 30 mL of dioctyl ether was then transferred into the flask and the contents were stirred while purging with Ar for 30 minutes at room temperature. The flask was then heated to

200° C at 6° C per minute by use of a Glas-Col hemispherical heating mantel connected to a programmable heat controller using a type J thermocouple. Once the temperature reached 200°C, the flask was kept at this temperature for 30 minutes. After the 30 minute hold, the flask was heated to 295° C at a rate of approximately 5°C per minute. The flask was maintained at a refluxing temperature of 295° C for 30 minutes before cooling down to room temperature under the Ar purge. Afterwards, all handling was performed open to the atmosphere.

In section 4.4, the synthetic experiments were carried out using standard airless technique in argon atmosphere. In a typical procedure, 0.5 mmol each of platinum acetylacetonate ($Pt(CH_3CHOCH_2OCHCH_3)_2$) and iron acetylacetonate ($Fe(CH_3CHOCH_2OCHCH_3)_3$) was added to 125 ml flask containing a magnetic stir bar and mixed with 20 ml of octyl ether in presence of 0.5 mmol each of oleic acid ($CH_3(CH_2)_7CH=CH(CH_2)_7COOH$) and oleyl amine ($CH_3(CH_2)_7CH=CH(CH_2)_7NH_2$). Argon gas was flowed throughout the whole experiment. After purging with argon for 30 minutes at room temperature, the flask was heated up to 200°C for 30 minutes and then up to 295°C for 30 minutes before cooling to room temperature under the argon blanket. The heating rate of 7°C per minute was maintained during the experiment.

In section 4.5, FePt nanoparticles were prepared via chemical reduction of $Pt(acac)_2$ and thermal decomposition of $Fe(CO)_5$ in the presence of oleic acid and oleyl amine. The synthetic experiments were carried out using standard airless technique in argon atmosphere. In a typical procedure, 0.5 mmol of platinum acetylacetonate was added to 125 mL flask containing a magnetic stir bar and mixed with 20 mL of

octyl/benzyl ether. After purging with argon for 30 min at room temperature, the flask was heated up to 120 °C for 10 min and a designated amount of oleic acid and oleyl amine was added. Iron pentacarbonyl or iron acetylacetonate were used as an iron precursor. Iron acetylacetonate (0.5 mmol) was added at room temperature while iron pentacarbonyl (1.0 mmol) was added at 120 °C when the platinum precursor dissolved completely. Then it was heated to reflux temperature and held at there for 1 h before cooling to room temperature under the argon blanket. The heating rate was varied from 1 to 15 °C per minute according to the experimental design.

3.1.2 Storage

For most samples, storage for up to 6 months or more was required for validation of original results or stability assessments of the particles. Upon completion of the synthesis, it was would found that refrigerating the particles in the dioctyl ether solvent provided good long-term stability. Therefore, after the fluids from the synthesis cooled to room temperature, the liquid was transferred to a 50 mL polyethylene conical bottom centrifuge tube, capped and then placed in a intrinsically safe refrigerator. Dispersions were then re-generated as needed for thin film deposition on silicon substrates or TEM grids.

3.1.3 Purification

The synthesized nanoparticles stored in the dioctyl ether were first precipitated from the dioctyl ether by addition of excess anhydrous ethyl alcohol in a typical volume ratio of 1 part reaction fluid to 4 parts anhydrous ethyl alcohol. This sample would be centrifuged for 15 minutes at 6000 rpm, after which the supernatant would be removed

from the centrifuge tube leaving the precipitated particles distributed inside. Generally 5 – 10 mL of hexane was added back to the centrifuge to re-disperse the particles. Occasionally, a minimal amount of oleic acid or oleyl amine would be added to the hexane along with sonication of the centrifuge tube to assist with re-dispersion of the particles. This process would be repeated up to three times to assess the initial particle size distribution.

3.1.4 Size Selection

For size selection, the first centrifugation would process as described previously; however, the second centrifugation would use hexane dispersion from the first centrifugation with a volume ratio of 1 part ethanol to 3 parts hexane dispersion centrifuged for 15 minutes at 6000 rpm. The larger particles would deposit on the centrifuge surface leaving the smaller particles dispersed. In this manner, nanoparticle size fractions could be removed enriching the hexane dispersion with the smaller sized nanoparticles. Additional steps similar to the second centrifugation could be applied to reach the desired particle size or distribution by increasing the ethanol fraction. All samples after centrifugation were dispersed in hexane, heptane, octane or a solvent combination in order to control the evaporation rate after drop casting of the dispersion on the substrate although once dispersed in hexane or heptane, the dispersions were best used within 24 hrs.

3.1.5 Deposition

For AGM analysis, nanoparticle samples were prepared for magnetic measurement by deposition of the dispersion on an approximate 3x3 mm silicon surface

at room temperature. The solvent type would control the rate of evaporation, which would allow the particles to self assemble on the substrate in a monolayer. The samples were then dried in a vacuum to remove volatile organics from the assemblies. Epoxy as the binder was used to prevent movement of the nanoparticles during magnetic measurements.

For SQUID analysis, fcc FePt particles were set in epoxy then mounted in the sample holder. In the case of fct FePt nanoparticles, samples were also prepared by mixing nanoparticles with epoxy or PVC as binder on Si substrates, or by freezing nanoparticles dispersions in alcohol or water with and without magnetic field alignment. Hardened epoxy or PVC and frozen solvents provide accurate magnetic measurements of nanoparticles by avoiding nanoparticle motion when the magnetic field is applied.

For TEM analysis, a 300-mesh copper grid with a carbon film deposited on a formvar backing, purchased from Ted Pella, was used. A drop of the nanoparticle dispersion solution in octane was put on the formvar side of the TEM grid and the solvents were allowed to evaporate in air. The surface energy of the formvar is apparently higher than the solvent, and hence the solvent can spread out easily on the grid instead of beading in the form of a small drop if deposited on the carbon film. Nanoparticles coated with surfactants can assemble into arrays on the grid under proper conditions.

For powder XRD analysis, dispersions of fcc FePt nanoparticles were deposited on approximately 1 cm^2 silicon or glass substrate at room temperature. Fct FePt

nanoparticles would temporarily disperse in ethanol allowing deposition on the 1 cm^2 silicon or glass substrates.

3.2 Preparation of fct FePt Thin Films and Monodisperse Nanoparticles

3.2.1 Annealing of fcc FePt Nanoparticles on Substrates

In order to transfer the disordered face-centered cubic (fcc) structure of the as-synthesized FePt nanoparticles to $L1_0$ structure with high magnetocrystaline anisotropy, the deposited thin film samples were placed in a ceramic annealing boat and annealed either in a nitrogen or forming gas (Ar + H_2 7%) atmosphere at temperatures between 550 and 900^o C in a Lindberg split top furnace. Samples, once inserted in the quartz tube, were purged in Ar for 1 hour then ramped to the desired annealing temperature over 30 minutes. Annealing times at the desired temperature ranged from 1 to 4 hours. Once the annealing time was completed, the furnace was opened and the quartz tube was air cooled while purging with Ar. To prevent sintering of the FePt nanoparticles during annealing, the salt matrix technique was used as described in the next section.

3.2.2 Salt-Matrix Annealing

Sodium chloride (NaCl) was chosen to be the separating media due to its chemical stability to the FePt nanoparticles, melting point of 801^{o}C and high solubility in water. The NaCl powder with particle size less than 10 μm was prepared by mechanical surfactant-assisted ball milling. A 500 ml Nalgene high-density polyethylene plastic container was inserted into a stainless steel container as shown in figure 3.1. And then the milling mixture as showed below was loaded into the plastic container.

- 50 grams of NaCl powder,
- 500 grams of 10 mm diameter 316 stainless steel balls, ball to powder weight ratio is 10:1,
- 200 ml of heptane,
- 20 ml of surfactant (oleyl amine), 10% of heptane.

The mixture was milled for 24 hours and the dispersion of NaCl in heptane was obtained.

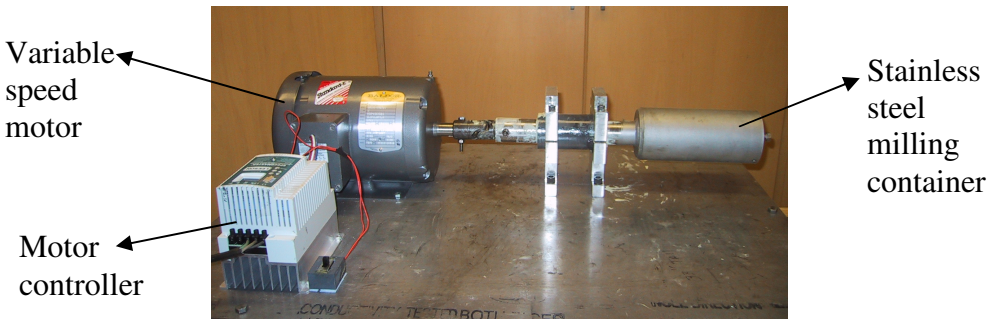

Figure 3.1 The ball milling set-up for milling of NaCl powder

As-synthesized FePt nanoparticles dispersed in hexane were mixed with the NaCl dispersion in heptane. The weight ratio of NaCl to FePt was varied, from 1:1 to 400:1. A Büchi R-200 rotary evaporator was used to achieve optimal mixing and evaporation of solvents. After all the solvents were evaporated, dry mixture of FePt in NaCl matrix was obtained. The dry mixture was crushed using a mortar and a pestle then transferred to a ceramic boat of sufficient size for annealing.

The salt-particle mixture was annealed in forming gas (93% H_2 + 7% Ar_2) at different conditions from 600 to 750 ^{o}C for 2 to 8 hours to investigate the fcc-to-fct

transition by using a Lindberg Blue-M tube furnace. After annealing, the mixture was then washed by de-ionized water for at least three times to remove NaCl. Centrifugation at 6000 rpm for 2 minutes was used to separate the FePt nanoparticles from the water. Acetone was used to absorb the remaining water and centrifugation was again applied to obtain separated FePt nanoparticles. Finally, these annealed FePt nanoparticles could be re-dispersed in cyclohexane with the assistance of surfactants.

3.3 Characterization of Nanoparticles

3.3.1 X-ray Diffraction (XRD)

Philips PW 1710 x-ray diffractometer with Cu-Kα radiation (wavelength λ=1.54056 Å) was used for crystalline structure characterization of samples. The samples were prepared by drop casting dispersions of nanoparticles in hexane or heptane on either a glass substrate or silicon wafer. The samples were dried under ambient conditions protected with a Petri dish cover to eliminate unintended contamination from air borne particles. Samples were then inserted in the sample holder and analyzed typically between 20 – 65 2θ degrees. The incident x-ray follows Bragg's law as described in figure 3.2 and the following formula:

$$n\lambda = 2d\sin\theta \tag{3.1}$$

When a monochromatic x-ray beam with wavelength λ is projected onto a crystalline material at an angle θ, diffraction occurs only when the distance traveled by the rays reflected from successive planes differs by a complete number n of wavelengths. By varying the angle θ, the Bragg's Law conditions are satisfied by different d-spacings

in materials. Plotting the angular positions and intensities of the resultant diffracted peaks of radiation produces a pattern that is characteristic of the sample. Usually 2θ is used instead of θ. If equation (3.1) is rearranged to the following form considering a first order reflection:

$$\theta = \sin^{-1}\left(\frac{\lambda}{2d}\right) \tag{3.2}$$

The distance between lattice planes can be calculated using the following formula:

$$d = \frac{a}{\sqrt{h^2 + k^2 + l^2}} \tag{3.3}$$

Since the lower order Miller indices result in larger interplanar spacing in equation (3.3), the diffraction angle in equation (3.2) will be lower. Therefore, as the Miller indices increase, the diffraction angles will also increase.

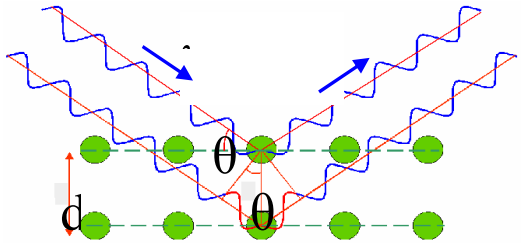

Figure 3.2 Bragg's law

3.3.2 *Transmission Electron Microscope (TEM)*

JEOL's 1200EX TEM was used for observing the morphologies and crystalline structure of nanoparticles. This TEM uses an acceleration voltage of 120 kV and can reach a magnification up to 500k times. Bright field images as well as the selected area electron diffraction (SAED) patterns were captured onto negative films, which were then

developed and scanned as digital images.

A 300-mesh copper grid with a carbon film deposited on a formvar backing, purchased from Ted Pella, were used for preparing TEM samples. A drop of the nanoparticle dispersion solution in octane was put on the formvar side of the TEM grid. The solvent was allowed to evaporate in air and assemble on the grid. However, for TEM imaging of nanoparticles, it is important to avoid excessive surfactant coating, which reduces the contrast and quality of the observation of nanoparticles.

The high acceleration voltage generates electrons that are collected by the condenser lenses. The electron beam then transmits through the specimen and the objective lens creates images of the specimen. Projective lens then projects the image on the fluorescent screen. By tuning the objective lens and projective lens, magnification and focus can be adjusted respectively. Images are recorded on the negative films by the camera installed at the bottom portion of the TEM. In the image mode of TEM, if the transmitted beam of electrons through the specimen is chosen to create images, then it is called bright field image. On the other hand, it is called dark field image if the diffracted beam is chosen. The selected area electron diffraction (SAED) pattern will be showed if the diffraction mode of TEM is set.

High-resolution TEM imaging of selected samples were performed by Hitachi HF 2000 TEM at Georgia Institute of Technology. Sample preparation for HRTEM analysis is the same as that for TEM.

3.3.3 Inductively Coupled Plasma-optical Emission Spectroscopy (ICP-OES)

Inductively coupled plasma-optical emission spectroscopy (ICP-OES) analysis on

composition of selected powder samples were processed by Galbraith Research Labs. This technique uses a plasma of argon that contains a large amount of cations and electrons. Temperatures within the plasma can reach up to 10,000 K, allowing the sample to fully ionize whether injected into the plasma either as an aerosol, thermally generated vapor or fine powder. Recombination with electrons within the plasma generates characteristic x-rays associated with the ions present. A spectrophotometer can then detect the wavelength and intensity of the emission allowing determination of multiple elements and relative quantites within the sample.

3.3.4 Alternating Gradient Magnetometer (AGM)

In an AGM measurement, the sample is mounted on an extended rod attached to a piezoelectric element and then placed at the center of the poles that generates magnetic field. An alternating gradient magnetic field is generated which produces an alternating force on the sample. This force (F) is proportional to the magnitude of the alternating magnetic field (B) and the magnetic moment (m) of the sample. Thus,

$$E = -m \bullet B \tag{3.4}$$

$$F_x = -\frac{dE}{dx} = m\frac{dB}{dx} \tag{3.5}$$

This force is converted into a proportional voltage by a piezoelectric element and hence the moment of the sample can be measured. The applied field is measured by a Hall probe sensor and the sensitivity of the AGM can reach up to 10 nemu. Samples with dimension up to 5 mm x 5 mm can be measured in AGM. The maximum magnetic field

that can be applied by AGM is limited to 14 kOe and it can only be operated at room temperature. Therefore, samples that have high anisotropy or require low or high temperature measurements will need magnetometers that can provide much higher saturation field to get accurate magnetic measurements and capability of operating in different temperatures.

Figure 3.3 Princeton Measurements Corporation Alternating Gradient Magnetometer.

3.3.5 High-field Magnetometers

3.3.5.1 Superconducting Quantum Interference Device (SQUID) Magnetometer

SQUID uses a superconducting magnet, through which large amount of current can flow so that large magnetic field can be generated. The magnetic measuring mechanism of SQUID belongs to an inductive technique. During magnetic moment measurement, the sample moves through a system of superconducting detecting coils and

the magnetic moment of the sample causes change in magnetic flux associated with the detecting coils, resulting in electric current produced in the detecting coils. The detecting coils are connected to the SQUID sensor, which functions as a highly linear current-to-voltage converter, producing very accurate variations in the output voltage that is proportional to the moment of the sample. The SQUID can generate a magnetic field as high as 70 kOe and can be operated in temperatures from 2 K to 400 K. The sensitivity of SQUID is 10 nemu up to applied field of 2.5 kOe and 0.6 μemu above that. Liquid helium is required to operate SQUID, which makes the use of it expensive. Sample dimension requirements of SQUID are almost the same as AGM, but the sample for SQUID can be longer in one of its dimensions. AGM is much easier, faster, and less expensive to operate comparing to SQUID. Hence, room-temperature measurements of all samples that can be saturated below 14 kOe should be measured by AGM.

Figure 3.4 Quantum Design SQUID Magnetometer.

3.3.5.2 Vibrating Sample Magnetometer (VSM)

VSM is an integrated magnetometer in Physical Property Measurement System (PPMS). It can generate a magnetic field as high as 140 kOe and provides magnetic moment sensitivity up to 1 μemu. The magnetic measuring mechanism is a VSM, which belongs to an inductive technique similar to the SQUID except that the motion of sample in the detecting coils for the VSM is much faster than in the SQUID. The normal operating temperature of VSM is from 1.9 K to 400 K, however, a VSM with an oven option can be operated from room temperature to 1000 K. The measurement of VSM is faster than SQUID but with lower sensitivity. Measurements that require saturation field higher than 70 kOe and temperatures higher than 400 K are performed by VSM instead of SQUID.

Figure 3.5 Quantum Design PPMS with VSM insert.

CHAPTER 4

NEW METHODS OF fcc FePt SYNTHESIS

4.1 Introduction

Research on the production of nano-scaled magnetic materials has been fueled by the required dimensional reduction on bit size for high-density storage media [26], nano-composite structures that can enhance the energy product of a magnet through exchange coupling of hard-soft phases[62] and potential medical applications that require enhanced image contrast from magnetic resonance applications[63-65] or specialty biological detection[66, 67], filtering and cellular targeting[56, 68]. A selection of candidate magnetic materials with the concomitant anisotropy required to maintain their ferromagnetic properties in the nanometer range is shown in figure 4.1. Only FePt and CoPt is capable of providing ferromagnetic properties down to 2 nm, although equiatomic ratios must be maintained in the alloy, and the magnetically hard $L1_o$ phase must be present.

In our studies, modified synthesis recipes have been used to produce FePt nanoparticles with alternative morphological and magnetic properties. By using ferric acetylacetonate ($Fe(acac)_3$) to replace iron pentacarbonyl $Fe(CO)_5$, we obtained monodisperse FePt nanoparticles with particles size of 2 nm [1]. It was also found that the FePt nanoparticles could be synthesized without using any polyol reducing agent [69] in octyl ether. We also studied the effect of various synthesis parameters, especially the

surfactant addition, on the particle size and shape and have obtained FePt nanoparticles with particle size from 2 to 9 nm with 1 nm accuracy [70].

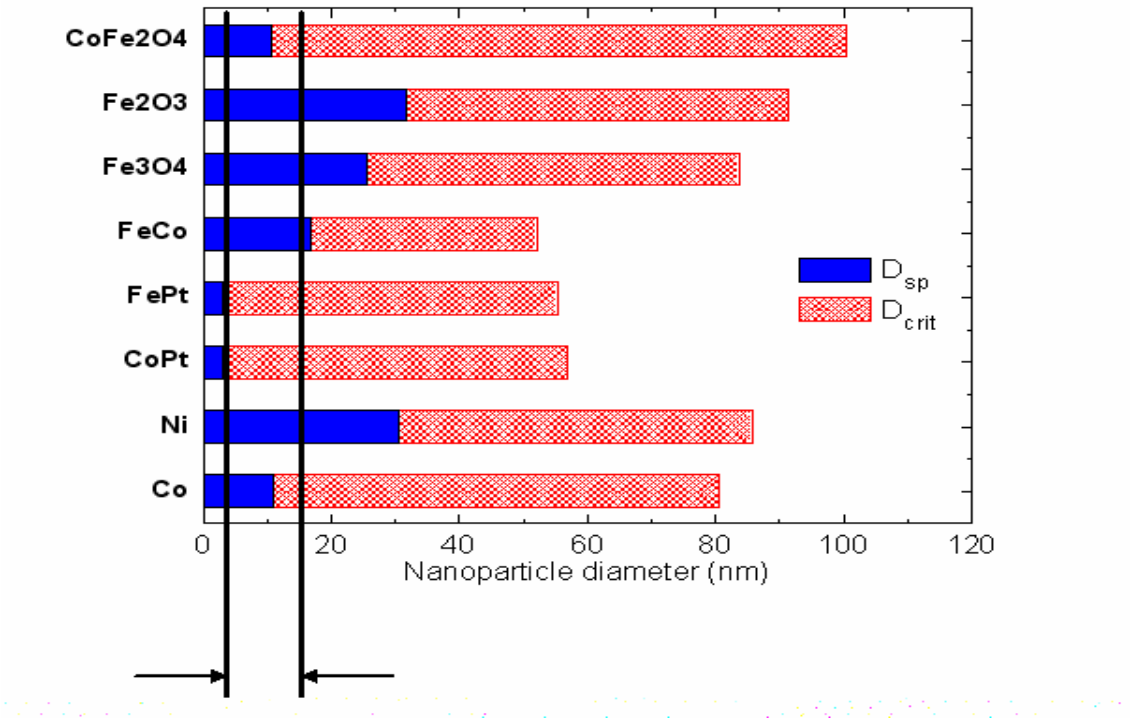

Figure 4.1 Bar graph showing the diameter in nanometers for select magnetic materials denoting the critical length scale required for single domain formation (D_{crit}) and superparamagnetic behaviour D_{sp}). Particle diameters in the 2 – 15 nm region are highlighted to show candidate materials for synthesis. Adapted from [71]

4.2 Synthesis of 2 nm FePt Particles

4.2.1 TEM and XRD Results

Figure 4.2 shows a typical TEM image of the as-synthesized FePt nanoparticles using the procedure described in chapter 3. The particle sizes are approximately 2 nm. Careful examination of the HRTEM images reveals that particles show good crystallinity,

with many being single crystals and with some particles possessing multiple twin boundaries. The HRTEM of a particle is shown in the inset in Fig. 4.2. The crystal structure of the particles is chemically disordered fcc, and the (100) lattice spacing is about 3.8 Å, which is consistent with the known fcc FePt structure [72] [73].

XRD patterns in Fig. 4.3 confirm the chemically disordered fcc crystal structure of the as-synthesized nanoparticles. This structure has a low anisotropy and hence needs to be annealed in order to obtain the fct phase, which possesses a high magnetocrystalline anisotropy responsible for the large coercivity [74]. Figure 4.3 also shows the XRD patterns for the sample annealed in nitrogen at 600°C for 30 minutes and the fct FePt sample produced by the method developed by Sun [27], which uses the $Fe(CO)_5$ and $Pt(acac)_2$ precursor. It can be clearly seen from this figure that both the peak position and intensity for the annealed sample prepared by this new method match the standard fct FePt phase.

4.2.2 Magnetic Properties

The in-plane hysteresis loops for the samples synthesized using a 2:1 precursor mole ratio ($Fe(acac)_3$:$Pt(acac)_2$) and annealed on a silicon substrate in nitrogen with a forming gas atmosphere are shown in Fig. 4.4. The coercivity of the sample annealed in forming gas is about 1.8 T, indicating a transformation from the fcc phase to the high magnetocrystalline fct FePt phase. The ICP analysis of these samples revealed their final particle composition to be $Fe_{44}Pt_{56}$. The coercivity of the samples annealed in nitrogen is less than the coercivity of the samples annealed in forming gas with all other variables being the same. This observation is in agreement with Ref. 75. Forming gas being a

reducing atmosphere reduces any iron in the oxidized state present in the nanoparticles thereby improving the chemical ordering in the fct crystal structure by bringing the atomic ratios of Fe and Pt closer to unity, which increases the chemically ordered fct phase in the sample leading to an increase in coercivity. Small differences between the in-plane and out-of-plane hysteresis loops for both samples annealed in N_2 and forming gas, indicate the FePt particle assemblies have a random orientation in the magnetic easy axis.

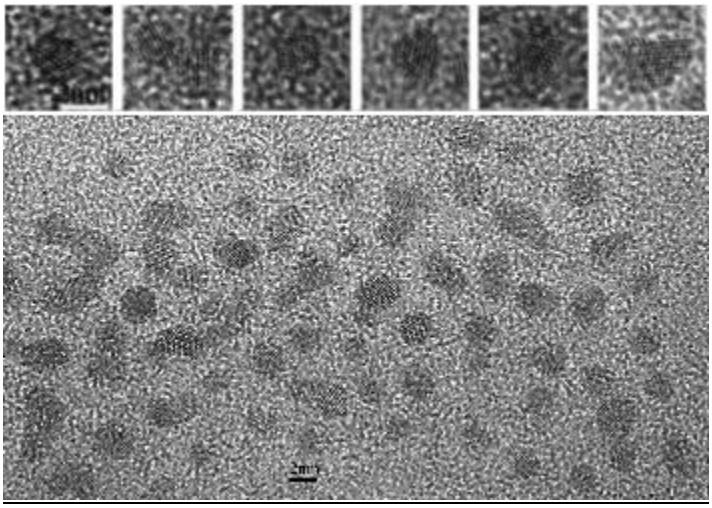

Figure 4.2 TEM image of the as-synthesized FePt particles. The HRTEM images of individual particles selected at random are shown at the top. The scale of these images is 2nm and it is shown in the first image on the top left corner.

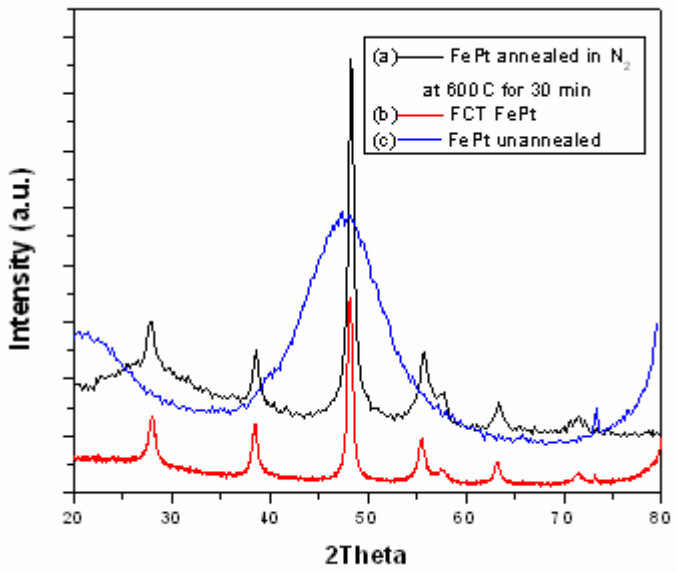

Figure 4.3 X-ray diffraction patterns of (a) the annealed FePt particle assemblies, and (b) the standard fct FePt structure, and (c) the as synthesized FePt nanoparticle assembly.

The final particle composition was changed by changing the initial mole ratio of the precursors. However, the initial mole ratio of the precursors was not carried over to the final product. Fig. 4.5 shows the coercivity dependence on the molar ratio of the FePt samples annealed in forming gas at 600^{o}C for 30 minutes. The coercivity of the annealed nanoparticles was found to increase rapidly to 1.8 T with increasing mole ratio of the precursors for ratios up to 2 and then decreased as the ratio is increased further to 4. The coercivity can be increased further if the synthesis and thermal processing are optimized.

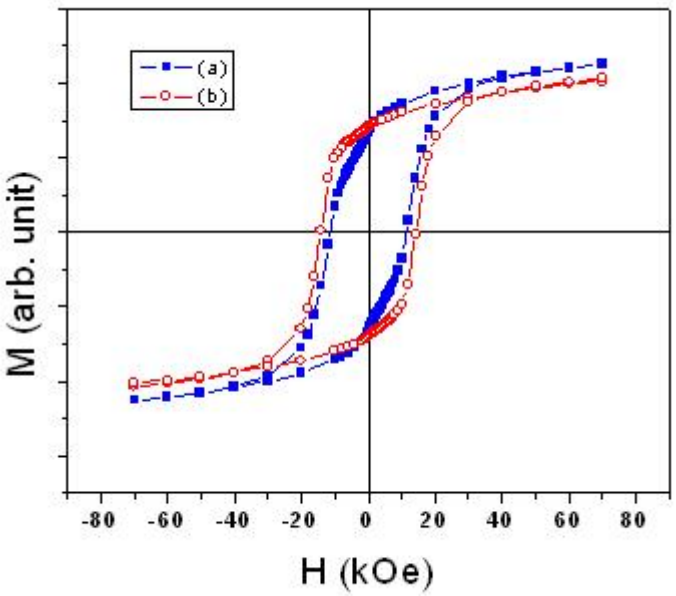

Figure 4.4 (a) Hysteresis loop of the sample annealed in N_2 at 600 C for 30 minutes, (b) Hysteresis loop of the sample annealed in FG at 600 C for 30 minutes, with a coercivity of about 1.8 T. Both samples are from the 2:1 precursor mole ratio synthesis.

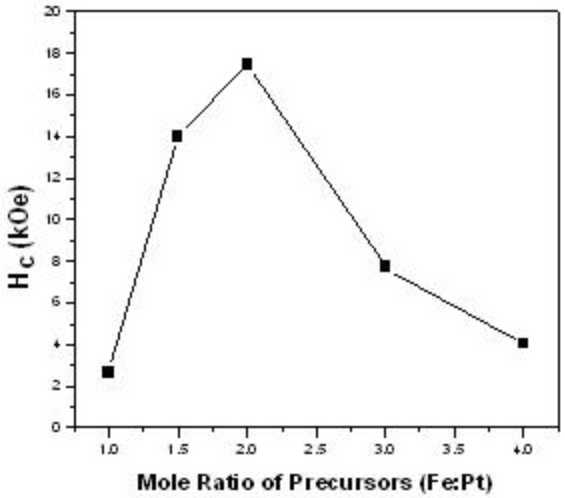

Figure 4.5 Coercivity as a function of initial mole ratio of the precursors ($Fe(acac)_3$:$Pt(acac)_2$) for the samples annealed in FG at 600^{o}C for 30 minutes. The maximum coercivity is about 1.8T for the 2:1 mole ratio sample.

4.3 One-pot Synthesis of FePt Nanoparticles with Controlled Composition by the Polyol Reduction of $Fe(acac)_3$ and $Pt(acac)_2$

4.3.1 Reduction using 1,2-hexadecanediol

Polyol reduction methodology used by Fievet et al. [44-46] and modified by Sun et al. [26] has been developed by many researchers to provide a wide variety of nanoparticle systems for investigations in the mentioned applications. The polyol process requires at its basis, a diol as reducing agent, metal salt precursors, surfactants and a solvent. The surfactants are added to prevent particles from agglomeration and inhibit oxidation. In certain cases, surfactants can also induce geometric changes to the particles [76]. In a typical polyol synthesis route, as shown in figure 4.6, FePt particles are synthesized via decomposition of iron pentacarbonyl, ($Fe(CO)_5$) and reduction of ($Pt(acac)_2$), in presence of 1,2-hexadecanediol (HDD). Oleic acid and oleyl amine are used as the surfactants in a proper solvent [27, 41, 43, 51-53, 77-81] . .

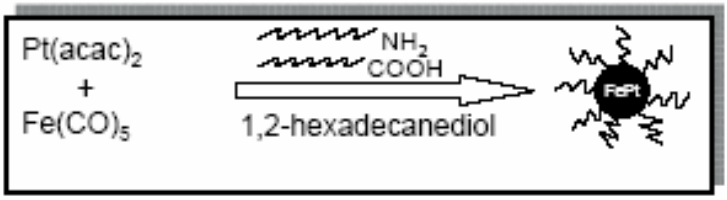

Figure 4.6 Typical polyol synthesis route for FePt nanoparticles.

The one-pot synthesis of FePt nanoparticles with controlled composition by the polyol reduction of $Fe(acac)_3$ and $Pt(acac)_2$ only in presence of 1,2-hexadecanediol in octyl ether, where the conventional surfactants such as oleic acid and oleylamine, are not

used, as shown in figure 4.7. It is interesting to find out that monodisperse FePt nanoparticles can be prepared by using this simple recipe and the resulting nanoparticles show improved magnetic properties.

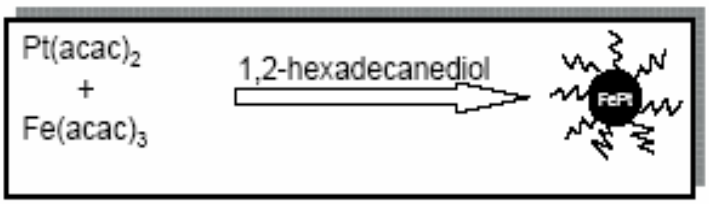

Figure 4.7 A simple synthesis route for FePt nanoparticles used in this investigation.

4.3.2 TEM and XRD Results

Fig. 4.8 shows a TEM image of the as-synthesized FePt nanoparticles. The average particle size is approximately 2 nm, which is typical for FePt nanoparticles reported earlier for recipes using $Fe(acac)_3$ [1]. Moreover, the particles derived from this method are fairly uniform in shape and size distribution.

Fig. 4.9 shows XRD patterns of as-synthesize FePt nanoparticles. From the position of the peaks, it is clear that the as-synthesized FePt nanoparticles have a chemically disordered fcc structure. An average particle diameter of 1.6 nm was calculated from the peak width of the XRD pattern using Scherer formula, which is consistent with the diameter calculated by analysis of the TEM images, and is similar to the particle size reported in Ref. 1. Energy dispersive x-ray analysis of the unannealed FePt particles show the initial feed ratio of Fe and Pt metal precursors are maintained in the fcc FePt nanoparticles.

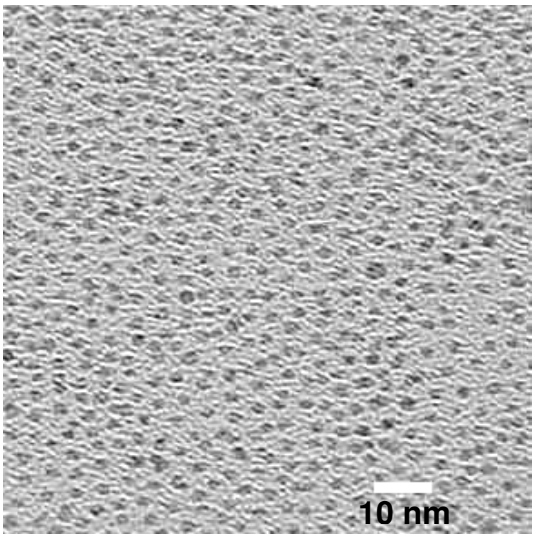

Figure 4.8. TEM image of the as-synthesized FePt particles using HDD as the surfactant and reductant.

The structural characterization shows that fcc FePt nanoparticles were synthesized by co-reduction of $Fe(acac)_3$ and $Pt(acac)_2$ in presence of 1,2-hecadecanediol in octyl ether. More interestingly, the HDD also played a role as an effective surfactant by protecting the formed nanoparticles from oxidation as seen in the annealed XRD pattern in figure 4.10 (a). Based on the structure and functionality, using HDD as a surfactant for dispersing the formed nanoparticles is not unreasonable, while also providing the mild reductive species needed to form the fcc FePt nanoparticles. In addition, it is possible that the oxidized HDD molecules can facilitate dispersion of particles in nonpolar solvents, similar to traditional methods where ligands such as oleic acid and oleylamine are used [27, 41, 43, 51-53, 77-81].

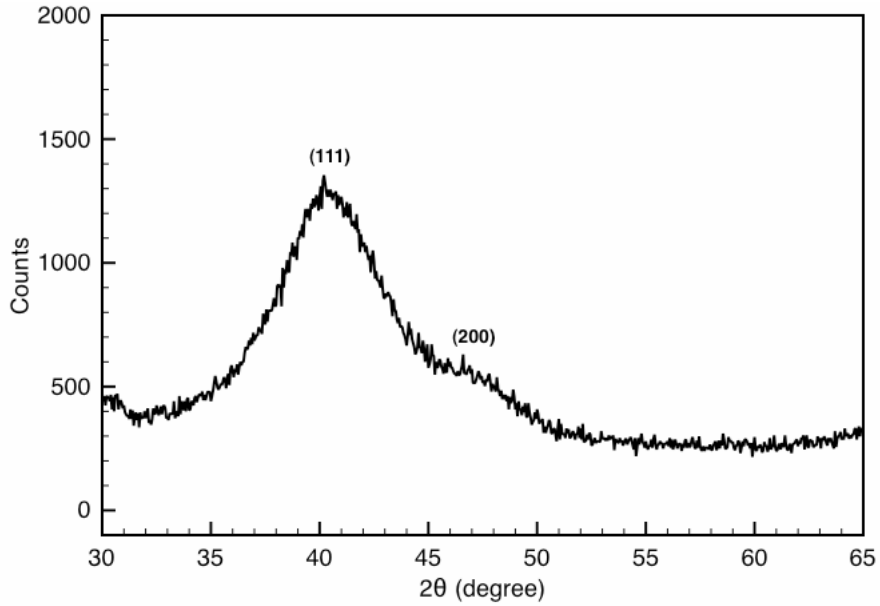

Figure 4.9 Powder XRD pattern of the as-synthesized FePt particles using HDD as the surfactant and reductant.

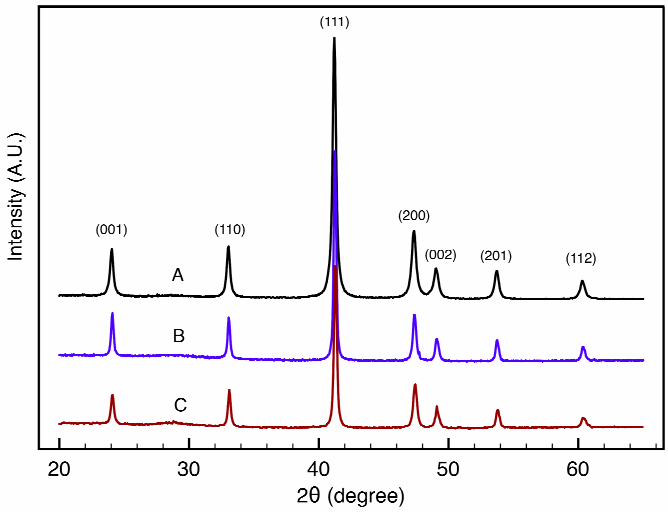

Figure 4.10 XRD scans of the samples annealed at 700° C in A) nitrogen, B) forming gas (Ar + H_2 7%), and C) particles from the reference [1] method annealed at 700° C in forming gas.

4.3.3 FePt Coercivity on Silicon Substrates

The as-synthesized FePt nanoparticles were annealed on silicon substrates at temperatures from 550 – 900°C to facilitate transformation to the chemically ordered $L1_0$ tetragonal FePt phase. Fig. 4.10 shows the XRD patterns for the samples annealed in nitrogen and Ar +H_2 (7%) at 700° C for 1 h, compared with the XRD pattern for the $L1_0$ FePt sample produced using $Fe(acac)_3$ and $Pt(acac)_2$ precursors using oleic acid, oleyl amine and HDD [1]. It can be seen from figure 4.10 that both the peak position and intensity for the annealed samples prepared by our new method match with those of the samples made from a standard method, indicating that Ll_0 structure is indeed formed after thermal annealing. This also confirms that the particle composition is in the right range for the formation of the equal atomic $L1_0$ phase. In addition, samples annealed in nitrogen do not show any oxide peaks in their XRD patterns, which indicates the HDD effectively protected the fcc FePt nanoparticles from oxidation when exposed to the open atmosphere.

Fig. 4.11 shows the coercivity change with annealing temperature of the annealed samples obtained from our new method, compared with the coercivity values of particles obtained by the method using oleic acid and oleyl amine as the surfactant. Samples were annealed on a Si substrate under Ar + H_2 (7%) for 1 h. It was observed that for the FePt sample produced using the method for 2 nm particles [1], a maximum coercivity of 1.8 T was obtained at 700°C and a sharp decrease in coercivity was observed above 700° C. On the other hand, for the sample prepared by our new method, coercivity continues to increase above 700°C, and a maximum coercivity of 2.3 T was obtained at 800° C. It is

interesting to find that there is an approximately 28% increase in coercivity of the particles obtained by our new method as compared to the particles prepared using the 2 nm method [1].

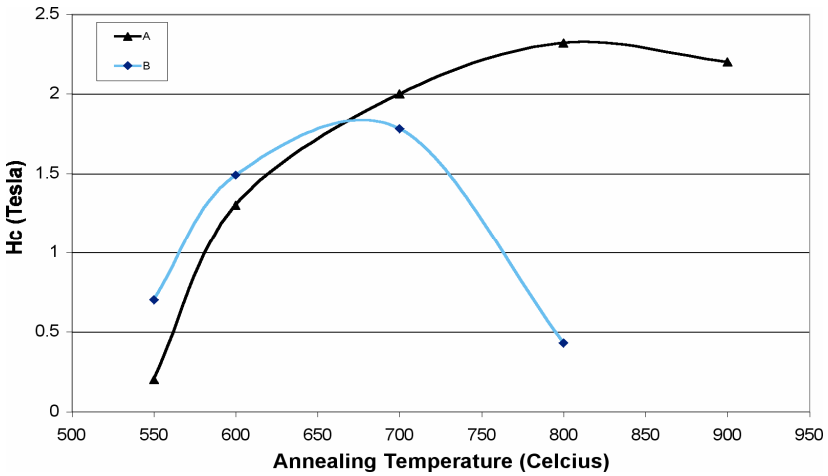

Figure 4.11 Annealing temperature dependence of coercivity of annealed samples prepared by the current method (curve A) and the method reported in Ref. [1] (curve B). The samples were annealed in forming gas for 1 h.

Even when particles are annealed at 900^{o} C, only a slight decrease in coercivity of the FePt nanoparticles is observed. The exact nature of the observed coercivity enhancement by this method is not completely clear, however, it is possible that the nanoparticles derived from this new method did not sinter substantially during annealing, relative to the particles from the 2 nm method [1]. This degree of isolation is possible if the HDD is preferentially adsorbed to the particle surface during synthesis, protecting the particles during annealing from sintering. A smaller particle size and high degree of chemical ordering within the particles could then result in higher coercivity at the higher

annealing temperatures. The higher coercivity may also be related to the enhanced atomic diffusion during the heat treatment, enhancing the $L1_0$ phase transformation.

We have also investigated the effect of HDD amount on the nanoparticle formation. During the FePt synthesis, the mole amount of HDD was varied from 5, 10 and 15 times of $Fe(acac)_3$ and $Pt(acac)_2$. It was observed that increased HDD mole amount during FePt synthesis does not lead to changes in the annealed FePt samples. There is essentially no change in coercivity of the samples with different HDD amount.

4.4 FePt Nanoparticle Synthesis via Hot Solution Processing

To make binary metallic nanoparticles by solution methods, care should be taken in choosing precursors, surfactants, solvents, reducing agents and reaction temperatures. In synthesis of FePt nanoparticles, both the metal precursors $Fe(acac)_3$ and $Pt(acac)_2$ were first dissolved in octyl ether and then the nucleation starts which is followed by the growth of the nuclei. The color transition of the solution was taken as the sign of decomposition of the precursors. To observe the decomposition temperature of $Fe(acac)_3$ and $Pt(acac)_2$ individually, they were each heated in separate flasks with octyl ether under an Argon blanket and found out that they decompose at approximately 180 and 140°C, respectively. The use of reducing agent (1, 2 hexadecanediol) assist in the reduction of the $Pt(acac)_2$ precursor. In this study, the intermediate reaction temperature was 200ºC, and the reducing agent was therefore not necessary.

The surfactants were injected at 200ºC based on the fact that both the precursors completely dissolve in octyl ether at this temperature. Oleic acid and oleyl amine are proven to be a good ligand combination for FePt formation and stabilization. Oleic acid

has long been used to stabilize varieties of colloids including Fe nanoparticles [40]. Long carbon chain amines, on the other hand, are good stabilizing ligands for noble metal such as Pt. The structural similarity between oleic acid and oleyl amine provides a smooth ligand shell around each FePt nanoparticle, facilitating superlattice formation [114].

Figure 4.12 shows XRD pattern of as synthesized and annealed FePt nanoparticles; the particles were annealed in forming gas at 650°C for 1 hour on a silicon substrate. The XRD of the as-synthesized 2 nm particles exhibit a disordered fcc crystal structure with low magnetic anisotropy. Because of the small particle size, the peaks are very broad and hence overlap on each other, which can be observed by comparing them with the XRD peaks of the as synthesized 4 nm FePt particles. The average particle diameter estimated from Scherrer's formula is consistent with that determined by TEM images (figure 4.13), indicating that each individual particle is a single crystal. The reason for such small size may be the sudden nucleation from precursor decomposition and precursor depletion.

Annealing enhances the diffusion of the Fe and Pt atoms to rearrange into the thermodynamically stable chemically ordered fct structure, as indicated by the (111) peak shifts and evolution of (001) and (110) peaks (figure 4.11). After annealing in forming gas at 650ºC for 1 hour, the particles sintered together resulting in granular thin films on which further characterization was performed. The sintered particles were found to be up to 30 nm in diameter as shown in the figure 4.13(b).

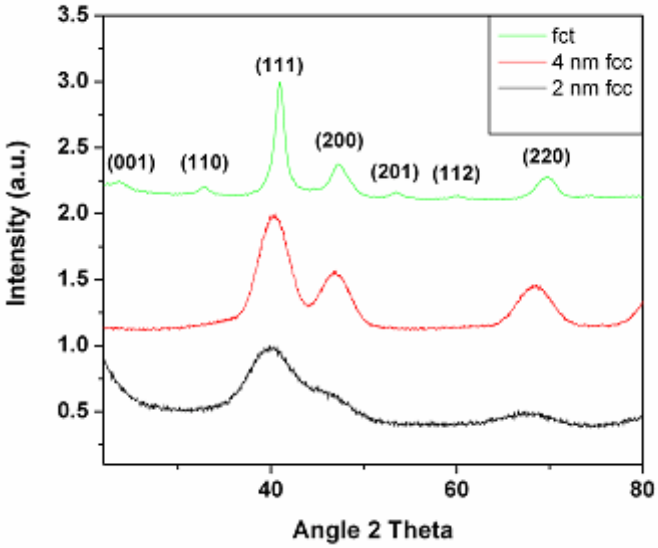

Figure 4.12 XRD pattern of 2 and 4 nm as-synthesized FePt nanoparticles and annealed FePt thin films

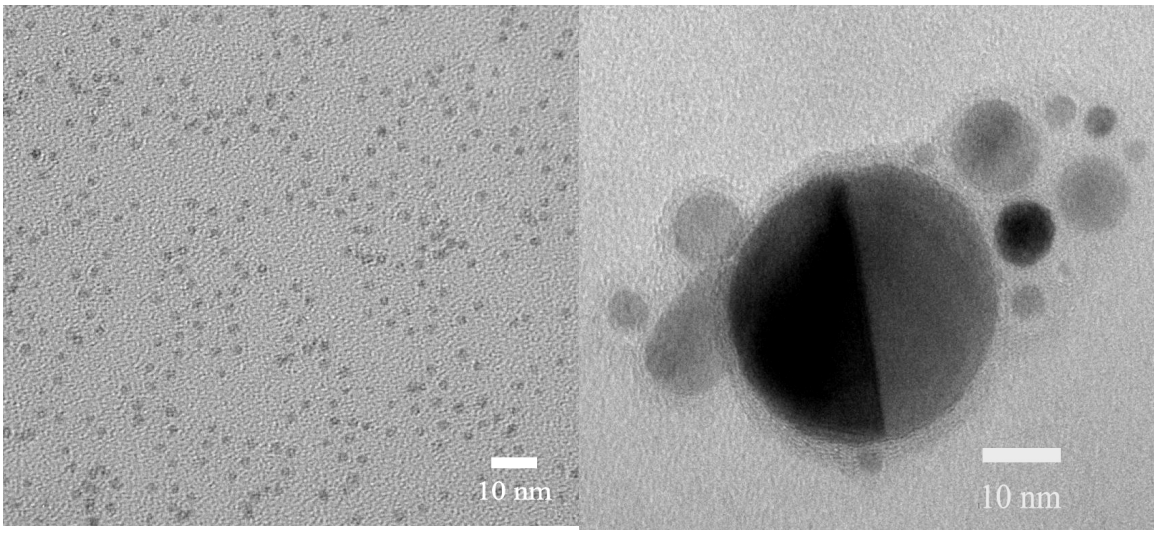

Figure 4.13 TEM image of the (a) as-synthesized 2 nm FePt nanoparticles. (b) annealed FePt nanoparticles

In the equal atomic FePt phase, magnetic hardening shown by the coercivity, is based on the fcc-fct phase transition. The as-synthesized fcc particles were deposited on Si substrate and annealed in forming gas above 500°C for 1 hour. We tested several temperatures and 650ºC was found to give the highest coercivity. The composition of the FePt nanoparticles is tuned via the initial molar ratio of Fe(acac)3 and Pt(acac)2 precursors in the reaction. Based on 1 mmol of Pt(acac)2 and 0.5 mmol each of oleic acid and oleyl amine and 20 ml of octyl ether, varying the molar amount of Fe(acac)3 , the resulting FePt particle compositions are shown in figure 4.14.

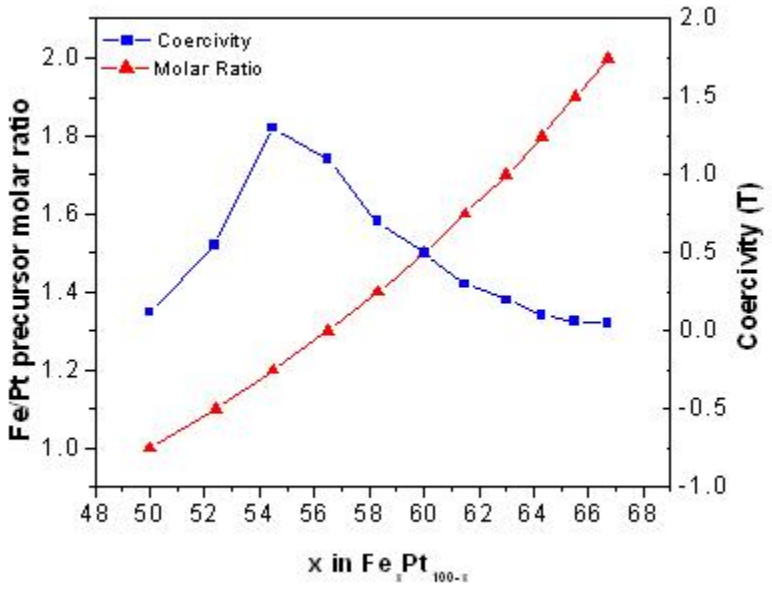

Figure 4.14 Composition dependence of coercivity.

The resultant compositions of Fe and Pt are average compositions determined by EDX. It was observed that precursor molar ratio of 1:1 yielded $Fe_{50}Pt_{50}$ particles while 2:1 led to $Fe_{67}Pt_{33}$ nanoparticles, which shows that unlike reactions where $Fe(CO)_5$ was

used [35], all the $Fe(acac)_3$ contributes to the FePt formation because of low precursor volatility at the reaction temperature of 295°C. In the same figure, coercivity dependence of the annealed FePt nanoparticles thin film assemblies with different percentage of Fe is also shown. The highest coercivity achieved was 19,000 Oe at $Fe_{55}Pt_{45}$ similar to the previous results [35]. However, if the reflux time during the reaction was increased from 30 minutes to 4 hours, the particle assembly resulted in a huge coercivity of 27,000 Oe after annealing at similar conditions as shown in figure 4.15. The very high coercivity can be related to the high degree of chemical ordering within the fct phase across the particle assembly. As the refluxing time was increased, the chemical composition of particles became more homogeneous allowing the particles to achieve a higher percentage of fct phase by maintaining the atomic composition closer to unity, which leads to high degree of chemical ordering in the nanoparticles and the assemblies. The high chemical ordering gives rise to the high magnetocrystalline anisotropy, which can result in the huge coercivity of these nanoparticle assembled thin films.

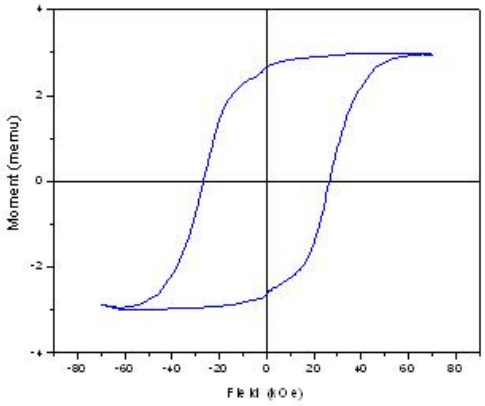

Figure 4.15 Magnetic hysteresis loop of the annealed assembly

4.5 Size and Shape Control of FePt Nanoparticles

4.5.1 FePt Particle Size Results

Figure 4.16 shows XRD patterns of as-synthesized FePt nanoparticles of 2 to 9 nm with an approximately 1 nm difference. It can be seen that the peak width decreases as the particle size increases, and also from the XRD pattern that these particles exhibit a face-centered cubic (fcc) crystal structure. TEM images of these nanoparticles are shown in figure 4.17.

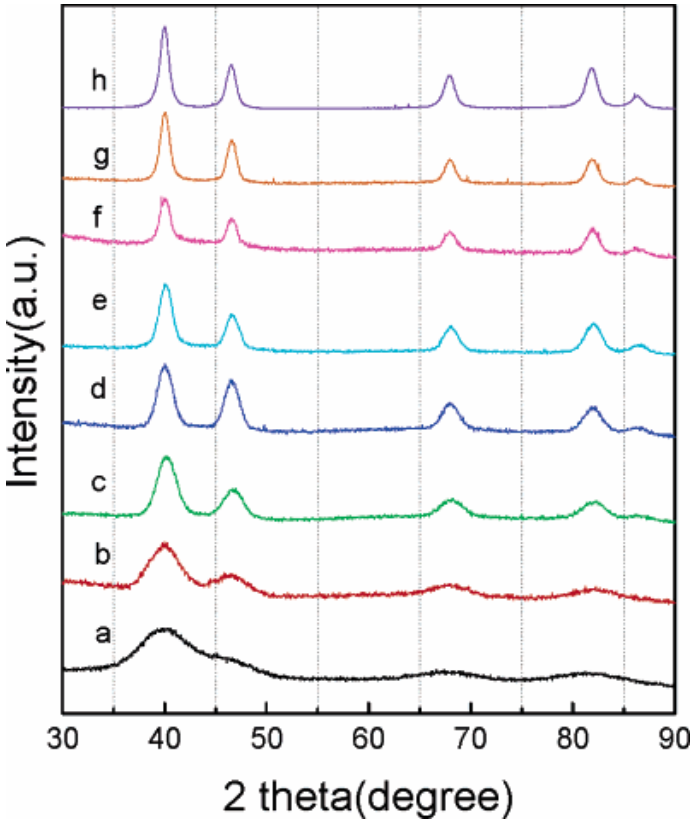

Figure 4.16 XRD curves as-synthesized FePt nanoparticles of size (a) 2 nm (b) 3 nm (c) 4 nm (d) 5 nm (e) 6 nm (f) 7 nm (f) 8 nm and (g) 9 nm.

The formation mechanism of FePt nanoparticles has been previously reported for similar methods [51 77 82]. At the early stage of the synthesis, Pt-rich nuclei are formed from the reduction of $Pt(acac)_2$ and the slow decomposition of $Fe(CO)_5$. As the Fe atoms continue to form, they attach to the nuclei surface then diffuse into the Pt-rich nuclei once heated to reflux temperature (approx. 300°C) until complete depletion of the $Fe(CO)_5$.

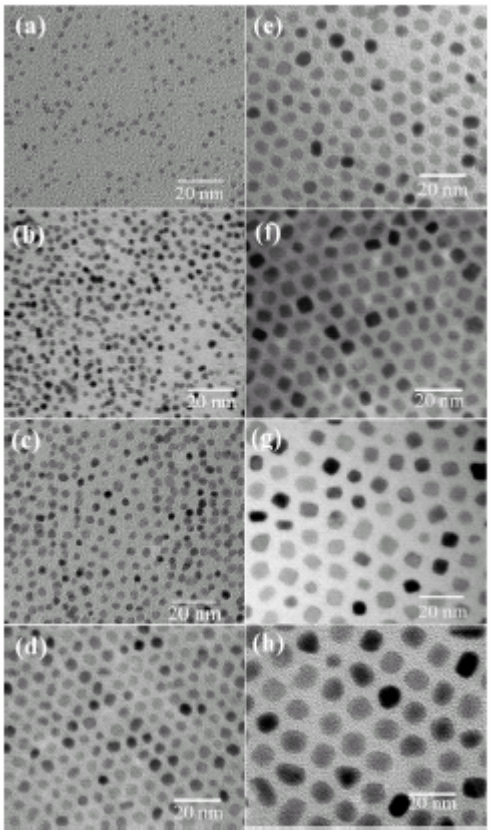

Figure 4.17 TEM image of as-synthesized FePt nanoparticles of size (a) 2 nm, (b) 3 nm, (c) 4 nm, (d) 5 nm, (e) 6 nm, (f) 7 nm, (g) 8 nm, and (h) 9 nm.

The size of the Pt-rich nuclei is dependent on the free energy of the system, which can be controlled by varying the reaction parameters. For polydisperse particle nuclei,

compositional variances occur due to the differing growth rates as a result of smaller nuclei possessing a higher chemical potential. As particle sizes become uniform, the smaller particles will be rich in Fe compared to the larger particles. Refluxing the reaction mixture above 295°C allows atomic diffusion of the Fe and Pt leading to the formation of disordered fcc FePt nanoparticles.

4.5.2 Surfactant Effects on Particle Size

Surfactants typically play a crucial role in controlling the size and shape of chemically synthesized nanoparticles. Oleic acid and oleyl amine were chosen in our synthesis as they work as ideal ligands for FePt nanoparticles. The surfactants to $Pt(acac)_2$ molar ratio was studied to determine the size effect on the FePt nanoparticles. The heating rate of the reaction was maintained at 5 °C/min. FePt nanoparticles with average size of 4 nm (Figure 4.17(c)) were obtained when the molar ratio of surfactants to $Pt(acac)_2$ was 1. By decreasing the molar ratio to 0.75, the particle size decreased to 3 nm (Figure 4.17(b)) whereas by increasing the molar ratio up to 10, the particle size increased to 9 nm (Figure 4.17(h)). It is clear that the particle size increases with increasing surfactant concentration, but after a certain concentration of surfactants the size did not change (Figure 4.19). The resultant size change of the nanoparticles is thought to be the result of the modification in the number of nuclei at the first step of particle formation usually referred to as “burst nucleation”. The increase in the surfactant amount acts counter-intuitively on the resulting particle size when the heating rate is held constant since it results in an increase in size. The critical size equation for nucleation if

assuming a spherical particle shows a balance among the key variables of temperature, solid-liquid interfacial energy and the supersaturation.

$$r_c = \frac{2\Omega\gamma_{SL}}{RT\sigma} \qquad 4.1$$

Assuming the solid-liquid interfacial energy remains constant, the additional surfactant then modifies the solution chemistry resulting in the formation of stable complexes with individual metal atoms (or dimers, trimers, etc.) from the molecular precursor. Therefore, an increase in surfactant concentration is expected to raise the solubility; thereby, lowering the supersaturation index, σ, of the formed atoms and as a consequence, larger particles are nucleated as seen from equation 4.1.

4.5.3 Heating Rate Effects on Particle Size

The heating rate of reaction mixture was also found to be very important in the fine-tuning of the particle size. To analyze the size change with the heating rate of the reaction mixture, surfactant to precursor ratio identical to that used to synthesize 8 nm particles (Figure 4.17(g)) was chosen. As the heating rate was increased from 5 to 10 and then to 15 °C/min, we found that the average particle size decreased from 8 to 7 and then to 6 nm (Figure 4.17(f) and 4.17(e)), respectively. With the increase in the heating rate, the temperature at which nucleation occurs was modified. As a result of the elevated temperature, the critical radius at nucleation was decreased. The nucleation rate was also increased as seen from equations 2.13 and 2.15 resulting in more nuclei forming at the initial stage. Consequently smaller particles were produced. On the other hand, the correlation between the heating rate and the particle size is not monotonous. When the

heating rate is very low, smaller particles were produced. For example, when the heating rate was decreased to 1 °C/min, surprisingly, the particle size decreased to 5 nm.

The complex nature of the process used to form the nanoparticles is evident from theses results and warrants further discussion and future work. A quick review of the surfactants used in the system, oleic acid and oleyl amine, are reactive within the temperature ranges used leading to a continual depletion of the surfactants throughout the process and formation of an amide (figure 4.18). The heating rate then determines the rate of depletion of the surfactants. Moreover, this depletion leads to a continual change in the free energy and possibly the kinetics of the system.

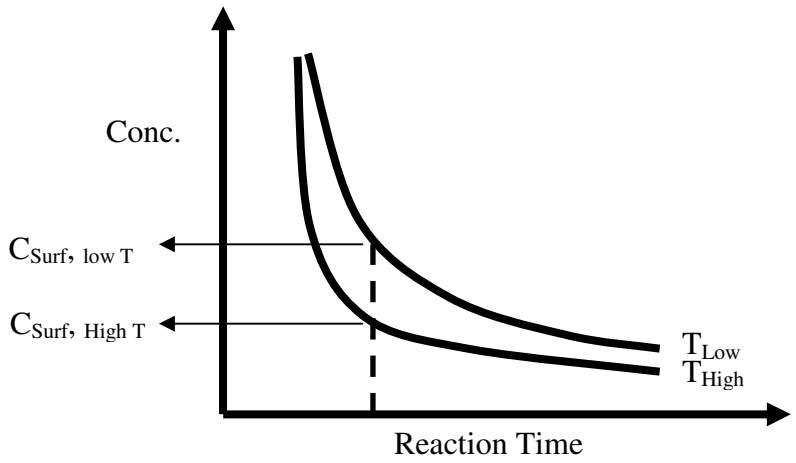

Figure 4.18 Graphic depicting the differences in the total concentration of the surfactants at a function of temperature and time.

The data in figure 4.19 suggests that at the lower heating rates when the surfactant charge is held constant, surfactant reduction due to amide formation occurs much slower, leaving a higher concentration of surfactant during nucleation than for reactions carried out at a faster heating rate. Equation 4.1 would predict an increasing particle size if other

variables were held constant based on the expected increase in the interfacial energy as the surfactant concentration decreases.

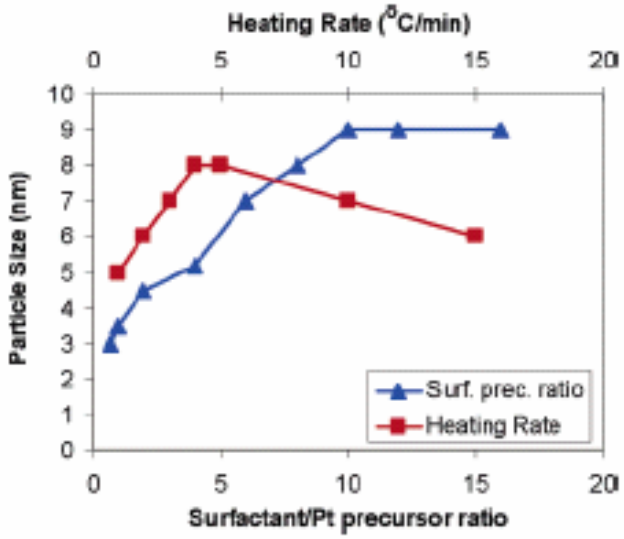

Figure 4.19 Heating rate and surfactant/Pt precursor dependence on particle size.

Based on the effect of the surfactants on the monomer solubility, which is directly proportional to the surfactant concentration, it would be expected that the average particle size would be larger at lower heating rates since more surfactant would be expected to be present. Moreover, the lower heating rate would also suggest potentially a lower temperature at nucleation leading to a larger particle size. However, the monomer-ligand-temperature effect on the monomer activities is not known, which if dramatic reductions in monomer concentration occur as a function of decreasing temperature could dominate the resulting particle size that is nucleated due to the change in the supersaturation index. Although the interactions have not been modeled by this group,

the resulting non-linear effect could then explain the changes to the particle size as a function of heating rate.

$Fe(CO)_5$ was used as the iron source to synthesize particles from 3 to 9 nm. However, particle sizes below 3 nm were not obtained using $Fe(CO)_5$. To study the effect of precursors on the particles size, $Fe(CO)_5$ was replaced by $Fe(acac)_3$, while keeping all the synthetic conditions same. When $Fe(acac)_3$ was used, 2 nm particles were obtained (Figure 4.17(a)). It is not known why the $Fe(acac)_3$ leads to a smaller particle size although it can be suggested the ligands from the acetylacetonate (acac) allow a much higher supersaturation to occur through rapid decomposition, effectively lowering the particle size. Although the amount of surfactant and heating rate were varied, particle size was always found to be 2 nm when $Fe(acac)_3$ was used as the iron precursor.

4.5.4 Solvent Effects on Particle Size

Solvents provide the media for particles to nucleate and grow. The correct composition of Fe and Pt is required to form the desired phase. A solvent with high boiling point and chemical stability at higher temperature is required to achieve the correct composition of FePt through diffusion. Because of its stability at reflux temperature (295°C), octyl ether is a commonly used solvent for FePt nanoparticle synthesis. However, octyl ether is a very expensive solvent; therefore, benzyl ether was used as an alternative solvent for the experiments. When benzyl ether was used as a solvent, monodisperse spherical particles with narrow size distribution were obtained. Nevertheless, it was very difficult to maintain the reflux temperature since it released some low-boiling point byproducts at high temperature (above 280 °C), which resulted in

lowering the temperature of the reaction mixture. As a result, separate experiments were evaluated in octyl ether and benzyl ether. Interestingly, faceted cubic shape (Figure 4.20(b)) FePt nanoparticles instead of the spherical ones (Figure 4.20(a)) were obtained when octyl ether was used as the solvent. However, this shape change was only observed in particles larger than 7 nm but was hard to find in the smaller particles.

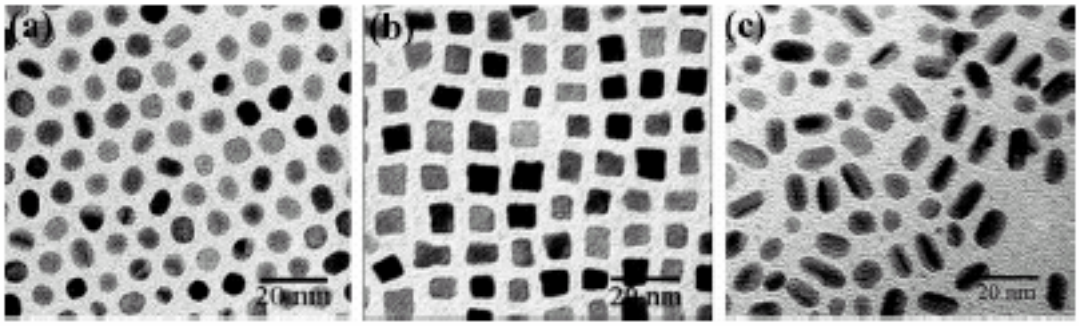

Figure 4.20 TEM image of (a) spherical, (b) cubic, and (c) rod-shape FePt nanoparticles.

4.5.5 Effect of Surfactant Injection on Particle Shape

The time interval of surfactant injection into the reaction mixture is another factor that influences the particle shape. In our synthesis procedure, both of the surfactants were injected simultaneously a few seconds after the injection of $Fe(CO)_5$. However, when using benzyl ether as a solvent, delaying the injection of oleyl amine 5 min after the injection of oleic acid resulted in rod shape nanoparticles (Figure 4.20(c)). The same results were not observed when octyl ether is used as the solvent. The mechanism of rod formation has is not well understood at this stage. This is an interesting finding because

rod shape nanoparticles are good candidates for anisotropic nanomagnets as they may be aligned by virtue of their shape.

CHAPTER 5

MONODISPERSE $L1_0$ FePt NANOPARTICLES

5.1 Introduction

For particle compositions in the range of approximately 45 – 65 atomic percent Fe, rearrangement of the chemically disordered fcc phase to the thermodynamically stable $L1_0$ phase occurs leading to an alternating layer of iron and platinum atoms with a c/a ratio equal to 0.964 [83]. A graphical representation of the transition to the $L1_o$ structure is shown in figure 5.1. Extensive efforts have been made since 2000 to obtain monodisperse fct FePt particles because the magnetically anisotropic phase possesses a magnetocrystalline constant of 6.6 MJ/m^3 (see appendix A), which can be formed by annealing of the chemically synthesized particles at 550°C [74]. Unfortunately, annealing usually leads to sintering of the particles resulting in large particle sizes and broad size distributions.

One of the approaches in such efforts is to lower the onset temperature for the fcc to fct phase transformation. Doping by elements such as Ag, Au and Cu in the FePt phase was tested resulting in the onset of the fct phase at 400°C [84-89]. Direct synthesis of the fct structured particles by the polyol process using high boiling point solvents is another major approach [90-93]. In this approach, higher synthesis temperatures can be applied which allows partial formation of the fct phase. Recently, fcc FePt nanoparticle arrays with coating were annealed at temperatures higher than

700°C without sintering. An immiscible silica matrix [94], or polyethyleneimine linker molecules [95] were used as the coating materials. The coating approach, however, was only suitable for monolayers of the separated nanoparticles on substrates. Other approaches to obtaining monodisperse fct nanoparticles include rapid thermal annealing [96] and pulse laser annealing [97]. To date, all the reported approaches have been only successful in obtaining partially transformed fct nanoparticles and high coercivity has not been developed from the partially transformed particles. It is therefore highly desirable to find processing techniques to produce completely transformed fct FePt nanoparticles.

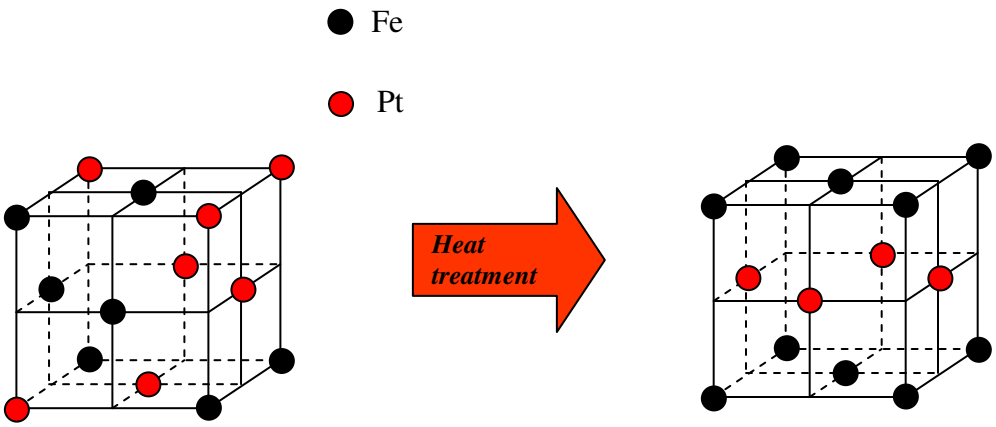

Figure 5.1 Transition of the chemically disordered fcc FePt unit cell to the magnetically anisotropic $L1_o$ FePt unit cell.

Our experimental concept is based on isolating the FePt nanoparticles with sufficient NaCl during annealing to prevent sintering. K. Sato and coworkers [98] used (001) NaCl crystals to deposit Pt then Fe by electron beam evaporation to study substrate temperature effects on the particle magnetic properties and surface structure interactions. It was found that an anchoring interaction between the substrate and deposited Pt

prevented coalescence of the FePt during annealing up to 600°C. When the NaCl substrate was slightly angled, from the [001] direction, the exposed ledges resulted in a higher density of particles per unit area.

Ball milling of sodium chloride down to micron sizes would substantially increase the number of ledges available for pinning the chemically synthesized fcc FePt nanoparticles allowing production of large quantities of hard magnetic nanoparticles. Subsequently, mixed phases of magnetic materials can be carefully controlled, structured and studied in efforts to advance many technologies using magnetic materials.

Studies on size dependent chemical ordering of FePt nanoparticles published by Y.K. Takahashi [99] and experimental confirmation by T. Miyazaki [100] suggest that fcc FePt particles may not undergo the chemical ordering if the diameter particle diameter is within 2 - 4 nm depending on the model used to make this determination. Calculations by Chepulskii [101] indicated that 3.5 nm particles should reach a long-range order parameter of 0.84, and the lack of transition to the fct when annealed at 600°C was limited by kinetics.

With the development of the salt-matrix annealing technique, which allows the conversion of the fcc FePt to the magnetically anisotropic phase without significant sintering, studies on the long range ordering of fcc FePt to $L1_0$ FePt can be systematically explored, testing the validity of the predictions on the particle size barrier to ordering. In addition, magnetic characteristics of assemblies of $L1_0$ FePt particles can be measured in an effort to understand the reduced dimensional characteristic and their inter-particle interactions relative to bulk FePt magnetic properties.

5.2 New Method for Isolated $L1_o$ FePt Nanoparticles

Figure 5.2 shows XRD patterns of the annealed FePt nanoparticles in NaCl matrix under different conditions. It can be seen clearly that well defined (001) and (110) peaks for fct FePt appear for samples annealed at 700°C for 2 hours in forming gas. Diffraction peaks associated with NaCl or any other phases were not found from the XRD patterns, which indicates a minimal contamination by the salt during the annealing. ICP analysis confirmed a low level of Na contamination of 0.099% (wt/wt basis) and an average particle composition of $Fe_{52}Pt_{48}$.

Magnetization of the salt-matrix annealed FePt nanoparticles were measured to check if there was any deterioration caused by contamination from the salt matrix during the annealing or from the water exposure during washing. For the recovered particles of 15 nm with salt to particle ratio of 40:1, for instance, the magnetization values at 7 T at room temperature (which are considered to be close to the saturation magnetization) are listed as follows: annealed at 600°C for 2 hours, 733.5 emu/cm^3; 700°C, 2 hours, 744 emu/cm^3; 700° C, 4 hours, 841.5 emu/cm^3. These magnetization values are comparable to FePt particles annealed under the same conditions without salt. It is seen that the magnetization values increase with the annealing time and temperature, indicating a phase-transition (from disordered fcc to ordered fct structure) related increase in the magnetization. The higher the degree of the chemical order, the higher the magnetization. A completely ordered fct bulk phase possesses very high saturation magnetization (1140 emu/cm^3 at room temperature [77]). The relatively low magnetization values at 7 T of the nanoparticles even after sufficient annealing may be attributed to

reduced magnetic moment of the surface atoms of the nanoparticles and the fact that 7 T field is not enough to reach the saturation.

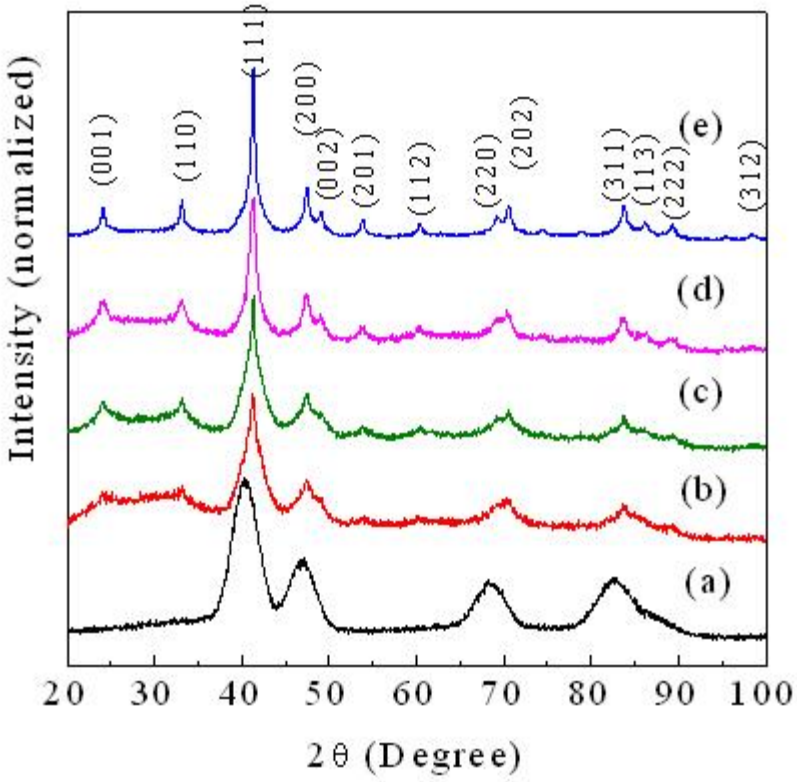

Figure 5.2 XRD patterns of the FePt nanoparticles. (a) the as-synthesized 4nm FePt and (b) particle annealed at 600°C for 2 hrs with NaCl:FePt ratio 40:1 (c) at 700°C for 2 hrs with the ratio 1:40 (d) 700°C for 4 hrs with the ratio 100:1 and (e) 700°C for 4 hrs with the ratio 40:1.

Morphology of the salt-matrix annealed nanoparticles was closely monitored by TEM observations. It was found that the annealed particles aggregate easier than the fcc particles because of the magnetic attractive force between the fct particles. This kind of aggregation can be re-dispersed by ultra-sonic vibration. Monodisperse nanoparticles can

still be observed if the particles are properly deposited on TEM observation grids. Figure 5.3 shows images of the particles annealed at 700°C for 2 hours. It can be seen clearly that this methodology has successfully prevented the particles with sizes from 4 to 15 nm from sintering and growing at 700°C, which is sufficient enough a temperature to transform from the fcc to the fct phase.

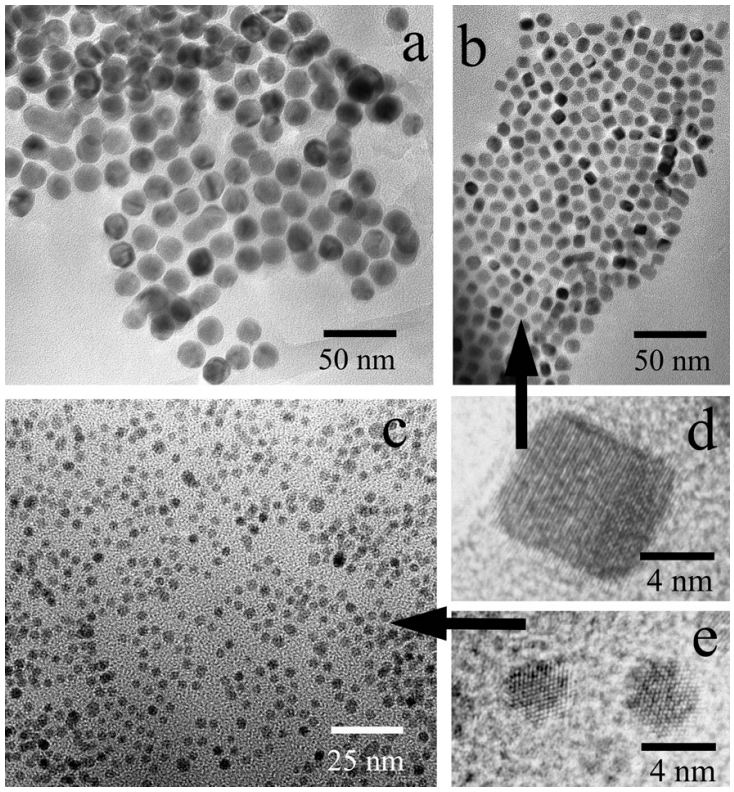

Figure 5.3 TEM images of salt-matrix annealed fct FePt particles annealed at 700°C for 2 hours. (a) 15 nm with NaCl:FePt ratio of 100:1; (b) 8 nm with the ratio of 40:1; (c) 4 nm with the ratio of 40:1; (d) and (e) are the high resolution TEM images for (b) and (c), respectively.

The salt ratio to fcc FePt particles can be increased to suppress the sintering of the nanoparticles when annealing at higher temperatures or longer times. When the ratio is lower than 20:1, monodisperse fct nanoparticles cannot be obtained from heat treatments at 700^{o}C for 2 hours. Lower salt ratios gave significant particle sintering and agglomeration (figure 5.4). Annealing at higher temperatures and extended time should be accompanied with higher salt to FePt ratio in order to avoid sintering. From our experimental observations, salt particle size has no significant effect on the annealing and the presence of salt has not altered the fcc to fct transition temperature.

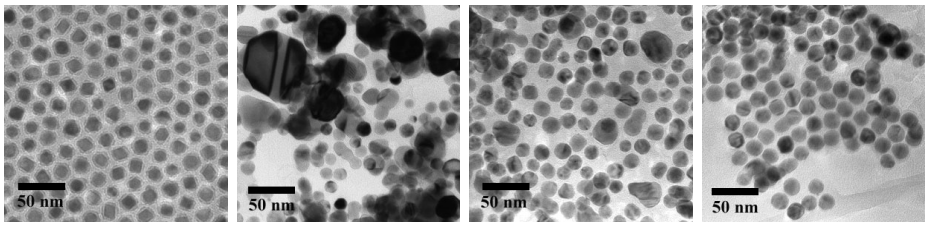

Figure 5.4 TEM images of salt-matrix annealed fct FePt particles annealed at 700^{o}C for 2 hours. From left to right are the as-synthesized fcc FePt particles and fct FePt particles from 4:1, 40:1 and 100:1 salt ratios.

From figure 5.4(b) and (d) it can be seen that most of the 8 nm particles have cubic or rectangular shape, as their precursors before the annealing, indicating that nanoparticle shapes can be retained with this heat treatment technique. Therefore, this technique can be readily applied to heat treatments of nanorods, nanowires and other isolated micro- and nanostructures as long as they can be mixed with salt powders and the salt contamination can be avoided.

The major reason for the great interest in FePt nanoparticles is that fct FePt phase has very high magnetic anisotropy and therefore, fct FePt nanoparticles should have high coercivity as long as their size is above the superparamagnetic critical dimension. The annealed particles were mixed with epoxy and aligned in a magnetic field of 7 T. After the epoxy dried the magnetization loops were measured with a SQUID magnetometer in different directions. Not surprisingly, the particles exhibited giant coercivity up to 30 KOe at room temperature (see Fig. 5.5). In all the cases of the annealed particles, when the XRD patterns show the fct structure, coercivity values of the isolated particles in epoxy are normally above 15 KOe at room temperature. It is interesting to note that the 8 nm particles have higher coercivity than the rest. From Fig. 5.5, it can be also seen that the demagnetization curves of the 4 and 8 nm particles show kinks with relatively low saturation magnetizations, indicating a two-phase magnetization behavior, which may be related to inhomogeneous composition.

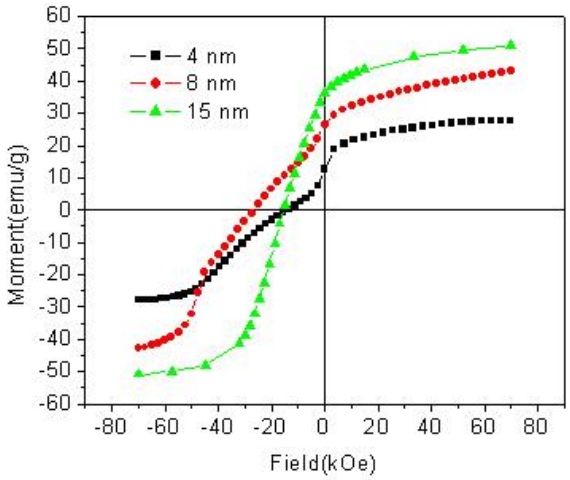

Figure 5.5 Demagnetization curves of the annealed fct FePt nanoparticles with 4, 8 and 15 nm particle size. The annealing was performed in NaCl matrix at 700^{o}C for 4 hrs in forming gas. The ratio FePt:NaCl = 1:100. The particles were embedded in epoxy.

5.3 Size Dependent Ordering and Characterization of $L1_o$ FePt Nanoparticles

5.3.1 fct FePt Size by XRD and TEM

Chemically disordered fcc FePt nanoparticles synthesized by the methods mentioned in section 3.2.2 were prepared in the NaCl matrix as described in section 3.2.3 and annealed for 2 hours at 600°C, 2 hours at 700°C and 4 hours at 700°C in an Ar / 7% H_2 atmosphere. Powder XRD was used to determine particle size changes before and after thermal annealing of the FePt in conjunction with TEM imaging to give an overall assessment of the particle assemblies. Particle sizes were calculated through the use of the Scherrer formula [102]:

$$L = \frac{0.94\lambda}{B(2\theta)\cos\theta} \tag{5.1}$$

Where λ is the Cu Kα wavelength of 0.154 nm, B(2θ) is the full width at half maximum in radians of the (111) peak. Peak patterns were fit using a Pearson VII profile and size estimates determined from this profile. Figure 5.6 shows the particle size results of the fcc FePt particles derived from powder XRD data compared to TEM images. It is apparent the particle sizes calculated from the XRD data match reasonably with the TEM images, which confirms the particles sizes are uniform throughout the sample.

The annealed samples were analyzed by powder XRD to reveal the extent on conversion from the fcc to fct phase which is shown in figure 5.7. As the annealing temperature and time was increased, the development of the (001) and (110) become more evident which is indicative of the additional reflection that would develop from the superlattice of alternating plane of Fe and Pt in the ordered structure. Additionally, a

split in the (200) peak developed typically under annealing conditions at 700°C at 2 hrs as would be expected as the lattice transforms from the fcc to fct phase.

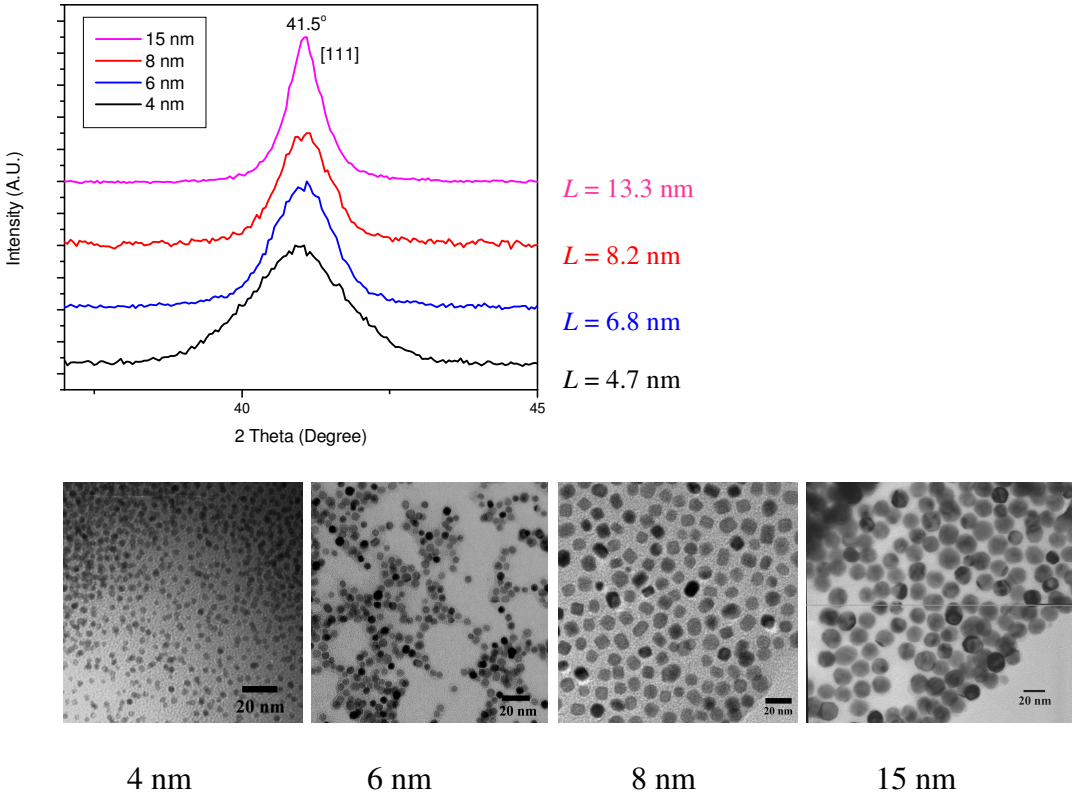

Figure 5.6 Comparison of XRD derived particle sizes from equation (5.1) compared to TEM images for fcc FePt.

5.3.2 Chemical Ordering of fct FePt Nanoparticles

A comparison of the XRD patterns for 2, 4, 6, 8 and 15 nm FePt particles annealed at a NaCl to FePt weight ratio of 400:1 at 700°C for 4 hr in an Ar / 7% H_2 atmosphere is shown in figure 5.8. A clear dependence on the level of transformation

from the fcc to fct phase is seen as a function of particle size with the 2 nm particles containing fcc FePt based on XRD data.

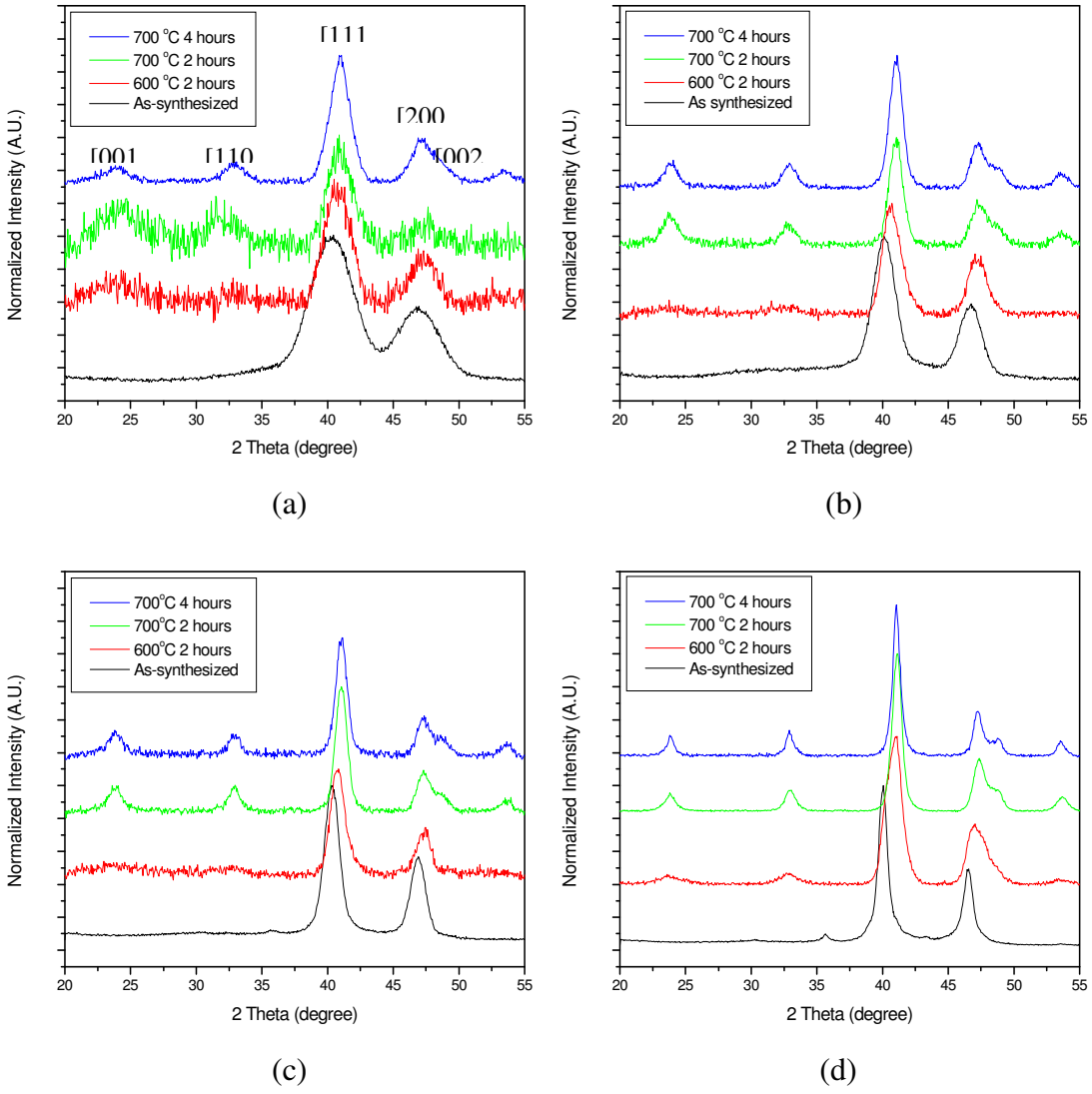

Figure 5.7 XRD patterns of as-synthesized and annealed FePt nanoparticles with diameters of (a) 4 nm, (b) 6 nm, (c) 8 nm and (d) 15 nm.

Long range ordering of the annealed nanoparticles can be evaluated by powder XRD through the use the following equation [103-105]:

$$S \approx 0.85\left(\frac{I_{super}}{I_{fund}}\right)^{\frac{1}{2}} \qquad (5.2)$$

Where I_{Super} is the intergrated area associated with the superlattice peak reflection and I_{Fund} is the intergrated area associated with the fundamental peak reflection. The (001) as the superlattice and (002) as the fundamental reflection was chosen for this study [105].

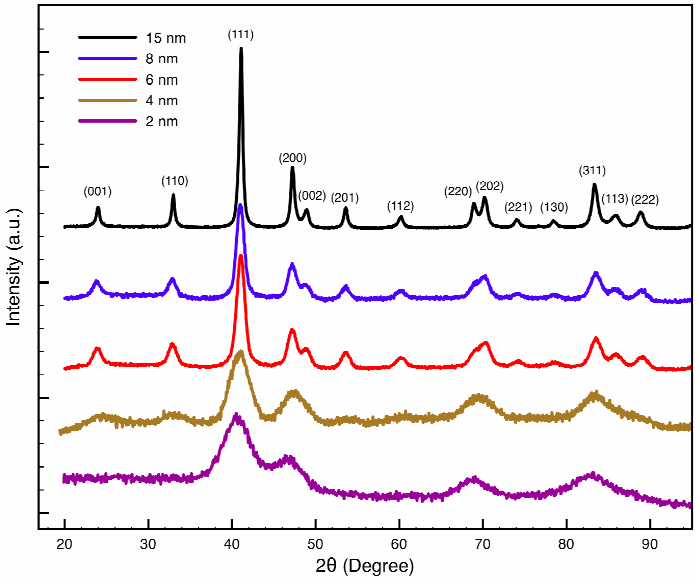

Figure 5.8 XRD patterns of fct FePt nanoparticles with diameters of 2, 4, 6, 8, and 15 nm annealed at 700°C for 4 hrs in an Ar / 7% H_2 atmosphere. A NaCl to FePt ratio of 400:1 was used during annealing.

The results of the calculated long-range order parameter for the 4, 6, 8 and 15 nm particles annealed at differing temperatures are shown in figure 5.9. Maximum long-range ordering was achieved in annealing conditions of 700°C for 4 hrs. The ordering trend increases with larger particle sizes reaching a maximum at 8 nm before decreasing

at 15 nm. The decrease in ordering of the 15 nm fct FePt may be a result of compositional variation within the particles since the larger particles are grown from 10 nm Pt cores then coated by Fe_3O_4. Reduction in forming gas reduced the oxide allowing the Fe and Pt to inter-diffuse.

When the coercivity of the fct FePt particles is plotted as a function of particle size, a similar trend to that of the ordering parameter occurs as seen in figure 5.10 with the 8 nm particles achieving the highest coercivity. The decreased coercivity of the 15 nm particles can be attributed to the polycrystalline nature of the particles and compositional variation. The full hysteresis of the 4, 6, 8 and 15 nm particles annealed at 600^{o}C for 2 hrs, 700^{o}C for 2 hrs and 700^{o}C for 4 hrs is shown in figure 5.11. The 4 and 6 nm FePt particles annealed at 600^{o}C for 2 hrs show superparamagnetic behavior with the exception of the 8 and 15 nm particles, which developed coercivity. At higher temperatures, hard phase magnetic characteristics developed. The 2 nm fcc FePt particles shown in figure 5.12 remained superparamagnetic even under annealing conditions of 700^{o}C for 8 hrs, which when coupled with the XRD data confirm that a size boundary to transitioning from the fcc to fct phase as mentioned in several publications [100-102] lie in the 2 – 4 nm region.

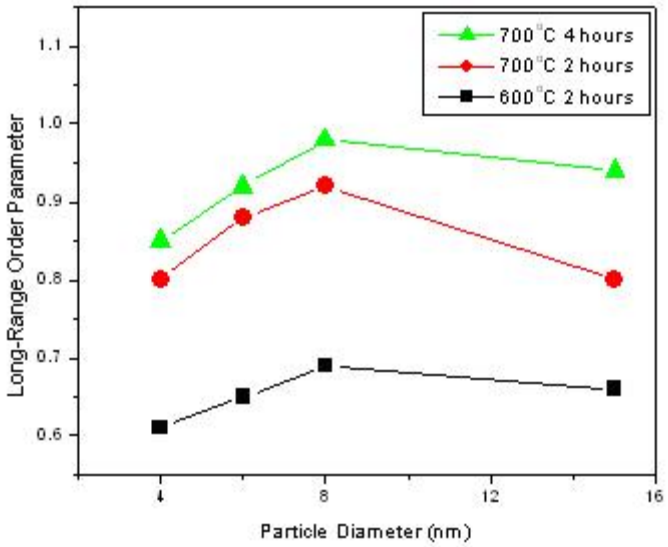

Figure 5.9 Long-range order parameter vs. particle diameter for different annealing conditions. 2 nm results are omitted since only the fcc phase was detected in the particles.

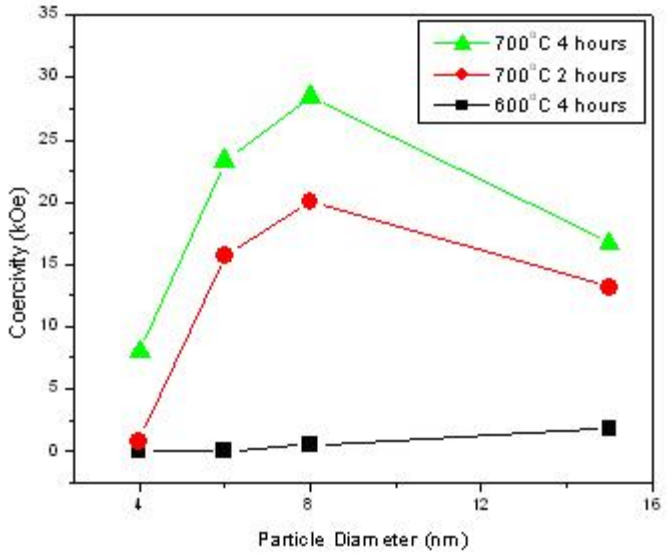

Figure 5.10 Coercivity vs. particle diameter for different annealing conditions. 2 nm results are omitted since coercivity did not develop in any of the annealed samples.

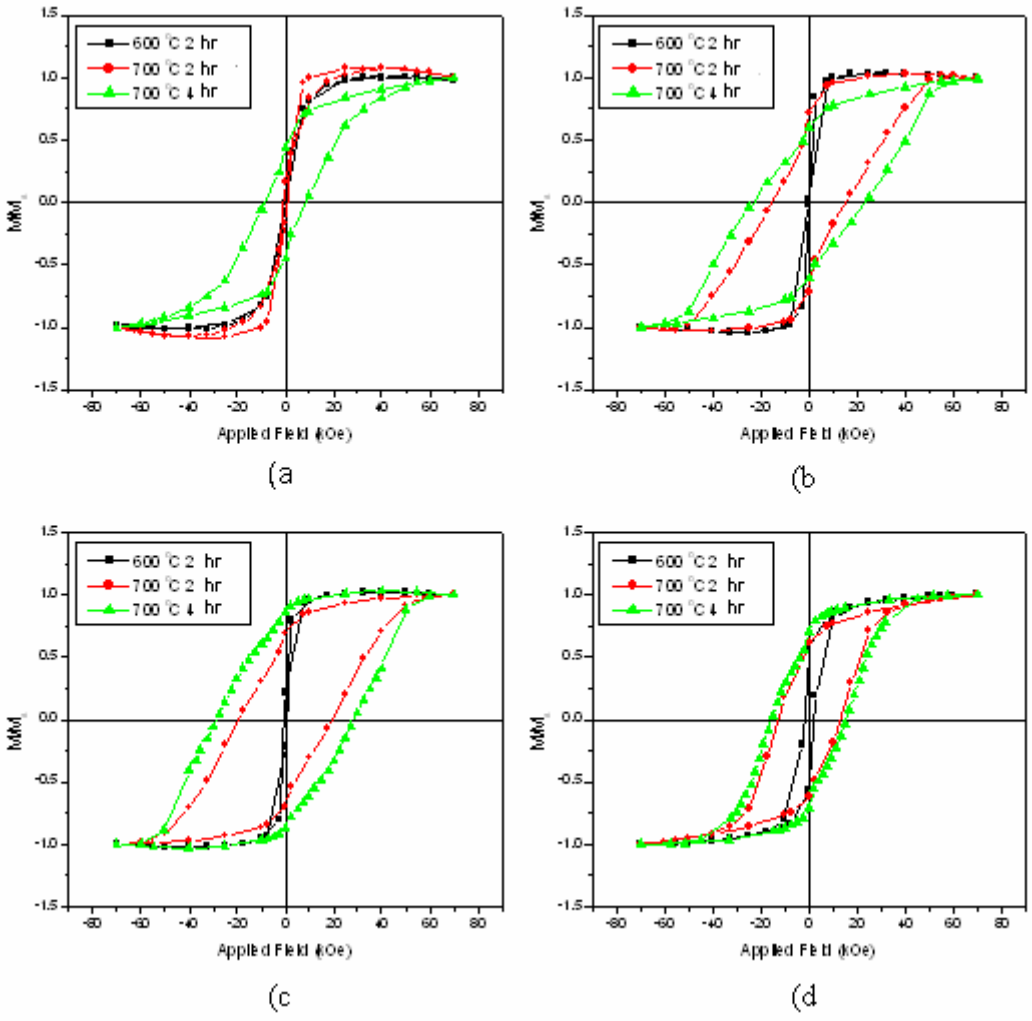

Figure 5.11 Hysteresis loops of FePt nanoparticles with diameters of (a) 4 nm, (b) 6 nm, (c) 8 nm and (d) 15 nm annealed in different conditions.

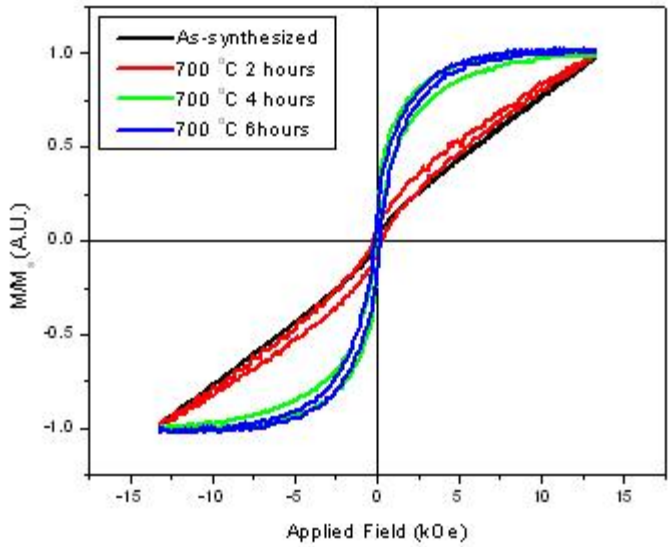

Figure 5.12 Hysteresis loops of 2 nm FePt nanoparticles annealed in salt-matrix in different conditions.

5.3.3 Size Boundary to Chemical Ordering

The size limitation on chemical ordering of FePt is not apparent from the phase diagram in figure 5.13; moreover, surface diffusion would be expected to enhance the mixing of the iron and platinum based on the large surface area to volume ratio of the nanoparticles. Calculations on thermodynamic ordering conducted by Takahashi et al. [106] using the Bragg-Williams approximation to calculate the Helmholtz free energy assuming free surfaces, and spherical particles and using Lennard-Jones potentials to calculate the internal energy indicated a size limitation to chemical ordering occurring at 1.5 nm. This effect was described as a thermodynamic depression in the ordering temperature, resulting in the chemically disordered state being energetically favored at an annealing temperature of 600°C. In effect, the annealing temperatures required to

promote diffusion would cross the ordering temperature leading to a chemically disordered state.

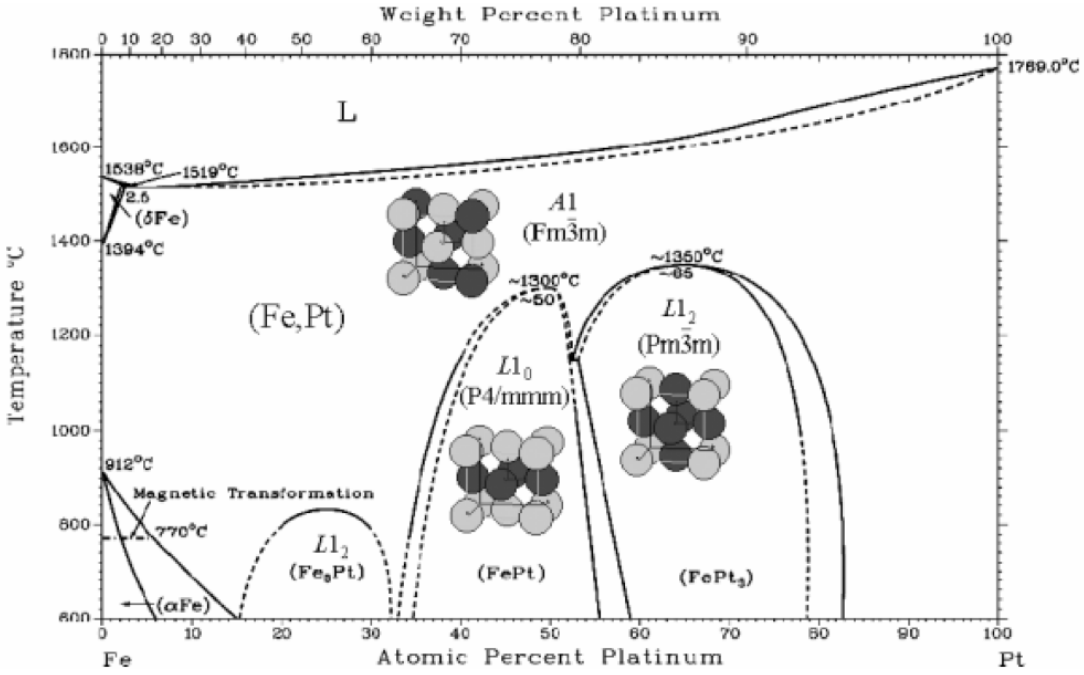

Figure 5.13 Phase diagram of FePt system from reference. [107]

Additional studies by Takahashi et al. using the diffuse-interface theory [99] assuming an isotropic system, homogeneous composition, spherical particles and a system at 600°C, showed that the ordered state of the particle becomes unstable when the size is less than 2 nm. Since the particle interface was considered disordered, the degree of chemical ordering driven strictly by particle size. However, if the interfacial energy could be modified without changes to the particle size, the level of chemical ordering

could possible be altered. This study essentially supported their previous work on the size limitation of chemical ordering in FePt.

Chepulskii et al.[101] performed a thorough study on the equilibrium order parameter for FePt using the Connally-Williams method to calculate the mixing potentials for equiatomic FePt and the Korringa-Kohn-Rostoker coherent potential approximation for comparison then using Monte Carlo simulations and the analytical ring approximation for calculation of the order parameter showed good correlation with experimental values. Based on this simulation work, the equilibrium chemical ordering for a 3.5 nm FePt nanoparticle of equiatomic composition would reach 0.84 at 600^{o}C. Lower values of ordering at this size would then be a function of kinetics. Noted in this study was the potential for surface segregation of the Fe or Pt, which would in effect reduce the ordering of the particles due to non-equiatomic compositions within the particle.

5.3.4 Alignment of fct FePt Nanoparticles

It is expected that the fct particles with magnetocrystalline anisotropy can be aligned in a magnetic field and therefore, the hardened epoxy specimens should give different magnetization curves in different directions. However, it was observed that no obvious difference could be found in the magnetization curves measured in the parallel and perpendicular directions. One possible reason for this phenomenon is that the fct particles (each of them is a small permanent magnet) attract each other to form large aggregations, which makes the rotation of individual particles difficult. Another reason may be that it is difficult to rotate the very fine nanoparticles with 7 T field in epoxy

because of the friction. The high viscosity of epoxy and the huge surface area of the nanoparticles can make the friction extremely high. Alignment with a higher magnetic field may be needed.

To reduce the friction, alignment of the particles in alcohol and water was performed in a magnetic field of 7 T. The specimens were cooled down in the magnetic field from room temperature at which alcohol and water are liquids, to temperatures below the freezing points for alcohol and water and then the demagnetization curves were measured. These curves were then compared with the curves measured for samples cooled without magnetic field (randomly aligned particles). Figure 5.14 shows the demagnetizing curves measured from the aligned particles and random particles in frozen alcohol at 10 K. Differences in the aligned and random sample have been observed, although the significance is not completely known since the possibility of experimental error could have caused the differences. However, we were not able to saturate the magnetization with 7 T magnetic field at 10 K. No kinks were observed in these minor-loop curves.

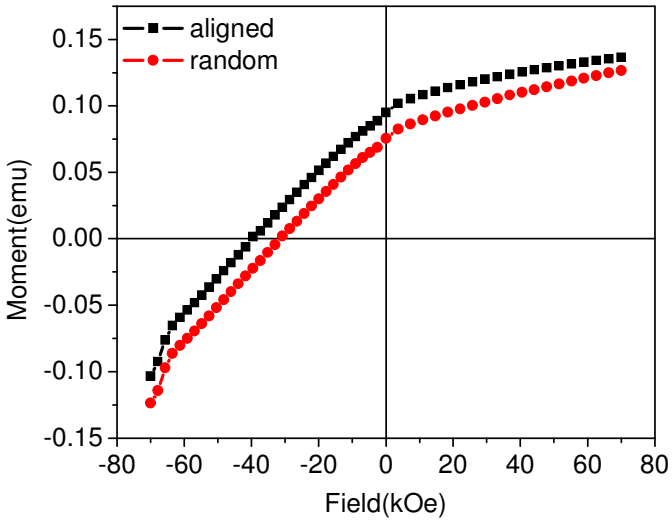

Figure 5.14 Demagnetization curves of the aligned and non-aligned fct particles. The curves were measured at 10 K from the aligned 8 nm particles and the randomly aligned particles in frozen alcohol. The particles were annealed at 700°C for 4 hours.

Another reason for the difficulty in aligning the nanoparticles is associated with an observation of the polycrystalline feature of the annealed fct particles. Figure 5.15 shows with a high-resolution TEM image an example of an annealed nanoparticle. In case of large size particles (15 nm), roughly 50% of the annealed particles are polycrystalline. For polycrystalline nanoparticles, the domain-grain relationship can be complicated and the magnetization reversal cannot be described in a simple model.

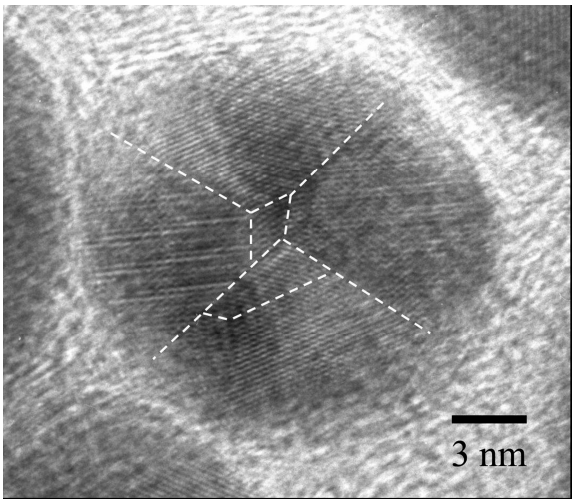

Figure 5.14 HRTEM image of an annealed fct FePt nanoparticle showing the polycrystalline morphology.

CHAPTER 6

FUTURE WORK - MICROREACTOR SYNTHESIS OF FePt NANOPARTICLES

6.1 Introduction

Recently, enormous efforts by many researchers to synthesis single or multi-element nanoparticles have resulted in continued advances in obtaining new nanoparticles with controllable properties (Chapter 2). However, properties of the nanoparticle materials rely principally on chemical synthesis parameters that control the important factors such as 1) Intra-particle homogeneity of composition, 2) Inter-particle composition distribution, 3) Particle size distribution, and 4) Particle shape distribution.

Each factor introduces variability to resulted products in such a magnitude that each batch of nanoparticles synthesized by chemical reduction requires extensive analytical characterization to ensure certain property uniformity. Unfortunately, the percent of batches of nanoparticles that possess the required properties remain low, reducing the efficiency of the chemical process needed for bulk magnet research due to low batch yields. Moreover, due to lower yields, potential exposure to toxic precursors, waste cost of disposal and usage of expensive precursors and solvents remains unnecessarily high that ultimately increases production cost of the nanoparticles. In response to these process issues, researchers are investigating the use of microreactors to synthesize nanoparticles such as CdSe, [108-111] and Au [112] among many others in an

effort to improve the nanoparticle quality in terms of composition and size control while simultaneously reducing the cost of production.

Convention chemical methods for producing nanoparticles usually involve gram level quantities of heated solvents along with milligram quantities of precursors and coordinating surfactants, which are injected at specified process points in a batch setup using glassware of several cubic centimeters in volume (see chapter 2 chemical methods). However, several factors that are difficult to control influence the particle quality such as the injection process, localized temperature and compositional variations, stirring rates and cooling rates [110]. In a continuous flow reactor, stead-state conditions can be established for reactant fluids with Reynolds numbers ($\mathrm{Re} = \frac{vl\rho}{\mu}$ where v = fluid velocity, l = diameter of capillary, ρ = density of fluid and μ = fluid viscosity) below 2000, which result in laminar flow regimes [113]. As the dimensions are reduced below 100 μm, mixing times become very small [114] resulting in reaction volumes that are more homogeneous with respect to temperature, concentration, and mass transport develop leading to potentially greater control of the nucleation and growth process involved in nanoparticle formation [112]. An example of a simple microreactor system is shown in figure 6.1.

Additional benefits of such system include the ability to study the effect of changes to the reaction parameters on the nanoparticles in a continuous manner. A more thorough systematic evaluation of the nucleation and growth process for each system of interest can result due to the sheer magnitude of data that can be collected continuously

coupled to the measured changes to the resulting particles. In effect, one continuous reaction run translates to numerous batch processes to gather the same information.

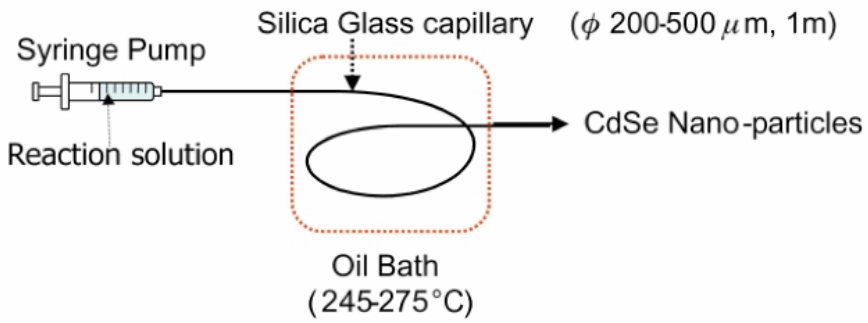

Figure 6.1 Microreactor design used for CdSe synthesis. [109]

Although the microreactor synthesis provides the potential for greatly enhanced control over particle composition and morphology, low production volumes and reactor fouling need addressing. Ideally, the issue of low volumes can be offset by the establishment of parallel reactors. For example, 70 microreactors using a flow rate of 0.25 mL/min can process 10 L reactor fluid in 10 hours [109]. Moreover, in parallel operation an inoperative microreactor can be readily replaced [115], preserving the required production volumes. Reactor fouling can occur if particles nucleate on the microchannel surface leading to particle growth, plugging and unstable microreactor conditions [111, 116]. A technique for minimizing fouling involves a two-phase system where gas bubbles are introduced into the microreactor fluid or reactant encapsulation in the carrier fluid [108]. It is clear that methods to reduce fouling would have to be evaluated based on the solvents, temperature requirements, precursor types and surfactants typical to the synthesis

methodology. Based on these considerations, we have started our work in designing and fabricating a new type of microreactors for nanoparticle synthesis.

6.2 Microreactor Design

A promising new approach to nanoparticle chemical synthesis with stable parameters in the chemical process is to use microfluidic reaction cells, as discussed above. In collaboration with the Center of Integrated Nanotechnology (CINT) at Sandia National Laboratory, we have designed a high performance micro-fluid reaction system and manufactured prototypes of the reactor (figure 6.2 and 6.3). The microreactor design in figure 6.2 provides eight injection points for introduction of the complexed metal ions used as precursors for forming the metallic nanoparticles into the reactor flow path. Heating elements are available to each injection point, which allows thermal control of the fluid as it enters the reactor flow path. In addition, precursor concentration could be specified at each injection point in the microreactor. Optimization of the configuration of the eight injection flow rates, precursor concentration and 13 heating elements would be required to obtain high quality nanoparticles and knowing which parameter to modify to change particle size, shape or composition would be challenging.

Leveraging and integration of the microfluidic reaction cell with high performance fluid control interface can provide additional opportunities for controlling the synthesis parameters. Next we will present our work in the reactor interface design and digital control of the synthesis systems based on our experience in chemical solution synthesis of FePt nanoparticles.

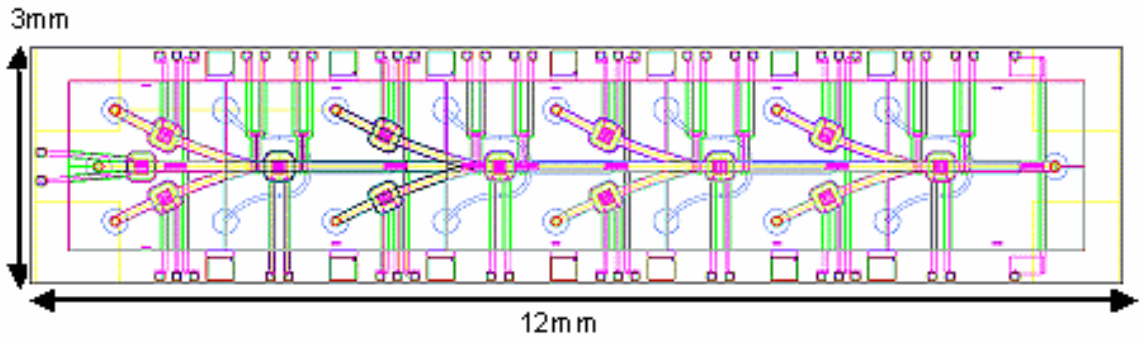

Figure 6.2 Schematic of microfluid reaction cell courtesy of CINT.

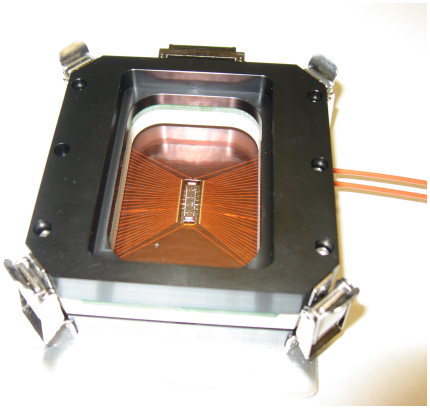

Figure 6.3 Photo of prototype microfluid reaction cell manufactured at CINT.

6.3 Reactor Interface

The system is based on commercially available high performance liquid chromatography (HPLC) units, which would connect to the microfluid reaction cell where normally a column would be placed. For example, Waters Corporation provides a system known as nanoACQUITY UPLC ™, which is designed for nano-scale seprations. Fortunately, the delicate systems control used is ideally suited to control the fluid conditions required for the microreactor. Precise flow rates can be varied from 200 nL/min to 100 µL/min and with these systems, back-pressure monitoring and pump

interlocks can prevent excessive hydrostatic pressure on the reactor which can result in fracture of the microreactor.

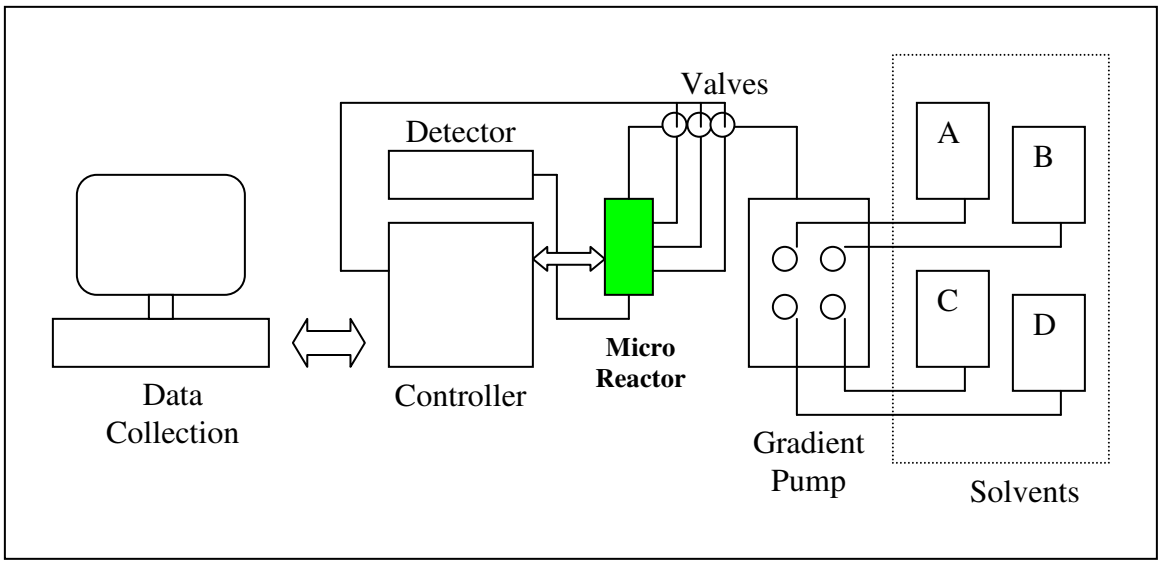

Figure 6.4 Schematic of microfluid reactor system for FePt synthesis.

Replacing the column with the microreactor can then open opportunities not available with conventional injection systems. For example, extensive cataloguing of surfactant precursor and solvent-blending effects which can induce geometric changes to the nanoparticles could be collected. If differing solvents are such as dioctyl ether or phenyl ether (reservoir A &B in figure 3), are slowly varied in composition using a gradient pump, precise determination of the structure blend correlation can allow the researcher to catalogue the blend ratios needed to product particles of particular geometry. In addition, particle size and surfactant concentration such as Oleic Acid and Oleyl Amine (reservoir C & D) can be studied and correlated in a similar manner

allowing a stable well characterized process to be determined for fine control over particle size and shape.

As opposed to small injection needles recommended for a microrector, combining the automated and continuous operation with the large volume reservoir of the nanoACQUITY UPLC™ will allow continuous high quality production of magnetic nanoparticles providing the needed mass of nanoparticles required for compaction experiments on soft/hard exchange coupled bulk magnets.

The nanoACQUITY UPLC™ system is also designed to interface with external equipment, which may simplify the controls needed to drive the heating elements within the microreactor although details will have to be determined from Waters Corporation. Several parameters would require defining in order to complete the system which include 1) interface controls and data acquisition for the microreactor heater, 2) controls for secondary flow path valves used to inject additional material for controlled particle growth characteristics, 3) interface to specialized microreactor detector used to analyze fluid and particle characteristics within the reactor, 4) determination of particle adhesion characteristics to similar surfaces and 5) defining of reactor preparation and post reaction cleaning procedures.

Tests can be performed on the prototype microreactor to assess the effectiveness of methods used to reduce particle adhesion. Initially, procedural development could occur in bench top scale equipment by testing different coatings on silicon surfaces in a typical reaction setup. After cleaning with a series of solvents, the substrate can be analyzed by SEM to gauge the effectiveness in preventing particle adhesion to the

substrate surface. After determination of the most effective method on the silicon surface, the method can be extended to the prototype system where microscopic observation on the micro channels can be performed (note that the reactor in figure 6.3 has a glass top allowing such observation).

Compositional and flow controls can be accomplished through the use of the gradient pump and solvent reservoirs. Additional control capabilities can be added through the installment of flow valves that can take advantage of the extra inline injection ports on the microreactor providing the capability to specify particle sizes or core shell structures by interface controls that allow injection points, flow and temperature profiles to be specified. If successfully integrated, the total system would provide an opportunity for forefront research in the field of microfluidic reactions and nanoparticle production.

6.4 Process Study on Particle Formation in Microreactors

In the chemical reduction process, a nucleation and growth process produces single or binary metallic particles or their respective oxides depending on the nature of the reductant, solvent, surfactant and process sequence. Preferential shape can be conferred to the particles through the selection of surfactants and the sequencing of the surfactant additions during processing [70]. In microreactors, the reactor temperatures and temperature ramp rates can be controlled to tune the average particle size of the nanoparticles [70]. For binary alloys, if nanoparticle composition homogeneity is desired, simultaneous nucleation of the two components would be required. However, in reality achieving uniform composition throughout the particles is difficult; therefore, reflux temperatures up to 300^{o}C become critical to distributing the atomic constituents in the

particles through diffusion [70]. For binary alloys with core-shell structure, the differing nucleation rates of the components will naturally provide this structure; however, reflux temperatures and times must be considered in order to minimize interdiffusion of the atoms.

As mentioned earlier, individual particle composition and distributions of compositions across a system of particles is difficult to control and is limited by the nucleation rate of each metallic precursor, which is defined by the following equations [11]:

$$J_N = A\exp\left(\frac{-\Delta G_N}{RT}\right) \tag{6.1}$$

$$\Delta G_N = \frac{16}{3}\pi\gamma_{SL}^3\left(\frac{\Omega}{RT\sigma}\right)^2 \tag{6.2}$$

Where ΔG_N is the free energy required for nucleation, γ_{SL} is the solid-liquid interfacial energy, Ω the molar volume, R is the gas constant and σ the saturation index. With temperature playing a critical role in nucleation rate, localized heating on each precursor injection point designed within the microreactor (Fig. 6.2) may allow tuning of nucleation rate of nanoparticles that will allow particles of homogeneous composition to form. Determination of specific injection temperatures would start by fixing the one precursor temperature then the secondary precursor. Moreover, with the initial particle size and composition defined by the first set of injection points, additional down stream injection of precursors could provide a controlled means for growing larger, homogeneous particles or core-shell structures. The capability to effectively grow the homogenous

particles to consistent size would depend on precise control of nucleating conditions, which is described from thermodynamics in the following equations [11]:

$$r_c = \frac{2\Omega\gamma_{SL}}{\Delta\mu} \tag{6.3}$$

$$\Delta\mu = RT\ln\frac{(A^aB^b)}{K_{sp}} \tag{6.4}$$

Where γ_{SL} is the solid-liquid interfacial energy, Ω the molar volume, R is the gas constant, σ the saturation index, K_{sp} the solubility constant and $\Delta\mu$ the change in chemical potential. Since inject point temperatures would be initially set to initiate nucleation of the precursors which would define the critical radius, the reaction flow temperatures can be altered to achieve the desired growth rate and final particle size. With the injection temperatures determined, the reactor flow path temperature would be stepped to assess the effect on the particle size. At this juncture, temperatures for the first injection port segment and reactor temperature is set relative to a constant flow rate and precursor concentration, which would be defined to ensure the proper atomic composition is achieved.

Surfactants can influence the particle size, which for bimetallic magnetic nanoparticles, an increase in surfactant concentration increases the particle size. This reported effect can be rationalized through inspection of equation (6.3) and (6.4). If the surfactant substantially complexes the formed atomic components, the solubility is increased, thereby reducing the saturation index which reduces the chemical potential. The inverse relationship between the critical radius and difference in chemical potential

points to an increased particle size with an increased surfactant concentration. Since the additional injection ports provide an easy method for extending the particle size, the surfactant injection point and combination of surfactants would be strictly used for geometric control of the particles.

Interaction of the surfactant on the step edges on growing facets influences the growth rate of the facet if a sufficient difference in energy exists for different crystal faces. Surfactants that show a preferential interaction with a facet will inhibit the growth of the facet, allowing the facets with minimal interaction to continue to grow. A mixture of surfactants are usually applied to the system of growing particles at different times to induce this growth effect [70] [16]. The microreactor can supply the surfactants at a various points along the reactor flow path. An interesting aspect to this reactor is the additional supply of precursors. Once operating parameters are defined to produce the initial particle, the proper amount and sequence of surfactant injection combined with additional precursors could be used in latter portions of the reactor flow path to develop specific geometery.

6.5 Evolutionary Computation in Chemical Synthesis of FePt Nanoparticles

Evolutionary computations (EC) have found utility in assisting researchers in global optimization of many systems such as electrical circuits [118-119], antenna geometry [120-124], polymer structures [125-135] and analytical applications [136-137] by structuring the computer program to mimic evolutionary pathways through biological information exchange, mutation and environmental selective pressures. The resulting program provides a directed search capability ideally suited for complex solution landscapes

where gradient search methods can become trapped or extensive CPU demands require parallel processing.

In this section, we will make an attempt to apply EC to chemical solution synthesis of FePt nanoparticles, with the goal of optimizing the synthesis parameters. This will be the first step to the digital controlled continuous production of high quality nanoparticles using microreactors.

Chemical solution methods used to form nanoparticles vary considerably in precursors, surfactants, solvents, process temperature and sequencing of events. [138-145] Can the parameters to be sufficiently determined so that particle size can be accurately controlled? Can it be refined to include particle shape, composition or particle distribution characteristics? EC has the capability for solving problems involving complex solution landscapes; furthermore, EC can avoid trapping of the optimizer within local minima or maxima leading to the desired global optimum or if preferred, a list of sub-optimal solutions along with the global solution for use in guiding experimental plans.

6.5.1 Chemical Process Modeling

In the chemical reduction process, a nucleation and growth process produces single or binary metallic particles or their respective oxides depending on the nature of the reductant. Preferential shape can be conferred to the particles through the selection of surfactants and the sequencing of the surfactant additions during processing. Reactor temperatures are controlled to tune the average particle size of the nanoparticles. For binary alloys, if nanoparticle composition homogeneity is desired, simultaneous

nucleation of the two components would be required. However, in reality achieving uniform composition throughout the particles is difficult; therefore, reflux temperatures up to 300^{o}C become critical to distributing the alloy components in the particles through diffusion.

For binary alloys with core shell structure, the differing nucleation rates of the components will naturally provide this structure; however, reflux temperatures and times must be considered in order to minimize inter diffusion of the atoms.

Experimentally, the following variables have shown a significant effect on the particle size during chemical reduction [140]:

$r \sim 1/T$; where T = temperature

$r \sim \gamma_c$; where γ_c = surfactant concentration

$r \sim Pc$; where Pc = precursor concentration

A process model based on a modified Gaussian distribution in which temperature is included can be constructed:

$$P(r,T) = \beta_0 + \beta_1 \exp(-\beta_2(r-r_{ave})^2/T) \quad (6.5)$$

The properties of this function graphically show the changes to the nuclei as a function of radius and temperature in figure 6.5.

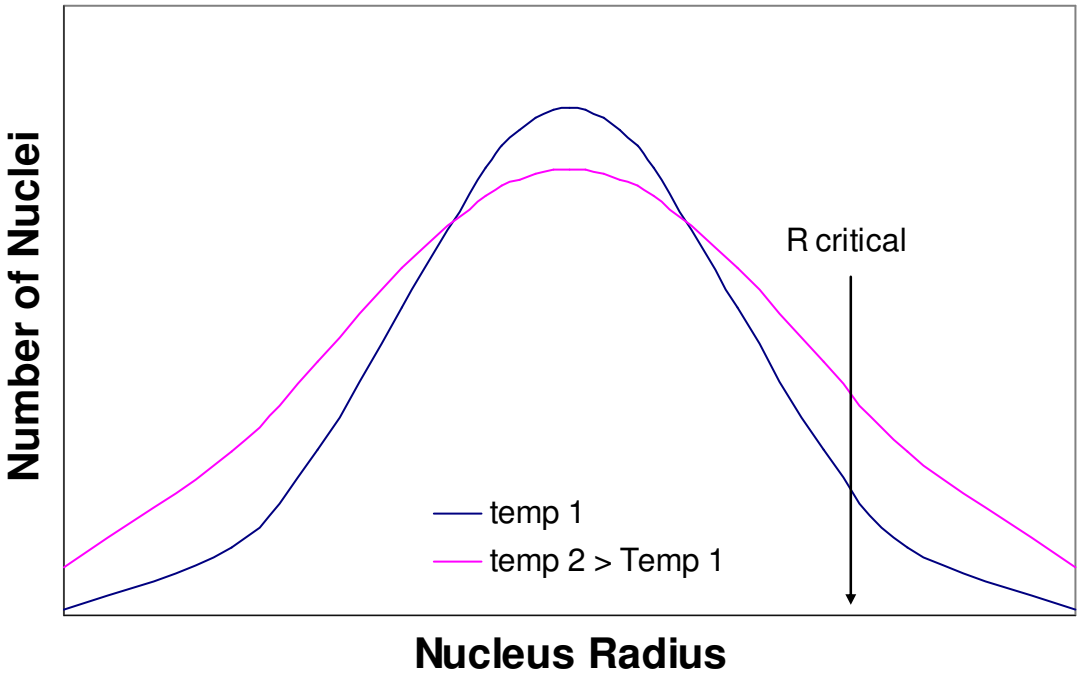

Figure 6.5 Graphic of the modified Gaussian function from temperature changes.

If the critical nuclei radius as determined from classical nucleation and growth theory (R critical = $2\gamma/\Delta\mu$) is represented as shown on the graph, the area under the graph would be proportional to the number of nuclei formed homogeneously. In addition to this expression, the effects of surfactants must be included. For the hot reduction methods, it has been observed that an increase in surfactants causes an increase in particle size. For this reason, the overall distribution is then modeled in the following manner:

$$P(r,T,\gamma) = \beta_0 + \beta_1 \exp(-\beta_2(r-r_{ave})^2/T\,\gamma) \qquad (6.6)$$

Where β_0, β_1, and β_2 are coefficients. The properties of the normalized distribution would be similar to figure 1 if surfactant is changed but temperature is held constant. Different

surfactants at the same concentration could yield a different distribution, which would affect the overall particle size.

The average particle size, would be proportional to the cube root of the amount of starting materials minus the amount of material bound in the average nucleus size as determined by the area under the distribution bounded by the critical radius for nucleation.

$$r_{est} = r_{crit} + r_{add} \tag{6.7}$$

$$r_{add} = (3M/4\pi\rho N)^{1/3} \quad N = \#\ \text{nuclei} \tag{6.8}$$

$$N = \Sigma\beta_0 + \beta_1 \exp(-\beta_2(r-r_{ave})^2/T\ \gamma)\Delta r \text{ (in the interval } i = r_{crit} \text{ to } r_{max}) \tag{6.9}$$

The determination of shape in this model is setup assuming each facet has an equal concentration of surfactant absorbed on the surface where:

$F_{111} + F_{110} + F_{100} = 1$ where F is the fraction of absorbed surfactant.

To account for the possibility that surfactant may not be absorbed equally, a weighting coefficient is introduced per facet:

$$\alpha_0 F_{111} + \alpha_1 F_{110} + \alpha_2 F_{100} / \Sigma\ \alpha_n = 1 \tag{6.10}$$

The α coefficient expresses the extent that the surfactant is unequally distributed on the available facets. A large α_0 relative to the others would indicate a lower energy facet relative to the others and a tendency for the other facets to grow faster than α_0. Finally, shape would have to be evaluated as a function of particle size in order to simultaneously determine size and shape control.

The objective function for the EA that estimates the weights on the chemical process model can be constructed by minimizing the square of the difference between the target property and the calculated values.

Min $\Delta r^2 = (r_{meas} - r_{est})^2$ using the coefficients β_0 ,β_1 ,β_2 in the solution landscape. In this manner, the parameter coefficients can be optimized via the EA by finding the coefficients that minimizes the differences among the training set data.

To gain insight into the chemical process, a model based on a modified Gaussian distribution of atomic clusters is proposed prior to nucleation as defined thermodynamically. An understanding of the process is possible through application of an evolutionary algorithm to determine the global and sub optimal solutions to the process parameters. This research will explore the development of an EA for optimizing the proposed process model parameters. The optimized process model will be validated experimentally through inverting the equation for the purpose of assessing its predictive capability. Modeling will be based on the use of the equations described in the chemical process modeling section:

$$\text{Min } \Delta r^2 = (r_{meas} - r_{est})^2$$

$$r_{est} = r_{crit} + r_{add}$$

$$r_{add} = (3M/4\pi\rho N)^{1/3}$$

$$\#\text{nuclei} = \Sigma\beta_0 + \beta_1 \exp(-\beta_2(r-r_{ave})^2/T\,\gamma)\Delta r \text{ (in the interval i = } r_{crit} \text{ to } r_{max})$$

6.5.2 EC training sets

Table 6.1 Temperature Variation Training Set

	Rxn 1	Rxn 2	Rxn 3	Rxn 4	Rxn 5
$Fe(acac)_3$	1.0 mole	1.0 mole	1.0 mole	1.0 mole	1.0 mole
$Pt(acac)_2$	1.0 mole	1.0 mole	1.0 mole	1.0 mole	1.0 mole
Pc	16.7 mg/mL	16.7 mg/mL	16.7 mg/mL	16.7 mg/mL	16.7 mg/mL
HDD	5.0 mole	5.0 mole	5.0 mole	5.0 mole	5.0 mole
Dioctyl Ether	30 mL	30 mL	30 mL	30 mL	30 mL
Oleic Acid	16.7 µL/mL	16.7 µL/mL	16.7 µL/mL	16.7 µL/mL	16.7 µL/mL
T_N	120°C	130°C	140°C	160°C	180°C

Table 6.2 Surfactant Variation Training Set

	Rxn 1	Rxn 2	Rxn 3	Rxn 4	Rxn 5
$Fe(acac)_3$	1.0 mole	1.0 mole	1.0 mole	1.0 mole	1.0 mole
$Pt(acac)_2$	1.0 mole	1.0 mole	1.0 mole	1.0 mole	1.0 mole
Pc	16.7 mg/mL	16.7 mg/mL	16.7 mg/mL	16.7 mg/mL	16.7 mg/mL
HDD	5.0 mole	5.0 mole	5.0 mole	5.0 mole	5.0 mole
Dioctyl Ether	30 mL	30 mL	30 mL	30 mL	30 mL
Oleic Acid	1.67 µL/mL	3.33 µL/mL	6.67 µL/mL	13.3 µL/mL	26.7 µL/mL
T_N	120°C	120°C	120°C	120°C	120°C

Table 6.3 Precursor Concentration Variation Training Set

	Rxn 1	Rxn 2	Rxn 3	Rxn 4	Rxn 5
$Fe(acac)_3$	1.0 mole	1.0 mole	1.0 mole	1.0 mole	1.0 mole
$Pt(acac)_2$	1.0 mole	1.0 mole	1.0 mole	1.0 mole	1.0 mole
Pc	1.67 mg/mL	3.33 mg/mL	6.67 mg/mL	13.3 mg/mL	26.7 mg/mL
HDD	5.0 mole	5.0 mole	5.0 mole	5.0 mole	5.0 mole
Dioctyl Ether	30 mL	30 mL	30 mL	30 mL	30 mL
Oleic Acid	16.7 µL/mL	16.7 µL/mL	16.7 µL/mL	16.7 µL/mL	16.7 µL/mL
T_N	120°C	120°C	120°C	120°C	120°C

6.5.3 Selection of EC System to Use for Optimization

For this study, a genetic algorithm (GA) will be used for the optimization of the reaction parameters. Real values will be used to comprise the genes in the solution space (population). The requirements are listed below:

- Parent selection: fitness proportional on the population.

  Example: rank equals 1 if $|r(\beta_0, \beta_1, \beta_2)-r_{target}|/r_{ave} \geq .5$

  0 if $|r(\beta_0, \beta_1, \beta_2)-r_{target}|/r_{ave} < .5$

- Crossover: 2 parent, 2 offspring – fixed point crossover

  Example: $Parent_1 = (\beta_{0,1}, \beta_{1,1}, \beta_{2,1})$, $Parent_2 = (\beta_{0,2}, \beta_{1,2}, \beta_{2,2})$

  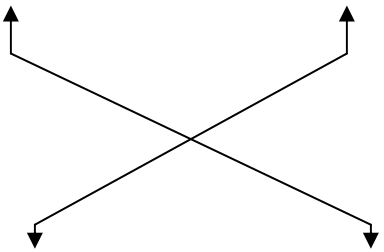

  $Offspring_1 = (\beta_{0,1}, \beta_{1,2}, \beta_{2,1})$, $Offspring_2 = (\beta_{0,2}, \beta_{1,1}, \beta_{2,2})$

- Mutation: randomly generated value from Gaussian distribution applied to 1% of population during each generation

  Example: $Offspring_1 = (\beta_{0,1}, \beta_{1,1}, \beta_{2,1})$,

  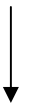

  Mutation on $\beta_{0,1}$

  $Offspring_1' = (\beta_{0,1} + N(0,\sigma), \beta_{1,1}, \beta_{2,1})$ where $N(0,\sigma)$ is a Gaussian distribution with average equal to zero and one sigma level.

- Objective function evaluation: minimization of the square of the difference in the target property (size) and the calculated property.

  Example: Min $\Delta r^2 = (r_{meas,1} - r_{est,1})^2 + (r_{meas,2} - r_{est,2})^2 + \ldots + (r_{meas,i} - r_{est,i})^2$

- New population: Population size is kept constant. After ranking according to the objective function, the lowest ranking elements in the dataset will be discarded.

  Example: for $Offspring_1 = (\beta_{0,1}, \beta_{1,1}, \beta_{2,1})$, => Δr^2 is low

  $Offspring_2 = (\beta_{0,2}, \beta_{1,2}, \beta_{2,2})$=> Δr^2 is greater than $Parent_1$

  $Offspring_1$ is considered more fit and will be placed in the population.

6.5.4 Develop Flow Chart

A proposed flow chart is listed in figure 6.6, which would be used to map the program flow and assist in programming of the optimization algorithm.

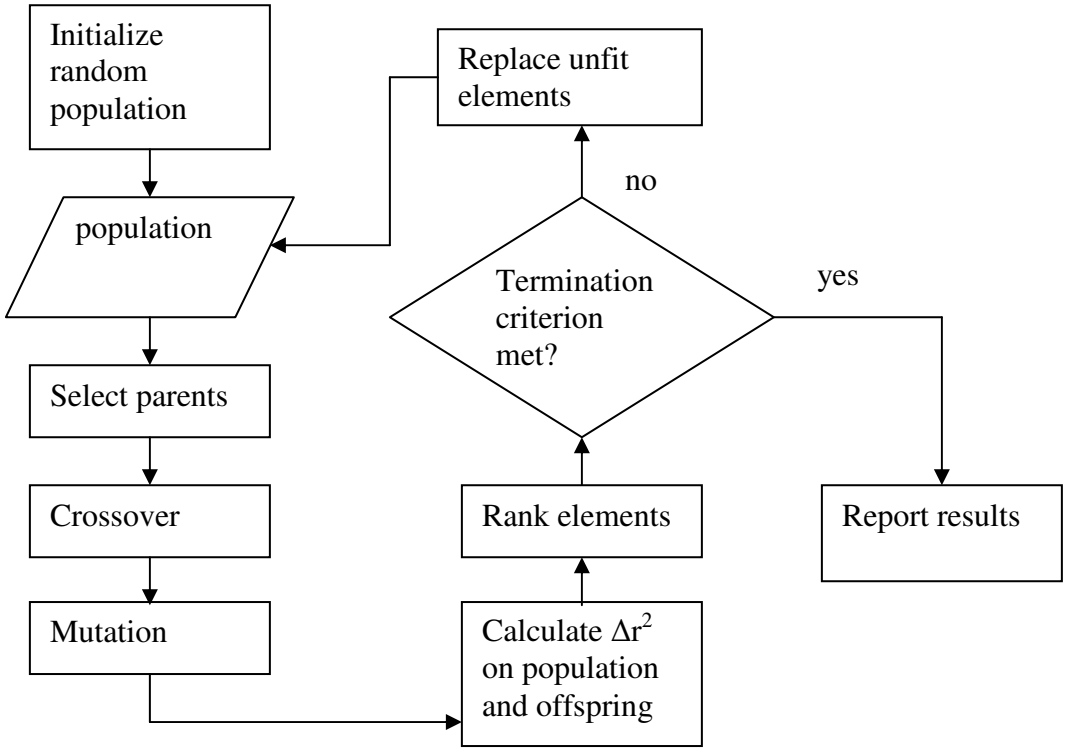

Figure 6.6 Flow chart of proposed algorithm for optimizing process variables.

6.5.5 Programming of Algorithm

Programming of the evolutionary algorithm will be accomplished using visual basic for applications (VBA) and Excel spreadsheet. The following pseudo code structure will be implemented within VBA.

Begin Program

g = 0 ;generation number

Initialize $Parent_i = (\beta_{0,i}, \beta_{1,i}, \beta_{2,i})$, ;random number assignment

While <not termination condition> do

Fitness evaluation ($Parent_i$)

Crossover (Parent$_i$)

Mutate (Offspring$_i$)

Object Function (Offspring$_i$)

If Offspring$_i$ best value = termination condition then

End while loop

Else

g = g + 1

end while

Display Offspring$_i$ best value

End program

6.5.6 Assessment of EC Convergence

The performance of the EA will be determined through the time or generations required to converge to an optimal point. Generally, the objective function value is plotted as a function of the generation number. For example, a plotting of Δr^2 verses generation number would result in the following graph:

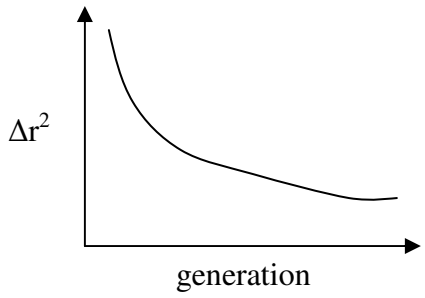

Figure 6.7 EC convergence.

Modification of the constraints on the coefficients, crossover points or mutation rate will alter the convergence rate and provide a way for assessing the EA performance as a function of generations.

6.5.7 Inclusion of Shape in EC

As mentioned in the chemical process model, the shape is valuated using the equation:

$$\alpha_0 F_{111} + \alpha_1 F_{110} + \alpha_2 F_{100} / \Sigma \alpha_n = 1$$

The α coefficient expresses the extent that the surfactant is unequally distributed on the available facets. A large α_0 relative to the others would indicate a lower energy facet relative to the others and a tendency for the other facets to grow faster than α_0. Experimentally, differentiation of shape develops as a function of size; therefore, α would have to be evaluated as a function of particle size in order to simultaneously determine size and shape control. It isn't known if the α would model as a linear or non-linear response, so multiple scenarios would have to be included.

Ultimately, a pareto front would be developed graphically to help assist in determining the best combination parameters to achieve a particular shape and size. For example, a minimum particle size is needed to produce preferential growth, which may require a particular set of conditions per α, particle size combination.

CHAPTER 7

SUMMARY

In conclusion, FePt nanoparticles with particle size of 2 - 9 nm with narrow size disribution have been successfully synthesized by a polyol reduction process. The size control was achieved by adjusting synthesis parameters such as the surfactant to Pt precursor ratio, precursor ligands and reactor heating rate. The as-synthesized FePt nanoparticles have chemically disordered fcc structure that can be transformed into chemically ordered fct structure through thermal annealing.

Moreover, a simplified and cost effective synthetic route has been found that provides a straightforward synthesis of FePt nanoparticles. 1,2-hexadecanediol alone can be used as reducing agent as well as an effective surfactant to protect the particle from agglomeration and oxidation. The as-synthesized particles have uniformity in size with particle diameters of approximately 2 nm. Structural and magnetic characterization show that FePt nanoparticles synthesized through this simplified method can provide the magnetically anisotropic $L1_0$ FePt phase with coercivity up to 2.3 Tesla in thin films after thermal treatment, representing an increase in H_c of nearly 30% over the traditional method using oleic acid and oleyl amine as the surfactants processed under the similar conditions.

Research on the salt-matrix annealing methodology reported here has marked the availability of building blocks of highly anisotropic fct FePt nanoparticles. Direct

application of fully converted fct FePt nanoparticles in magnetic recording media and biomedical experiments is now possible. Based on a simple and economic processing feasible for industrial scale-up production, this technique can be also applied to production of other isolated materials structures where heat treatments, but not sintering, are required. Unsintered fct FePt nanoparticles of 4, 6, 8 and 15 nm synthesized using the salt-matrix method showed a size dependence on the long-range order parameter calculated by XRD analysis with a maximum being reached at 8 nm. The coercivity of the particles as a function of diameter showed the same trend with a maximum coercivity being reached at 8 nm. Based on the XRD and SQUID data, phase transformation did not occur in the 2 nm particles, which matches with models that predict a size limitation for phase transformation from the fcc to fct structure with particle diameters ranging from 2 – 4 nm. Attempts to align 8 nm L1o FePt particles were not conclusive although further exploration on alignment techniques is warranted due to the enhanced magnetic properties of aligned assemblies.

Future work on enhanced synthetic control of nanoparticles through the use of reduced reaction volumes in a microreactors can potentially provide superior particle quality in terms of uniform composition within particles and throughout the particle assembly. Moreover, a continuous flow microreactor can enrich research opportunities by continued research on the mechanism on the nucleation and growth in bimetallic magnetic nanoparticles, solvent/ligand interactions and effects on particle morphology and the development of robust control algorithms for producing particles with well-defined characteristics for systems other than FePt.

APPENDIX A

INTRINSIC PROPERTIES OF SELECT MAGNETIC MATERIALS

Table A.1 Intrinsic Properties of Select Magnetic Materials [117].

Material	**$\mu_o M_s$ (T)**	**T_c (K)**	**K_1 (MJ/m^3)**	**Symmetry**
Fe_3O_4	0.60	858	-0.011	Cubic
$CoFe_2O_4$	0.50	793	0.270	Cubic
$NiFe_2O_4$	0.34	858	-0.0069	Cubic
□-Fe_2O_3	0.47	863	-0.0046	Cubic
CoPt	1.00	840	4.9	Tetragonal
FePt	1.43	750	6.6	Tetragonal
Sm_2Fe_{17}	1.17	389	-0.8	Rhombohedral
Sm_2Co_{17}	1.20	1190	3.3	Rhombohedral

APPENDIX B

CONVERSION FACTORS FOR COMMON MAGNETIC TERMS IN CGS AND SI UNITS

Table B.1 Conversion factors for common magnetic terms in CGS and SI units [9].

Magnetic Term	Symbol	CGS Unit	SI Unit	Conversion Factor
Applied Field	H	Oe	Am^{-1}	$10^3 / 4\pi$
Magnetization	M	cm^{-3}	Am^{-1}	10^3
Magnetic Induction	B	G	T	10^{-4}
Permeability	μ_o	Dimensionless	$H\ m^{-1}$	$4\pi \times 10^{-7}$
Relative Premeability	μ_r		Dimensionless	
Susceptibility	χ	$cm^{-3}\ Oe^{-1}$	Dimensionless	4π
Maximum Energy Product	$(BH)_{max}$	MGOe	$KJ\ m^{-3}$	$10^2/4\pi$

REFERENCES

1. Elkins, K. E.; Vedantam, T. S.; Liu, J. P.; Zeng, H.; Sun, S.; Ding, Y. and Wang, Z. L. *Nano Letters* **2003**, *3*, 1647-1649.

2. Solymar; L.; Walsh; D. *Electrical Properties of Materials*; Oxford University Press: 1998.

3. Mohn; P. *Magnetism in the Solid State*; Springer: 2003.

4. Spaldin; N. *Magnetic Materials*; Cambridge University Press: 2003.

5. Kneller, E. F. and Hawig, R. *IEEE Trans. Magn.* **1991**, *27*, 3588.

6. Coehoorn, R.; De Mooij, D. B. and De Waard, C. *J. Magn. Magn. Mater.* **1989**, *80*, 101.

7. Skomski, R and Coey, J. M. D. *Phys. Rev. B* **1993**, *48*, 15812.

8. Cullity; B. D. *Introduction to Magnetic Materials*; Addison-Wesley Publishing: 1972.

9. Skomski, R; Coey; J. M. D. *Permanent Magnetism*; Institute of Physics Publishing: 1999.

10. Winn, D. and Doherty, M. F. *AIChE J.* **1998**, *44*.

11. Dove, P.M., de Yoreo, J.J. and Weitner, S. *Biomineralization*; Mineralogical Society of America and Goechemical Society: 2003, *54*.

12. Shevchenko, Elena V; Talapin, D. V.; Schnablegger, H.; Kornowski, A.; Festin, O.; Svedlindh, P.; Haase, M. and Horst, W. *J. Am. Chem. Soc.* **2003**, *125*, 9090-9101.

13. LaMer, V. K. and Dinegar, R. H. *J. Am. Chem. Soc.* **1950**, *72*, 4847.

14. Watzky, M. A. and Finke, R. G. *J. Am. Chem. Soc.* **1997**, *119*, 10382.

15. Sugimoto, T. *Adv. Colloid Interface Sci.* **1987**, *28*, 65 - 108.

16. Puntes, V. F.; Krishnan, K. M. and Alivisatos, A. P. *Science* **2001**, *291*, 2115-2117.

17. Chen, S.; Wang, Z. L.; Ballato, J.; Foulger, S. H. and Carroll, D. L. *J. Am. Chem. Soc.*

18. Lian, S.; Wang, E.; Kang, Z.; Bai, Y.; Gao, L.; Jiang, M.; Hu, C. and Xu, L. *Solid State Commun.* **2004**, *129*, 485-490.

19. Yu, D. and Yam, V. W. *J. Am. Chem. Soc.* **2004**, *126*, 13200-13201.

20. Ghezelbash, A.; Sigman, B., Jr. and Korgel, B. A. *Nano Letters* **2004**, *4*, 537-542.

21. Sun, Y.; Mayers, B. and Xia, Y. *Nano Letters* **2003**, *3*, 675-679.

22. Tsai, K. and Dye, J. L. *J. Am. Chem. Soc.* **1991**, *113*, 1650-1652.

23. Leslie-Pelecky, D. L.; Zhang, X. Q.; Kim, S. H.; Bonder, M. and Rieke, R. D. *Chem. Mater.* **1998**, *10*, 164-171.

24. Leslie-Pelecky, D. L.; Bonder, M.; Martin, T.; Kirkpatrick, E. M.; Zhang, X. Q.; Kim, S. H. and Rieke, R. D. *IEEE Trans. Magn.* **1998**, *34*.

25. Nguyen , H. L. *Chem. Mater.* **2006**, *18*, 6414-6424.

26. Sun, S.; Murray, C. B.; Weller, D.; Folks, L. and Moser, A. *Science* **2000**, *287*, 1989-1992.

27. Sun, S.; Fullerton, E. E.; Weller, D. and Murray, C. B. *IEEE Trans. Magn.* **2001**, *37*, 1239-1243.

28. Y. Bao, Y.; Pakhomov, A. B. and Krishnana, K. M. *J. Appl. Phys.* **2005**, *97*, 10J317.

29. Hao Zeng, H.; Li, J.; Wang, Z. L.; Liu, J. P. and Sun, S. *IEEE Trans. Magn.* **2002**, *38*.

30. Sobal, N. S.; Ebels, U.; Mohwald, H. and Giersig, M. *J. Phys. Chem. B* **2003**, *107*, 7351-7354.

31. Momose, S.; Kodama, H.; Uzumaki, T. and Tanaka, A. *Appl. Phys. Lett.* **2004**, *85*, 1748-1750.

32. Chen, M. and Nikles, D. E. *Nano Letters* **2002**, *2*, 211-214.

33. Suslick, K. S.; Fang, M. and Hyeon, T. *J. Am. Chem. Soc.* **1996**, *118*, 11960-11961.

34. Zafiropoulou, I.; Devlin, E.; Boukos, N.; Niachos, D.; Petridis, D. and Tzitzios, V. *Chem. Mater.* **2007**.

35. Sui, Y. C.; Skomski, R.; Sorge, K. D. and Sellmeyer, D. J. *Appl. Phys. Lett.* **2004**, *84(9)*, 1525-1527.

36. Yang, J.; Deivaraj, T. C.; Too, D. and Lee, J. Y. *Journal of Physical Chemistry B* **2004**, *108*, 2181-2185.

37. Sun, X.; Jia, Z. Y.; Huang, Y. H.; Harrell, J. W.; Nikles, D. E.; Sun, K. and Wang, L. M. *J. Appl. Phys.* **2004**, *95(11)*, 6747.

38. Warne, B.; Kasyutich, O. I.; Mayes, E. L.; Wiggins, J. A. L. and Wong, K. K. W. *IEEE Trans. Magn.* **2000**, *36*, 3009-3011.

39. Yu, A. C. C.; Mizuno, M.; sasaki, Y. and Kondo, H. *Appl. Phys. Lett.* **2002**, *81 (20)*, 3768.

40. Fang, J.; Tung, L. D.; Stokes, K. L.; He, J.; Caruntu, D.; Zhou, W., L. and O'Conner, C. J. *J. Appl. Phys.* **2002**, *91 (10)*, 8616.

41. Sun, S.; Anders, S.; Thomson, T.; Baglin, J. E. E.; Toney, M. F.; Hamann, H. F.; Murray, C. B. and Terris, B. D. *J. Phys. Chem. B* **2003**, *107*, 5419–5425.

42. Ko, H. Y. Y. and Suzuki, T. *IEEE Trans. Magn.* **2007**, *43*.

43. Song, H. M.; Hong, J. H.; Lee, Y. B.; Kim, W. S.; Kim, Y.; Kim, S. J. and Hur, N. H. *Chem. Commun* **2006**, 1292-1294.

44. Fievet, F.; Lagier, J. P.; Blin, B.; Beaudon, B. and Figlarz, M. *Solid State Ionics* **1989**, *32/33*, 198.

45. Viau, G.; Fievet-Vincent, F. and Fievet, F. *Solid State Ionics* **1996**, *84*, 259.

46. Toneguzzo, P.; Viau, G.; Acher, O.; Guillet, F.; Bruneton, E.; Fievet-Vincent, F. and Fievet, F. *Journal of Materials Science* **2000**, *35*, 3767.

47. Chinnasamy, C. N.; Jeyadevan, B.; Shinoda, K. and Tohji, K. *J. Appl. Phys.* **2003**, *93(10)*, 7583.

48. Frommen, C.; Malik, S.; Wurfel, J. U.; Rosner, H. and Didschies, C. *Mater. Lett.* **2004**, *58*, 953-958.

49. Mizuno, M.; Sasaki, Y.; Inoue, M.; Chinnasamy, C. N.; Jeyadevan, B.; Hasegawa, D.; Ogawa, T.; Takahashi, M.; Tohji, K.; Sato, K. and Hisano, S. *J. Appl. Phys.* **2005**, *97*, 10J301.

50. Tzitzios, V.; Niarchos, D.; Margariti, G.; Fidler, J. and Petridis, D. *Nanotechnology* **2005**, *16*, 287-291.

51. Nakaya, M.; Kanehara, M. and Teranishi, T. *Langmuir* **2006**, *22*, 3485-3487.

52. Iwaki, T.; Kakihara, Y.; Toda, T.; Abdullah, M. and Okuyama, K. *J. Appl. Phys.* **2003**, *94(10)*, 6807-6811.

53. Liu, C.; Wu, X.; Klemmer, T.; Shukla, N.; Yang, X.; Weller, D.; Roy, A. G.; Tanase, M. and Laughlin, D. *Journal of Physical Chemistry B* **2004**, *108*, 6121-6123.

54. Takahashi, M.; Ogawa, T.; Hasegawa, D. and Jeyadevan, B. *J. Appl. Phys.* **2005**, *97*, 10J307.

55. Wang, S.; Kang, S. S.; Nikles, D. E.; Harrell, J. W. and Wu, X. W.

56. Ahrenstorf, K.; Albrecht, O.; Heller, H.; Kornowski, A.; Gorlitz, D. and Weller, H. *Small* **2007**, *3*, 271-274.

57. Park, J.-I. and Cheon, J. *J. Am. Chem. Soc.* **2005**, *123*, 5743-5746.

58. Baker, C.; Hasanain, S. K. and Shah, S. I. *J. Appl. Phys.* **2004**, *96*, 6657-6662.

59. Kuhn, L. T.; Bojesen, A.; Timmermann, L.; Fauth, K.; Goering, E.; Johnson, E.; Nielsen, M. M. and Morup, S. *J. Magn. Magn. Mater.* **2004**, *272-276*, 1485-1486.

60. Kang, S.; Miao, G.; Shi, S.; Jia, Z.; Nikles, D. E. and Harrell, J. W.

61. Aslam, M.; Fu, L.; Li, S. and Dravid, V. P. *J. Colloid Interface Sci.* **2005**, *290*, 444-449.

62. Zeng, H.; Li, J.; Liu, J. P.; Wang, Z. L. and Sun, S. *Nature* **2002**, *420*, 395-398.

63. Wang, Y. J.; Hussain, S. M. and Krestin, G. P. *Eur. Radiol.* **2001**, *11*, 2319-3139.

64. Frias, J. C.; Ma, J.; Williams, K. J.; Fayad, Z. A. and Fisher, E. A. *Nano Lett* **2006**,

65. Chung, S. H.; Hoffmann, A.; Bader, S. D.; Liu, C.; Kay, B.; Makowski, L. and Chen, L. *Appl. Phys. Lett.* **2004**, *85*, 2971-2973.

66. Haller, A.; Hartwig, S.; Matz, H.; Lange, J.; Rheinlander, T.; Kotitz, R.; Weitschies, Trahms, L. *Supercond. Sci. Technol.* **1999**, *12*, 956-958.

67. Berry1, C. C. and Curtis, A. S. G. *J. Phys. D: Appl. Phys.* **2003**, *36*, R198–R206.

68. Pankhurst, Q. A.; Connolly, J.; S K Jones, S. K. and Dobson, J. *J. Phys. D: Appl. Phys.* **2003**, *36*, R167–R181.

69. Nandwana, V.; K.E., E. and Liu, J. P. *Nanotechnology* **2005**, *16*, 2823.

70. Nandwana, V.; Elkins, K. E.; Poudyal, N.; Chaubey, G. S.; Yano, K. and Liu, J. P. *J. Phys. Chem. C* **2007**, *111*, 4185.

71. Weller, D. *IEEE Trans. Magn.* **2000**, *36*.

72. Dai, Z. R.; Wang, Z. L. and Sun, S. *Surf. Sci.* **2002**, *505*, 325–335.

73. Dai, Z. R.; Wang, Z. L. and Sun, S. *Nano Lett.* **2001**, *1*, 443–447.

74. Klemmer, T.; Hoydick, D.; Okamura, H.; Zhang, B. and Soffa, W. A. *Scripta Metalurgica et Materialia* **1995**, *33*, 1793.

75. Vedantam, T. S.; Liu, J. P.; Zeng, H. and Sun, S. *J. App. Phys.* **2003**, *93*, 7184–7186.

76. Lee, S.; Jun, Y.; Cho, S. and Cheon, J. *J. Am. Chem. Soc.* **2002**, *124*, 11244.

77. Chen, M.; Liu, J. P. and Sun, S. *J. Am. Chem. Soc.* **2004**, *126*, 8394-8395.

78. Chen, M.; Kim, J.; Liu, J. P.; Fan, H. and Sun, S. *J. Am. Chem. Soc.* **2006**, *28*, 7133.

79. Sra, A. K.; Ewers, T. D.; Xu, Q.; Zandbergen, H. and Schaak, R. E. *Chem. Commun.* **2006**, 750.

80. Sasaki, Y.; Mizuno, M.; Yu, A. C. C.; Miyauchi, T.; Hasegawa, D.; Takahashi, M.; Jeyadevan, B.; Tohji, K.; Sato, K. and Hisano, S. *IEEE Trans. Magn.* **2005**, *41*, 660.

81. Momose, S.; Kodama, H.; Uzumaki, T. and Tanaka, A. *Japanese Journal of Applied Physics* **2005**, *44*, 1147.

82. Yan, Q.; Purkayastha, A.; Kim, T.; Kroger, R.; Bose, A. and Ramanath, G. *Adv. Mater.* **2006**, *18*, 2569-2573.

83. Lyubina, J.; Gutfleisch, O.; Muller, K. H.; Schultz, L. and Dempsey, N. M. *J. Appl. Phys.* **2004**, *95 (11)*, 7474-7476.

84. Kitakami, O.; Shimada, Y.; Oikawa, K.; Daimon, H. and Fukamichi, K. *Appl. Phys. Lett.* **2001**, *78*, 1104-1106 .

85. Maeda, T.; Kai, T.; Kikitsu, A.; Nagase, T. and J., A. *Appl. Phys. Lett.* **2002**, *80*, 2147-2149 .

86. Kang, S.; Harrell, J. W. and Nikles, D. E. *Nano Lett* **2002**, *2*, 1033–1036.

87. Kang, S.; Nikles, D. E. and Harrell, J. W. *J. Appl. Phys.* **2003**, *93*, 7178-7180 .

88. Sun, X.; Kang, S.; Harrell, J. W.; Nikles, D. E.; Dai, Z. R. and Wang, Z. L. *J. Appl. Phys.* **2003**, *93*, 7337-7339 .

89. Platt, C. L.; Wiermann, K. W.; Svedberg, E. B.; van de Veerdonk, R.; Howard, J. K.; Roy, A. G. and Laughlin, D. E. *J. Appl. Phys.* **2002**, *92*, 6104-6109.

90. Jeyadevan, B.; Hobo, A.; Urakawa, K.; Chinnasamy, C. N.; Shinoda, K. and Tohji, K. *J. App. Phys* **2003**, *93*, 7574-7576 .

91. Jeyadevan, B.; Urakawa, K.; Hobo, A.; Chinnasamy, C. N.; Shinoda, K.; Tohji, K.; Djayaprawira, D. D. J.; Tsunoda, M. and Takahashi, M. *Jpn. J. Appl. Phys.* **2003**, *42*, L350-L352 .

92. Sato, K.; Jeyadevan, B. and Tojhi, K. *J. Magn. Magn. Mater.* **2003**, *266*, 227-230 .

93. Kang, S.; Jia, Z.; Shi, S.; Nikles, D. E. and Harrell, J. W. *Appl. Phys. Lett.* **2005**, *86*, 62503.

94. Ding, Y.; Majetich, S. A.; Kim, J.; Barmak, K.; Rollins, H. and Sides, P. *J. Magn. Magn. Mater.* **2004**, *284*, 336-341 .

95. Mizuno, M.; Sasaki, Y.; Yu, A. C. C. and Inoue, M. *Langmuir* **2004**, *20*, 11305-11307.

96. Zeng, H.; Sun, S.; Sandstrom, R. L. and Murray, C. B. *J. Magn. Magn. Mater.* **2003**, *266*, 227-232.

97. Saita, S. and Maenosono, S. *J. Phys.: Condens. Matter* **2004**, *16*, 6385-6394.

98. Sato, K.; Kajiwara, T.; Fujiyoshi, M.; Ishimaru, M.; Hirotsu, Y. and Shinohara, T. *J. Appl. Phys.* **2003**, *93*, 7414-7416 .

99. Takahashi, Y. K.; Koyama, T.; Ohnuma, M.; Ohkubo, T. and Hono, K. *J. Appl. Phys.* **2004**, *95*, 2690-2696 .

100. Miyazaki, T.; Kitakami, O.; Okamoto, S.; Shimada, Y.; Akase, Z.; Murakami, Y.; Shindo, D.; Takahashi, Y. K. and Hono, K. *Phy. Rev. B* **2005**, *72*, 144419.

101. Chepulskii, R. V. and Butler, W. H. *Phys. Rev. B.* **2005**, *72*, 134205.

102. Warren; B. E. *X-Ray Diffraction*; Dover: New York, 1990; pp 253.

103. Cebollada, A. a. *Phys. Rev. B.* **1994**, *50*, 3419.

104. Christodoulides, J. A., et al. *IEEE Tran. Mag.* **2001**, *37*, 1292.

105. Warren; B. E. *X-Ray Diffraction*; Dover: New York, 1990; pp 211.

106. Takahashi, Y. K.; Ohkubo, T.; Ohnuma, M. and Hono, K. *J. Appl. Phys.* **2003**, *93*, 7166 - 7168.

107. Gutfleisch, O. *Adv. Eng. Mater.* **2005**, *7*, 208.

108. Emory, M.; Chan, A.; Alivisatos, P. and Mathies, R. A. *J. Am. Chem. Soc.* **2005**, *127*, 13854-13861.

109. Nakamura, H.; Yamaguchi, Y.; Miyazaki, M.; Maeda, H.; Uehara, M. and Mulvaney, P. *Chem.Commun.* **2002**, 2844–2845.

110. Yen, B. K. H.; Stott, N. E.; Jensen, K. F. and Bawendi, M. G. *Adv. Mater.* **2003**, *15*, 1858 – 1862.

111. Krishnadasan, S.; Tovilla, J.; Vilar, R.; deMello, A. J. and deMello, J. C. *J. Mater. Chem.* **2004**, *14*, 2655–2660.

112. Wagner, J. and Kohler, J. M. *Nano Lett.* **2005**, *5*.

113. Kenis, P. J. A.; Ismagilov, R. F. and Whitesides, G. M. *Science* **1999**, *285*.

114. deMello, A. J. *Nature* **2006**, *442*.

115. Jensen, K. F. *Chem. Eng. Sc.* **2001**, *56*, 293-303.

116. Shestopalov, I.; Tice, J. D. and Ismagilov, R. F. *Lab Chip* **2004**, *4*, 316-321.

117. Sellmeyer; D. J.; Skomski, R. *Advanced Magnetic Materials*; Springer: 2006; pp 494.

118. F.Wang, Y.Li, L.Li, K.Li. Automated analog circuit design using two-layer genetic programming, Applied Mathematics and Computation, 2006.

119. J.F.M.Amaral, J.L.M.Amaral, C.C.Santini, M.A.C.Pacheco, R.Tanscheit, M.H.Szwarcman. Intrinsic Evolution of Analog Circuits on a Programmable Analog Multiplexer Array, ICCS, 2004, 1273-1280.

120. D.S.Weile, E.Michielssen. Genetic Algorithm Optimization Applied to Electromagnetics: A Review, IEEE Transactions on Antennas and Propagation, 1997, 45(3).

121. D.J.Caswell, G.B.Lamont. Wire-Antenna Geometry Design with Multiobjective Genetic Algorithms, IEEE, 2002.

122. S.Santarelli, T.L.Yu, D.E.Goldberg, E.Altshuler, T.O'Donnell, H.Southall, R.Mailloux. Military antenna design using simple and competent genetic algorithms, Mathematical and Computing Modelling, 2006, 43, 990-1022.

123. A.Hoorfar, Mutation-based Evolutionary Algorithms and their Applications to Optimization of Antennas in Layer Media, IEEE, 1999.

124. D.A.Van Veldhuizen, B.S.Sandlin, R.E.Marmelstein, G.B.Lamont, A.J.Terzuoli. Finding Improved Wire-Antenna Geometries with Genetic Algorithms, IEEE, 1998.

125. W.T. Brown, S. Martin, M.D. Rintoul, J.L. Faulon. Designing Novel Polymers with Targeted Properties Using the Signature Molecular Descriptor, J.Chem.Inf.Model. 2006, 46, 826-835.

126. R.Giro, M.Cyrillo, D.S.Galvao. Designing conducting polymers using genetic algorithms, Chemical Physical Letters, 2002, 366, 170-175.

127. M.J.Kharaajoo. Predictive Control of a Solution Copolymerization Reactor Using Locally Linear Identifier and Evolutionary Programming Optimizer, 2nd IEEE Intern. Conf. on Intelligent Systems, June 2004.

128. K.Mitra, S.Majumdar, S.Raha. Multiobjective dynamic optimization of a semi-batch epoxy polymerization process, Computers and Chemical Engineering, 2004, 28, 2583-2594.

129. S.S.S.Chakravarthy, D.N.Saraf, S.K.Gupta. Use of Genetic Algorithms in the Optimization of Free Radical Polymerizations Exhibiting the Trommsdorff Effect, J. Appl. Poly. Sci., 1997, 63, 529-548.

130. R.R.Gupta, S.K.Gupta. Multiobjective Optimization of an Industrial Nylon-6 Semibatch Reactor System Using Genetic Algorithm, J. Appl. Poly. Sci., 1999, 73, 729-739.

131. S.Massebeuf, C.Fonteix, S.Hoppe, F.Pla. Development of New Concepts for the Control of Polymerization Processes: Multiobjective Optimization and Decision Engineering. I. Application to Emulsion Homopolymerization of Styrene, J. Appl. Poly. Sci., 2003, 87, 2383-2396.

132. R.Vaidyanathan, M. El-Halwagi. Computer-Aided Synthesis of polymers and Blends with Target Properties, Ind. Eng. Chem. Res., 1996, 53, 527-634.

133. C.D.Maranas. Optimal Computer-Aided Molecular Design: A Polymer Design Case Study, Ind. Eng. Chem. Res., 1996, 35, 3403-3414.

134. K.V.Camarda, C.D.Maranas. Optimization in Polymer Design Using Connectivity Indices, Ind. Eng. Chem. Res., 1999, 38, 1884-1892.

135. N.K. Roy, W.D.Potter, D.P.Landau. Designing Polymer Blends Using Neural Networks, genetic Algorithms, and Markov Chains, Applied Intelligence, 2004, 20, 215-229.

136. H.C.Goicoechea, A.C.Olivieri. A new family of genetic algorithms for wavelength interval selection in multivariate analytical spectroscopy, J. Chemometrics, 2003, 17, 338-345.

137. A.Kakay, M.W.Gutowski, L.Takacs, V.Franco, L.K.Varga. Langevin granulometry of the particle size distribution, J. Phys. A: Math. Gen., 2004, 37, 6027-6041.

138. E.V.Shevchenko, D.V.Talapin, H.Schnableggar, A.Kornowski, O.Festin, P.Svedlindh, M.Haase, H.Weller. Study of Nucleation and Growth in the Organometallic Synthesis of Magnetic Alloy Nanocrystals: The Role of Nucleation Rate in Size Control of CoPt Nanocrystals, J. Am. Chem. Soc., 2003, 125, 9090-9101.

139. M.Chen, D.E.Nickles. Synthesis, Self-Assembly, and Magnetic Properties of FexCoyPt100-x-y Nanoparticles, Nano Letters, 2002, 2, 211-214.

140. S.Chen, Z.L.Wang, J.Ballato, S.H.Foulger, D.L.Carroll, Monopod, Bipod, Tripod, and Tetrapod Gold Nanocrystals, J. Am. Chem. Soc., 2003.

141. C.N.Chinnasamy, B., Jeyadevan, K.Shinoda, K.Tohji. Polyol-process-derived CoPt nanoparticles: Structural and magnetic properties, Journal of Applied Physics, 2003, 93.

142. B.L.Cushing, V.L.Kolesnichenko, C.J.O'Conner, Recent Advances in the Liquid-Phase Syntheses of Inorganic Nanoparticles, Chem.Rev., 2004, 104, 3893-3946.

143. F.Dumestre, B.Chaudret, C.Amiens, P.Renaud. Superlattices of Iron Nanocubes Synthesized from $Fe[N(SiMe_3)_2]$, Science, 2004, 303, 821-823.

144. J.Fang, L.D.Tung, K.L.Stokes, J.He, D.Caruntu, W.L.Zhou, C.J.O'Conner. Synthesis and magnetic properties of CoPt–poly,,methylmethacrylate nanostructured composite material, Journal of Applied Physics, 2002, 91.

145. D.Farrell, S.A.Majetich, J.P.Wilcoxon. Preparation and Characterization of Monodisperse Fe Nanoparticles, Journal of Physical Chemistry B, 2003, 107, 11022-11030.

BIOGRAPHICAL INFORMATION

Kevin Elkins was bonrn in Lufkin, TX. After graduating high school, he attended Texas A&M University receiving his Bachelor of Science Degree in Chemistry in 1992. Afterwards, the author worked in the oilfield industry where he gained experience in corrsion inhibitor synthesis, analysis and chemical characterization. Additional opportunities within the oilfield industry allowed the author to work in research and development in concrete polymer additives used to prevent concrete fluid loss and premature setting. During this time, the author developed a desire to pursue a deeper fundamental understanding of material properties needed to engage in research and development in a leading role. In 1998, the author was admitted as a graduate student into the Materials Science and Engineering Department at the University of Texas at Arlington. Under the supervision of Dr. J. Ping Liu, he researched and developed several chemical reduction methods used to produce FePt nanoparticles of various sizes and lead the development of a process used to convert the fcc FePt nanoparticles into the magnetically hard fct phase without significant sintering. Throughout this research, the author has enriched his knowledge and experience in magnetic phenomena, magnetic characterization and chemical production of magnetic nanoparticles. The author plans to reside in the DFW metroplex where he will pursue research and development in polymer systems with his current employer.